A Study of Electronic Nematicity in Cuprate Superconductors using Resonant Soft X-Ray Scattering

by

Naman Kumar Gupta

A thesis
presented to the University of Waterloo
in fulfillment of the
thesis requirement for the degree of
Master of Science
in
Physics

Waterloo, Ontario, Canada, 2020

Author's Declaration

This thesis consists of material all of which I authored or co-authored: see Statement of Contributions included in the thesis. This is a true copy of the thesis, including any required final revisions, as accepted by my examiners.

I understand that my thesis may be made electronically available to the public.

Statement of Contributions

The main results of this thesis are based on a manuscript ready to be submitted. I wrote a significant part of the manuscript, working closely and incorporating feedback from my supervisor. The results in the manuscript — included in Chapter 5 — are from measurements performed by previous and current members of the group*, including myself. Chapter 5, which is mostly left in the to-be-submitted form, has some additional data from our recent and previous measurements to provide a full picture and coherent structure. Chapter 6 is a work-in-progress, it contains preliminary results from uniaxial stress device measurement performed by me earlier this year. Chapter 2, 3, and 4 are background texts to give some context to the general reader.

*David Hawthorn, Andrew Achkar, Christopher McMahon, Tianyu Shi, Haofei Wei, and Rantong Gong participated to the beamtimes.

Abstract

The cuprate high-temperature superconductors involve a complex interplay between different structural and electronic symmetry-breaking phases. In the last decade, rotational and translational symmetry-breaking phases — electronic nematicity and density wave order — have been established as generic and distinct features in the cuprate phase diagram using different probes. To understand this connection between these symmetry breaking phases, we use resonant soft x-ray scattering (RSXS) — a technique that combines x-ray diffraction and x-ray absorption spectroscopy — at different photon energies allowing us to differentiate between ionic displacement and orbital asymmetry. The results presented in this thesis are based on the measurements performed at the REIXS beamline at the Canadian Light Source (CLS).

In this thesis, we employ RSXS to explore the low-energy physics of different symmetry breaking phases in the cuprate high temperature superconductor $La_{1.6-x}Nd_{0.4}Sr_xCuO_4$ or Nd-LSCO, as a function of carrier density (hole doping) by varying Sr content. The scattering cross section on resonance develops sensitivity to the orbital symmetry which at different photon energies can be used to probe the relationship between electronic nematicity of the CuO_2 planes, structural distortions, and charge density wave (CDW) order.

We measure the temperature dependency of the orbital asymmetry to probe the relationship between electronic nematicity of the Cu $3d$ orbitals and hole doping in Nd-LSCO. We achieve this by recording the low temperature (001) Bragg peak — which provides sensitivity to electronic nematicity — at different atomic edges in single crystals of Nd-LSCO at hole dopings of x = 0.125, 0.17, 0.18, 0.19, and 0.24. In the vicinity of the putative pseudogap quantum critical point – at x = 0.23 in Nd-LSCO – we find evidence for a considerable decrease in the measure of electronic nematicity as the degree of orbital asymmetry is reduced. These results identify electronic nematicity as a possibility for the ordered phase responsible for the quantum critical point in overdoped cuprates. Alongside electronic nematicity, we also measure the evolution of charge ordering or CDW order in these samples at the above-mentioned hole dopings. We report the absence of CDW order beyond the hole doping of x = 0.18, which is in agreement with results from other techniques.

Possible approaches to disentangle the role of nematicity, CDW order and superconductivity in the cuprates require a means to vary one (nematicity or CDW order) while minimizing changes to other. A powerful way to achieve this goal is to apply uniaxial strain in order to tunably change the degree of orthorhombicity, and measure the impact of the resulting changes of the crystal structure on electronic nematic order, unidirectional

CDW order and superconductivity. The second part of the thesis is a work in progress, discussing the design and working of a recently in-house fabricated uniaxial stress device with the potential to do so. We provide preliminary results as a proof of principle for the uniaxial stress device which can tunably apply uniaxial strain, allowing us to perform in-situ RSXS experiments at CLS's line-of-sight Bragg geometry — recording the response of electronic nematicty and CDW order — with applied strain along a desired reciprocal space direction. We demonstrate the shifting of structural Bragg peaks confirming the application of in-plane uniaxial strain along [100] direction on a single crystal of x = 0.125 Nd-LSCO. We also note a slight broadening of the CDW peaks along the h-direction on applying compressive strain in the same material along the [100] direction.

Acknowledgements

First and foremost, I thank my supervisor David Hawthorn for introducing and giving me this wonderful opportunity to work in the field of high temperature superconductivity. I greatly appreciate your feedback and careful consideration to all of our discussions — from about a random arxiv pre-print to a potential experimental proposal — we have had in the last two years. Thanks Dave for the constant supply of ideas, encouragement, and freedom on various projects. I look forward to our discussions and partnership in the upcoming few years.

I would like to thank all the people who have participated and helped in making this thesis possible: Ronny Sutarto, Feizhou He, and Teak Boyko for being there helping out and keeping the life-force running in that UHV chamber, even outside of work hours. I would also like to thank my lab members, Rantong Gong and Christopher McMahon, who have always been extremely generous and a friendly presence — from helping with aligning samples in Saskatoon to fixing up the finicky wire-saw in Waterloo.

Next, I would like to thank my pseudo-group members: Kai Chung for the long walks and being there for the late-night breakdowns, Darren Pereira for being almost a brotherly presence, Daniel Lozano-Gómez for teaching how to cook, Daniel Wong for being a patient and encouraging presence, Alex Hickey, Addison Richards, Wen Jin, thanks you guys! I am lucky to share an office with you guys. Other people who made it a happy exercise to roam across corridors would include Steven Esau, Taylor Fraser, Julia Zangoulou to name a few. I would also like to mention Jennifer Reid and Archana Tiwari (and Kai Chung) for helping start the QM GradTalks, I think they are going better than we expected.

I would also like to thank my advisory committee members, Prof. Michel Gingras and Prof. Rob Hill for the interesting remarks, questions and valuable feedback in the committee meetings, they have greatly influenced my way of thinking as a young researcher. Also, thanks to Prof. Anton Burkov for I have genuinely enjoyed both the courses I took with you.

I would also take this opportunity to thank scientists and researchers from Waterloo who have been an essential part of my last two years: Hiruy Hale for helping in making the design/dream of unixial stress device come true, Stefan Idziak for being so generous and helpful in letting me run your hard x-ray machine alone and for the fun conversations too. Friends from the chemistry department for whom Bromine-etching is not at all a big deal (for me it is!). I would also like to thank Anja Drygala for handling with months old travel receipts, Ena Devedzija and Diana Goncalves for helping with paperwork, printing posters and sending out emails to physgrad mailing lists.

Thanks to all the friends in Waterloo who have helped me strike a ‘work-life’ balance in one way or another, included but not limited to Aritro, Gyan, Paul, Abhinav, Sunidhi, Pranav, and more.

Last and most importantly, I would like to thank my family for always being supportive and caring! Maa, Papa, Nipun, none of this would be possible without you!

Dedication

To my Nana and Nani, the former instilled an appeal of scientific method and the latter spoiled me with all things sweet

Table of Contents

List of Figures

La lutte elle-même vers les sommets suffit à remplir un cœur d'homme; il faut imaginer Sisyphe heureux.

- Albert Camus, Le Mythe de Sisyphe (1942)

Chapter 1

Introduction

In 1986, J. Georg Bednorz and K. Alex Müller working at the IBM Research Laboratory in Zurich discovered a Ba-La-Cu-O system [1] which had a superconducting transition temperature of 35 K, which was not only greater than the any superconducting system known at that time but also more than the proposed theoretical limit described by the theory provided by Bardeen, Cooper, and Schrieffer (BCS) which describes conventional superconductivity [2, 3]. It soon became cleared that BCS theory does not describe the superconductivity in $La_{2-x}Ba_xCuO_4$ when the very next year, in 1987, Chu and colleagues [4] discovered a Y-Ba-Cu-O system which exhibited a superconducting transition temperature of 93 K. The reason to what causes these transition metal oxides to show superconductivity at such high temperatures still remains an open problem in condensed matter physics.

Cuprate (or copper-oxide) high temperature superconductors started a revolution in condensed matter physics, one that holds the key to the next generation of technological advances built on artificially synthesized quantum materials. Inspired by the desire of achieving superconductivity at higher temperatures — still ongoing — the attempts bore fruit in terms of realizing theoretical breakthroughs of the last century, involving quantum mechanics, topology, theory of phase transitions into tangible materials. Since their discovery, cuprate superconductors have led to exciting physics almost every decade, from the first evidence of a stripe phase [5] to the rich physics of the pseudogap phase [6], from the still unknown machinery of intertwined symmetry breaking phases [7, 8] to strange metal phases, some of these co-existing and some even competing with the superconducting state [9]. Not only did we learn the exotic phase diagram of these materials but also they have led to tremendous advancements in the nature and sophistication of experimental techniques up to atomic scales, with which we can now probe cuprates and other strongly correlated electronic systems. An example of this is the discovery of unconventional superconductiv-

ity in more than seven classes of materials [10] — in the last 34 years — and the list is still increasing. Recent mentions include iron-based superconductors which share a lot of common features with cuprates. The highest recorded superconducting transition temperature[1] of around 135 K [11] — almost half as high as the room-temperature — comes from a Hg based cuprate.

In this thesis, we use resonant x-ray scattering to explore the low-energy physics of the different symmetry breaking phases in the cuprate high temperature superconductor $La_{1.6-x}Nd_{0.4}Sr_xCuO_4$ or Nd-LSCO. The main focus of this thesis involves investigating the occurrence of the electronic nematic phase, that is, when the electronic structure breaks the rotational (point group) symmetry but leaves the translational (lattice group) symmetry intact. Experimental evidences include reports of electronic nematicity from bulk transport [12, 13, 14], scanning tunneling microscopy (STM) measurements [15, 16], and inelastic neutron experiments [17]. Recently our group identified electronic nematicity in cuprate superconductors [18] and its relationship to the crystal structure as well as the CDW order using resonant x-ray scattering. Resonant soft x-ray scattering (RSXS) is a technique that combines x-ray diffraction and x-ray absorption spectroscopy at different photon energies allowing us to differentiate between ionic displacement and orbital asymmetry. The scattering cross section on resonance develops sensitivity to the orbital symmetry which at different photon energies can be used to probe the orbital anisotropy of the Cu $3d$ and O $2p$ states as we increase the concentration of holes, or apply structural deformations along a particular direction in the CuO_2 planes.

A brief review of different electronic and structural symmetry breaking phases in cuprates and the low-energy physics involved is presented in Chapter 2, it might help the reader place the significance of the results — provided in the later chapters — in a broader context. Chapter 3 provides background for the experimental technique of resonant soft x-ray scattering, setting up the theoretical framework followed by Chapter 4 which deals with the details of the experimental setup.

In Chapter 5, we provide results for the temperature dependency of the orbital asymmetry to probe the relationship between electronic nematicity of the Cu $3d$ orbitals and hole doping in Nd-LSCO. We achieve this by recording the low temperature (001) Bragg peak — which provides sensitivity to electronic nematicity [18] — at different atomic edges in single crystals of Nd-LSCO at hole dopings of x = 0.125, 0.17, 0.18, 0.19, and 0.24. In the vicinity of the putative pseudogap quantum critical point – at x = 0.23 in Nd-LSCO – we find evidence for a considerable decrease in the measure of electronic nematicity as the degree of orbital asymmetry is reduced. These results identify electronic nematicity

[1] At ambient pressure conditions.

as a possibility for the ordered phase responsible for the quantum critical point (QCP) in overdoped cuprates. Alongside electronic nematicity, we also measure the evolution of charge ordering or charge density wave (CDW) order — a spatial modulation of the charge that has been identified as a generic phase in cuprates that co-exists and competes with superconductivity [19] — in these samples at the above-mentioned hole dopings. We report the absence of CDW order beyond the hole doping of x = 0.18, which is in agreement with results from other techniques.

Amongst others, possible approaches to disentangle the role of nematicity, CDW order and superconductivity in the cuprates require a means to vary one (nematicity or CDW order) while minimizing changes to other. A powerful way to achieve this includes application of uniaxial strain in order to tunably change the degree of orthorhombicity, and measure the impact of the resulting changes of the crystal structure on electronic nematic order, unidirectional CDW order and superconductivity. Chapter 6 is a work in progress, discussing the design and working of a recently in-house fabricated uniaxial stress device with the potential to do so. It provides preliminary results as a proof of principle for the uniaxial stress device which can tunably apply uniaxial strain, allowing us to perform in-situ RSXS experiments at CLS's line-of-sight Bragg geometry — recording the response of electronic nematicty and CDW order — with applied strain along a desired reciprocal space direction. We demonstrate the shifting of structural Bragg peaks confirming the application of in-plane uniaxial strain along [100] direction on a single crystal of x = 0.125 Nd-LSCO. We also note a slight broadening of the CDW peaks on applying compressive strain of up to 0.3% in the same material along the [100] direction. Future directions include validation of the reported results and investigation of the electronic response along directions perpendicular to the applied strain.

Chapter 2

The physics of cuprate superconductors

2.1 Historical development

2.1.1 Conventional superconductivity

The first observation of a superconducting phase of matter dates back to 1911, when Heike Kamerlingh Onnes cooled Mercury at cryogenic temperatures to find the resistance abruptly disappear at a temperature of 4.2 K [20]. Soon other elemental superconductors were discovered — with transition temperatures as high as ∼10 K in Niobium — and which are now referred to as conventional superconductors. It took about 50 years after Onnes' discovery to develop a satisfactory microscopic theory for conventional superconductivity by Bardeen, Cooper, and Schriffer (BCS) who explained the possible mechanism through which electrons can create pairs — called Cooper pairs — that originate from a small attractive electron-electron interaction mediated by phonons [2, 3].

2.1.2 Unconventional superconductivity

In 1986, however, J. Georg Bednorz and K. Alex Müller working at the IBM Research Laboratory in Zurich discovered a Ba-La-Cu-O system [1] which had a superconducting transition temperature of 35 K, which was not only greater than the any superconducting system known at that time but also more than the proposed BCS limit. It soon became

clear that BCS theory does not describe the superconductivity in $La_{2-x}Ba_xCuO_4$ when the very next year, in 1987, Chu and colleagues [4] discovered a Y-Ba-Cu-O system which exhibited a superconducting transition temperature of 93 K. The reason to what causes cuprates and other similar transition metal oxides to show superconductivity at such high temperatures still remains an open problem in condensed matter physics.

2.2 Cuprate superconductors

The structure of the cuprates attributes greatly to the novel physics that emerge, see Fig. 2.1, the undoped parent compound has copper-oxide (CuO_2) layers separated by insulating spacer layers. The CuO_2 planes are doped by modifying the chemical makeup of spacer, or charge reservoir layers such that either the electrons are removed (hole doped) or introduced (electron doped) to the (quasi) two-dimensional CuO_2. For instance, the family of Lanthanum-based cuprate superconductors are hole doped children of the Mott-insulating parent compound La_2CuO_4. The undoped compound is a Mott insulator, that is electrons are localized at their lattice sites due to the strong Coulomb repulsion. As one varies the carrier concentration in the CuO_2 planes, it partially alleviates the strong Coulombic repulsions allowing electrons to delocalize (or hop) across the underlying quasi-2D lattice structure.

Based on different hole doping levels, one can move from an antiferromagnetic state at underdoped region to optimal doping where superconductivity forms, on further increasing the concentration of holes we get a fairly conventional metallic state that can be described by a Fermi liquid theory. For the last 34 years, cuprates have been a subject of intense investigation both theoretically and experimentally. We present a very brief and, naturally, incomplete introduction to the relevant phases for the scope of this thesis. For a more complete treatment of the development and current state of the field, the reader might find Ref. [9, 21, 8, 6] to be helpful.

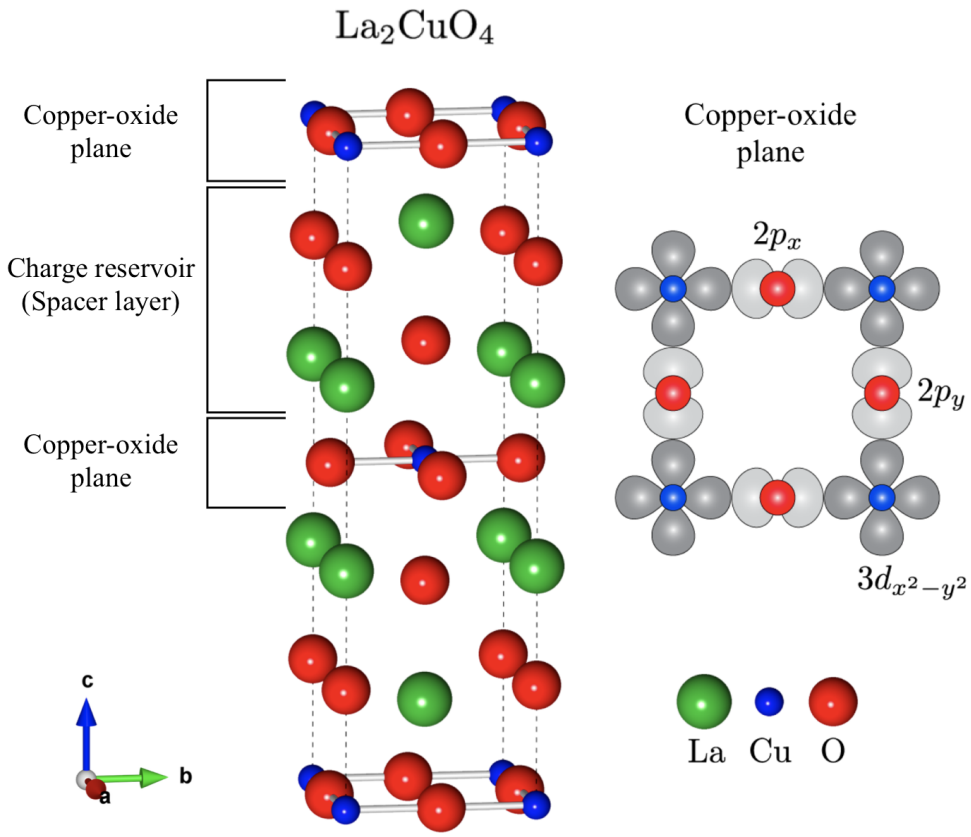

Figure 2.1: Crystal and electronic structure of cuprate superconductors. As we traverse the phase diagram, the undoped parent compound La_2CuO_4 show superconductivity and other electronic phases by hole doping the copper-oxide or CuO_2 planes. In La_2CuO_4, La is substituted with Sr or Ba and optionally co-doped with Nd or Eu like in Nd-LSCO. In cuprates, the generic structural unit is the (quasi) two-dimensional CuO_2 plane whose electronic structure, close to the Fermi level, involves hybridization of a $3d_{x^2-y^2}$ hole on the copper sites with an in-plane $2p_x$ and $2p_y$ oxygen orbitals. Arrow labeled a, b, c are crystallographic axes.

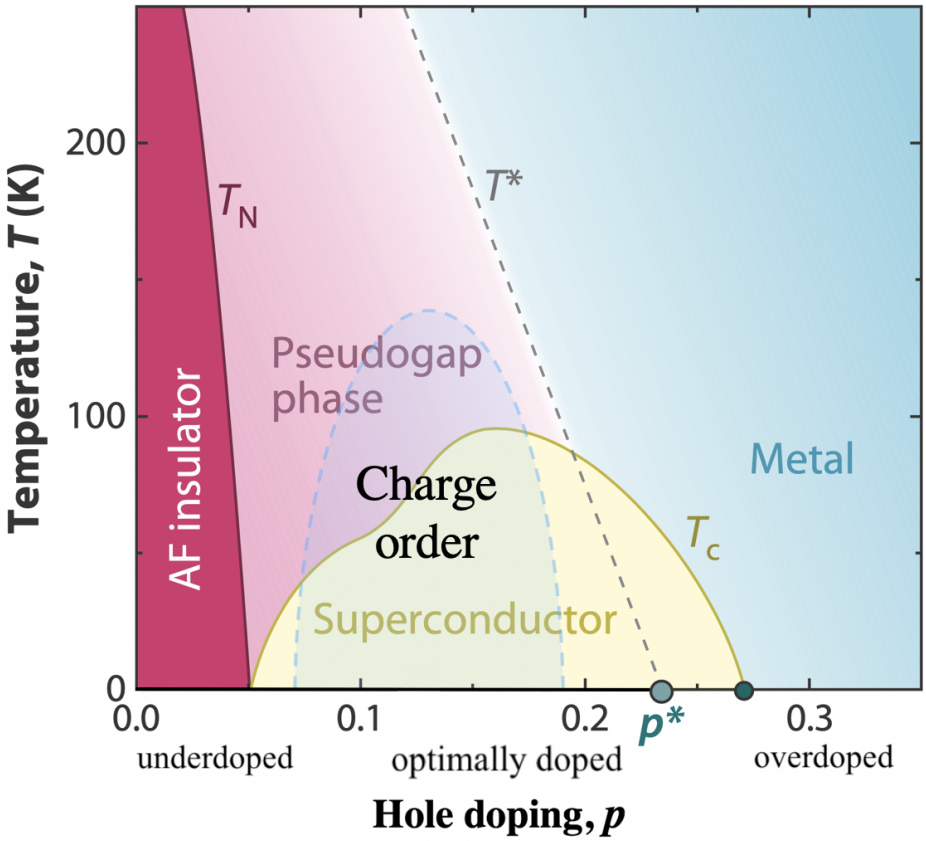

Figure 2.2: Phase Diagram: Temperature versus hole doping levels for the copper oxides. When the parent Mott insulator is doped by substituting an electropositive atom in the spacer layer, it exhibits various electronic symmetry-breaking phases as shown. AF insulator is antiferromagnetic insulator with the Néel temperature T_N, the pseudogap phase is shaded pink and is indicated below a crossover temperature T^*, the superconducting dome is marked with the superconducting transition temperature, T_c. The blue shaded dome, peaked at hole doping of $p = 0.125$ is the charge density wave order, which has been identified to compete with superconductivity. The pseudogap phase ends at p^* which has been recently identified as the putative QCP for Nd-LSCO. Ref. [9] for a detailed discussion. Figure adapted from Ref. [6] with permission.

2.3 Cuprate phase diagram

In the phase diagram shown in Fig. 2.2, the hole doping (p) is essentially the number of holes per Cu atom in the CuO_2 planes. Hole doping delocalizes the frozen electrons, destroying the long range antiferromagnetic ordering, however, the delicate balance between Coulomb repulsion and kinetic energy often lead to strong electronic correlations giving birth to a number of intertwined phases with comparable energy and temperature scales. Besides superconductivity, these comprise of charge density wave (CDW) order [19, 22, 23, 5], antiferromagnetism, electronic nematicity [12, 13, 14, 15, 17, 16] and possibly other orders such as pair density wave order [24]. In this thesis, we will primarily focus on charge ordering and electronic nematicity, investigating how they respond to hole doping and external tuning parameters like an in-plane uniaxial strain as an attempt to disentangle and study their connection with each other and, ultimately, with the superconducting state.

2.3.1 Charge ordering: Charge density wave (CDW) order

Unidirectional spin and charge order ('stripes') were first observed in the cuprates by neutron scattering measurements by Tranquada *et al.* in 1995 [5]. In the last decade, translational symmetry breaking charge ordering has been established as a generic phase in cuprates with experimental signatures observed in the underdoped regime and vanishing as the hole doping increases to optimal doping [22, 19, 26].

The family of La-based cuprates show strong suppression in the superconducting transition temperature, T_c, at the hole doping level of $p = 1/8$. There have been evidence for the competition of the superconducting phase with charge order in cuprates other than Nd-LSCO as well. For instance, application of a perpendicular magnetic field suppresses superconductivity and enhances CDW order in YBCO. The jury is still out for why $p = 1/8$ doping favors the stripe phase, and exhibits very strong suppression of superconductivity in some of the cuprates like LBCO.

First reports of CDW order detection in cuprates using RSXS come from measurements by Abbamonte *et al.* in 2005 [27]. This attracted more work using RSXS, and soon enough CDW order was discovered in YBCO [22, 19], now it is considered a generic member of the cuprate phase diagram. CDW order is evidenced by a broad and weak peak above the fluorescent background signal in resonant scattering at a particular $\boldsymbol{Q}$ value[1]. As shown in Fig. 2.3(b), the $\boldsymbol{Q}_{\text{peak}}$ value for $p = 1/8$ Nd-LSCO is (0.236, 0, 1,5), it tells us that the

[1] Around (±0.236 0 1.5) in La-based cuprates.

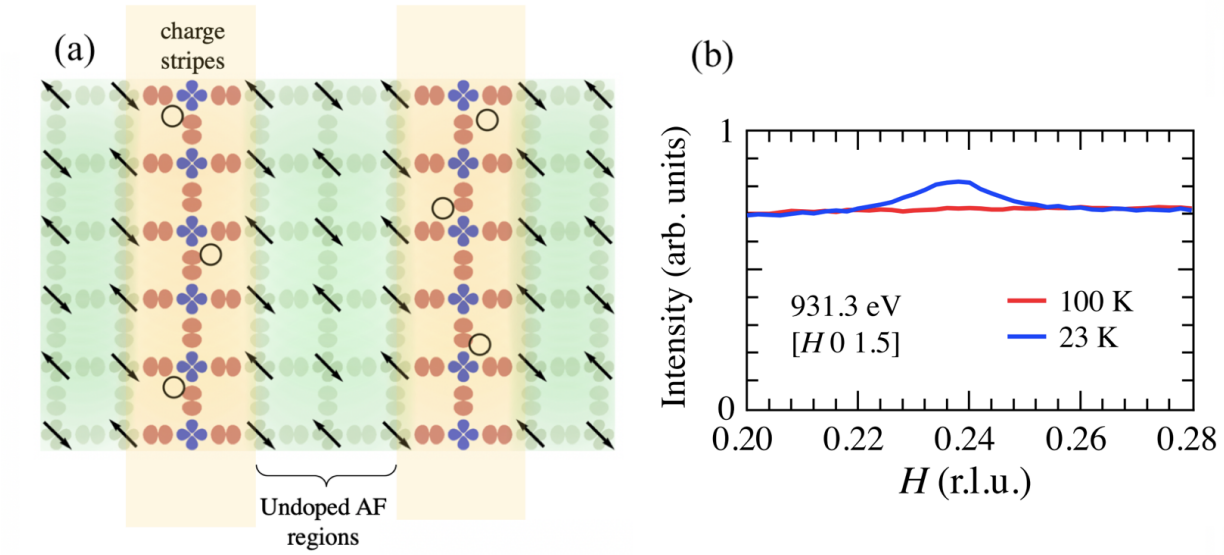

Figure 2.3: Unidirectional charge ordering in Lanthanum based cuprates: (a) Schematic of charge stripe order in Nd-LSCO at $p = 1/8$ hole doping. Spontaneous segregation of holes into unidirectional charge stripes occur, shown by orange shade. These stripes follow a (lattice) period-4 stripe-like charge correlations in the La-based materials. Undoped AF region in between are denoted by green shade, (b) Detection of a CDW signal in a La-based cuprate, Nd-LSCO at $p = 1/8$ hole doping, using RSXS performed at Cu L edge. Schematic (a) used with permission from [25]. Reprinted figure (b) with permission from Ref. [28]. Copyright (2013) by the American Physical Society.

periodicity of the charge superlattice is 4 times the lattice spacing. The broad character of the peak indicates the short range order with a correlation length of around 70 Å [28]. More details on the measurement and analysis of CDW order is presented in sections 5.5.2 and 6.4.2.

2.3.2 Structural low-temperature phases

An important aspect of La-based cuprates is a low-temperature orthorhombic (LTO) phase to low-temperature tetragonal (LTT) structural phase transition [29, 30, 31]. As shown in Fig. 2.4, the average structures of these phases can be described by the in-plane Cu atom coordinated by six oxygen atoms, such that it forms a grid of tilted, almost rigid, corner

sharing CuO_6 octahedra. Based on the hole doping levels and temperature, four structural phases are observed in Nd-LSCO: the high-temperature tetragonal (HTT) phase with space group $I4/mmm$, the low-temperature orthorhombic (LTO1) phase ($Bmab$), the low-temperature tetragonal (LTT) phase ($P4_2/ncm$) phase, as well as the LTO2 phase ($Pccn$) which is an intermediate phase between LTO and LTT with reduced orthorhombicity.

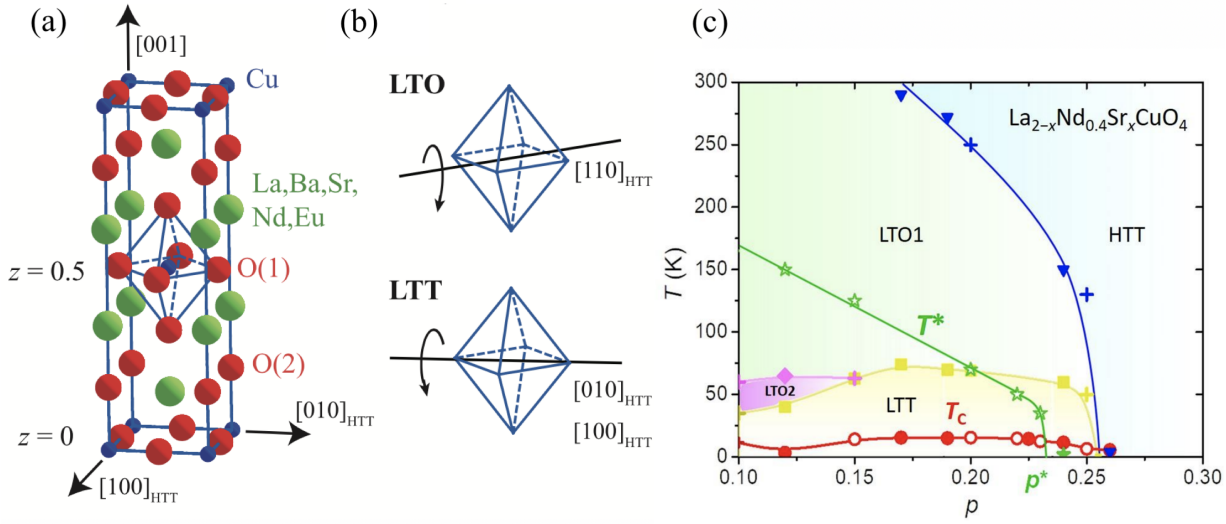

Figure 2.4: (a) Unit cell of Nd-LSCO in the high-temperature tetragonal phase (HTT). O(1) and O(2) are in-plane and apical oxygen sites, respectively. (b) is described in the text. (c) Structural phase diagram of Nd-LSCO with different structural phases as described in the text. (a) and (b) reused from Ref. [18] with permission. Phase diagram taken from [32].

At high temperatures, the CuO_2 layers are parallel to the *ab*-plane of the unit cell being in HTT structure. However, as one lowers the temperature, mismatch between the Cu-O and La-O bond lengths causes strain which is alleviated by structural distortions achieved by tilting of these octahedras. As a consequence, on cooling the space group changes, and the unit cell of the LTO phase is rotated by 45 degrees. As shown in Fig. 2.4, in the LTO phase the octahedra tilt along $[1\ 1\ 0]_{\mathrm{HTT}}$ direction, whereas in the LTT phase the tilt direction alternates between $[0\ 1\ 0]_{\mathrm{HTT}}$ and $[1\ 0\ 0]_{\mathrm{HTT}}$ from plane to plane [31].

In the LTT phase, the orientation of these distortions — which change direction by 90 degrees between adjacent layers — are crucial for stabilizing charge and spin order in the copper oxide plane [33]. Moreover, the axis about which the octahedra rotate is parallel

to an in-plane crystallographic axis, alternating between a and b in the adjacent layers [29, 30, 31]. This structural transition is known to induce the C_4 symmetry breaking of the average electronic structure within an individual CuO_2 plane [18].

2.3.3 Electronic nematicity

An electronic nematic phase occurs when the electronic structure breaks the rotational (point group) symmetry but leaves the translational (lattice group) symmetry intact. Experimental evidences include reports of electronic nematicity from bulk transport [12, 13, 14], scanning tunneling microscopy (STM) measurements [15, 16], and inelastic neutron experiments [17]. Recently our group identified electronic nematicity in cuprate superconductors [18] and its relationship to the crystal structure as well as the CDW order using resonant x-ray scattering. We investigated the $C_4 \rightarrow C_2$ rotational symmetry-breaking (electronic nematicity) of the average, intra–unit cell, electronic structure within an individual CuO_2 plane. The role of electronic nematicity, such as whether it is a feature of the pseudogap region and how it relates to CDW order or hole doping or the crystal structure of different cuprate families has not yet been fully established.

Our study uses resonant soft x-ray scattering (RSXS) measurements of the (001) Bragg peak to probe electronic nematicity in the in Nd-LSCO. Previous work by Achkar *et al.* [18] showed that the resonant x-ray scattering measurements of the (001) Bragg peak provide sensitivity to electronic nematicity. Understanding how this measurement reveals electronic nematicity requires examination of the crystal structure of Nd-LSCO. As discussed in the previous section, Nd-LSCO exhibits a structural phase transition from the LTO to LTT phase at temperatures between 50 – 90 K depending on doping. The LTT phase is characterized by tilting of the CuO_6 octahedra along the a or b axes such that each individual CuO_2 layer structurally breaks C_4 rotational symmetry as shown in Fig. 2.4. The axis of rotation of the octahedra, however, rotates by 90 degrees between neighbouring layers producing a crystal structure that is tetragonal, despite having orthorhombic layers. Consequently, any probe that bulk averages the layers would yield the same result along the a and b axes and not reveal nematic order. However, resonant x-ray scattering is sensitive to orbital symmetry, which differs for atoms in neighbouring layers in the LTT phase. Moreover, by tuning the photon energy to correspond to different atoms within the unit cell, the electronic symmetry breaking of the CuO_2 planes – which contain the Cu $3d$ and O $2p$ states that cross E_F and are most relevant to the low energy physics of the cuprates – can be differentiated from the La_2O_2 spacer layer, which do not have states that cross E_F but would be sensitive to changes in their orbital symmetry induced purely by structural distortions.

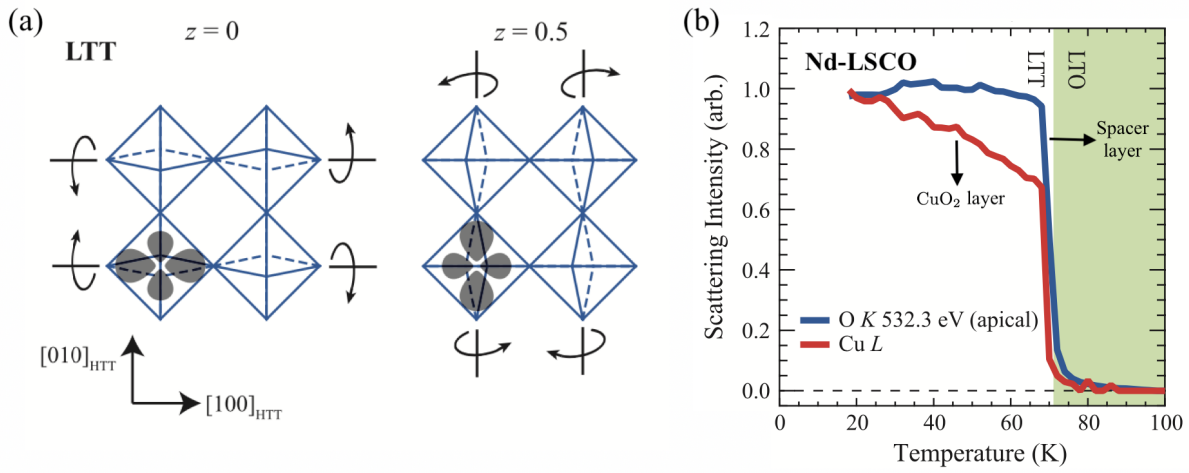

Figure 2.5: Electronic nematicity as a measure of orbital asymmetry: (a) CuO_2 planes showing the octahedral tilt pattern in neighboring layers ($z = 0$ and 0.5) in the LTT phase. The structural C_4 symmetry-breaking and electronic nematicity alternates between neighboring planes, $z = 0$ and $z = 0.5$. (b) Temperature dependency of the (001) Bragg peak at photon energy tuned to atoms in the CuO_2 layer and the spacer layer. The different temperature dependences can be understood in terms of an electronic nematic order in the CuO_2 planes that has a temperature dependent susceptibility and provides a contribution to the (001) peak intensity in addition to any contribution to that is induced by the lattice potential via structural distortions. (a) and (b) taken from Ref. [18] with permission.

2.3.4 Pseudogap and Quantum criticality

Rotational and translational symmetry-breaking phases in the pseudogap region have been established as generic and distinct features in the cuprate phase diagram using different probes. The pseudogap is a region below a crossover temperature T^*, where the electronic density of states is partially gapped, it is a trove of exotic electronic instabilities and ordering mechanisms. Opening up in the non-superconducting state, the pseudogap houses several symmetry-breaking phases, such as stripe-order [5], liquid electronic crystalline order, and the newest addition of a pair-density- wave (PDW) state [24]. The intertwined nature of these phases, both in energy and temperature, makes it challenging to tell whether the pseudogap is a distinct (ordered) phase or an amalgamation of different instabilities [9, 8] as we move across the phase diagram (along temperature and hole-doping axes). The electronic instabilities, unconventional superconductivity, and the pseudogap are believed

to be linked with the existence of a zero-temperature quantum critical point (QCP) similar to heavy-fermion, organic, pnictide [6, 34], and iron-based superconductors [35]; the last being the closest cousins to cuprates.

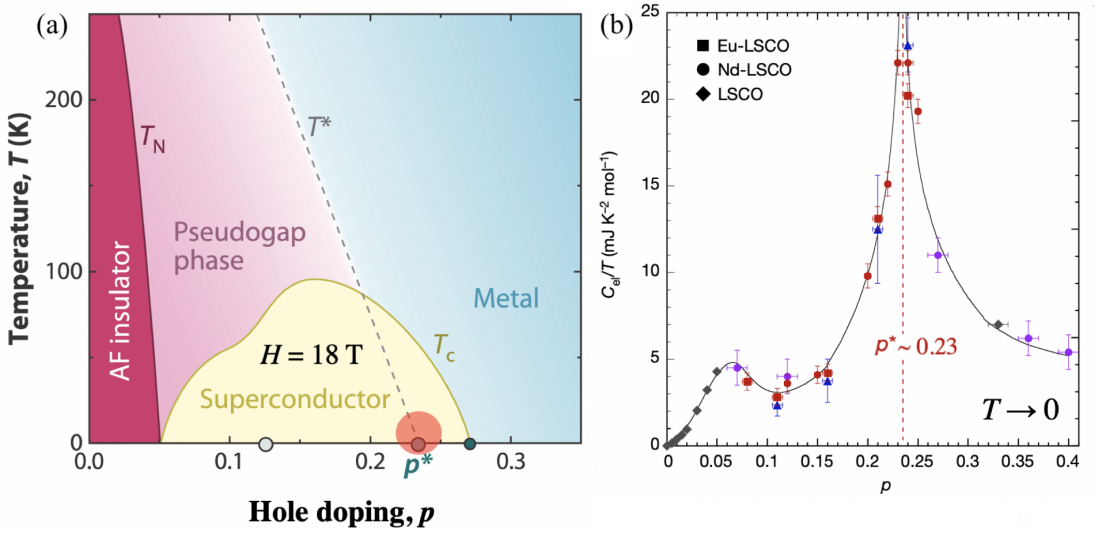

Figure 2.6: Evidence of quantum criticality in Nd-LSCO: A quantum critical point (QCP) occurs when the phase transition temperature of a material is suppressed to absolute zero. (a) shows the schematic phase diagram with the putative QCP at the point where the pseudogap phase ends. (b) High field resistivity measurements on La-based cuprates: Superconductivity is suppressed to sub-Kelvin temperatures by applying a magnetic fields in the samples to investigate the behavior of electronic specific heat with doping. The authors argue that the strongly peaked electronic specific heat at p^* which exhibits a $\log(1/T)$ dependence is a signature of a QCP in these materials. Image (a) adapted from [6] with permission and image (b) reused from [36] with permission.

Existing proposals and recent reports of this putative pseudogap QCP in different cuprate families — based on the change in carrier density [37], Fermi surface transformation [38, 39], torque-magnetometry measurements [40], strong mass enhancement via quantum oscillation studies [41], and specific heat measurements (see Fig 2.6) at low temperatures in large magnetic fields [36] — suggest the possibility of termination of electronically ordered phases, and transition to a Fermi liquid behavior, as we increase the hole doping. As depicted in Fig. 2.6, for Nd-LSCO the putative pseudogap QCP lies inside the superconducting dome around the hole doping of 0.23 [38]. It has been proposed that quantum fluctuations enhance superconducting pairing interactions in the vicinity of this

putative QCP [6, 41, 42]. There have been several theoretical and experimental attempts to understand the nature and finite-temperature implications of these posited fluctuations at the putative pseudogap QCP in cuprates [6, 41, 42, 43]. Recent advancements include reports of divergent nematic fluctuations using elastoresistance measurements[44] and enhanced electronic nematic fluctuations using Raman scattering [45] near the endpoint of the pseudogap phase, both suggesting the presence of a nematic quantum critical point.

2.4 Motivation for our studies

In $La_{1.6-x}Nd_{0.4}Sr_xCuO_4$ or Nd-LSCO, the putative pseudogap QCP lies, inside the superconducting dome, around the hole doping of 0.23 [38]. It has been proposed that quantum fluctuations enhance superconducting pairing interactions in the vicinity of this putative QCP [6]. This makes Nd-LSCO a suitable candidate for studying the relation between the three symmetry-breaking phase, that is CDW order, electronic nematic order and structural phase transitions. The existence of a low temperature tetragonal (LTT) distortions — a feature of this family — gives us access to the (001) peak which, as we will describe in the chapters ahead, is crucial for the measurement of electronic nematic order using our technique of resonant x-ray scattering.

We use resonant soft x-ray scattering (RSXS) — a technique that combines x-ray diffraction and x-ray absorption spectroscopy — at different photon energies allowing us to differentiate between ionic displacement and orbital asymmetry. This helps us address how static electronic orders might evolve as a function of hole doping. In this study, we focus on the relationship between electronic nematicity, charge density wave order and structural distortions.

Furthermore, with the freedom RSXS provides in choosing a transition edge, we can explore the impact of uniaxial strain on materials with different crystallographic structures, including materials that are 4-fold symmetric and do not intrinsically favour unidirectional charge ordering. In these systems, the application of strain may have a dramatic effect, potentially stabilizing long-range unidirectional charge. Uniaxial strain proves to be a useful way in understanding the role of directional crystal deformations — which influences the way how orbitals overlap in the neighboring sites and layers — in the correlated electronic states of matter. This selection allows us to decouple co-existing symmetry breaking phases providing a way to understand the behavior of the electronic structure under changing point group symmetries.

Chapter 3

Resonant Elastic X-ray Scattering

3.1 Introduction

Quantum materials is an umbrella term in condensed matter physics for materials that exhibit strong electronic correlations, ordering, and instabilities like superconductivity, charge/spin modulations, magnetic order, and other structural, electronic, and temporal symmetry breaking phases [9]. Often in these materials, the electronic correlations and ordered states are intertwined — competing, co-operating, and co-existing — with phases sharing similar energy and temperature scales [8]. Understanding the physics of intertwined electronic order in strongly correlated electron systems is of crucial importance to a wide range of materials, so are the techniques capable of probing and characterizing different co-existing degrees of freedom in such configurations.

In this thesis, we investigate (hole doped) transition metal oxide (TMO) heterostructures, which exhibit complex electronic phenomena involving competitive and/or cooperative ordering of various electronic degrees of freedom — for instance, density wave order, superconductivity, nematicity amongst others. In TMO, the collective ordering of charge, spin and orbital degrees, generally, affects a small portion of the valence electrons, thus most of the interesting physics occurs at low energies, close to the Fermi level of the transition metal ion involved. In condensed matter physics, conventional x-ray diffraction (XRD) is a well-established tool to probe the spatial, microscopic description of the underlying ionic/atomic structure and the degree of crystalline order, via measurement of the position and width of Bragg peaks. Since the atomic scattering cross-section for x-rays is proportional to Z^2, where Z is the atomic number, XRD signal is greatly influenced by heavier dopant atoms in the TMO heterostructures [46]. Thus forbidding us to resolve the physics

of the charge and orbital degrees of freedom happening close to the Fermi level for lighter elements like oxygen and copper.

Resonant elastic x-ray scattering (REXS) combines XRD with x-ray absorption spectroscopy, in such a way that gives us a probe which is not only sensitive to the structural features but also to the electronic structure: a technique that not only allows us to probe weak ordering phenomena that is otherwise difficult to detect, but also to identify and disentangle different orders (magnetic, lattice, charge, orbital), even when they overlap or occur simultaneously in time or temperature, by varying the x-ray energy and polarization. It works by tuning the incident photon energy to an x-ray absorption edge, i.e. an energy sufficient to excite a core electron of a particular element into an unoccupied state. Near an x-ray absorption edge, the resonant effect enhances the scattering amplitude which now varies strongly with photon energy and, unlike off resonance, depends on details of the electronic structure, such as the valence, spin state or orbital symmetry of the unoccupied electronic states. It is important to choose the transition edge such that it not only enhances the cross section but also keeps it in the low-energy range near the Fermi energy of the transition metal ion. In our case of the $3d$ TMOs, the most relevant dipole-allowed transition is from $2p$ to $3d$, also called the $L_{2,3}$ or L_3[1] edge, which lies between $100 - 2000$ eV — called the soft x-ray regime — thus adding the "soft" in the name of the technique resonant soft x-ray scattering (RSXS). For Copper the L_3 edge is at $E \sim 930$ eV, which is the backbone energy value of this thesis. It is worthwhile to mention that there is a small cost involved in this compromise: the wavelength range for soft x-rays drastically restricts the q-space access, we will briefly touch upon later in this chapter. On the other hand, even with larger q-space accessibility, the hard x-ray ($E > 5$ keV) would not be as useful in probing intertwined electronic correlated physics for the TMOs as they would probe/correspond to states above the Fermi level.

This chapter briefly covers the theoretical description of REXS and its application to probe orbital asymmetry. More rigorous treatment can be found in Ref. [46, 47, 48, 49].

3.2 X-rays and their interaction with matter

For the scope of this thesis, we will consider monochromatic beams – which travel perpendicular to the direction of the electric and magnetic field. For a simplistic theoretical treatment, we shall consider the electric field only, thus characterizing x-rays by a wavelength λ, or wavenumber $k = 2\pi/\lambda$. Interaction of an oscillating external field hold an

[1] Or colloquially L edge, when used with Cu in the later chapters.

important place in condensed matter physics via driving the underlying system's dynamics out of equilibrium. The response of the properties of the studied phase of matter contain key information about such excitations, which in a first principle consideration can be treated proportional to the external field (or oscillations). This is generally modeled with a linear response theory, we will borrow and build up from this idea in the sections ahead.

3.2.1 X-Rays: Waves, photons, and synchrotron

Assuming the x-ray beam is monochromatic and perfectly collimated, we apply the approximation of a plane wave. The classical description of the spatial and temporal variation of a linearly polarized, electromagnetic plane wave propagating along the z-axis can be expressed as

$$\boldsymbol{E}(\boldsymbol{r}, t) = \hat{\boldsymbol{\epsilon}}\ E_0 e^{i(\boldsymbol{k}.\boldsymbol{r}-\omega t)}, \tag{3.1}$$

where the $\hat{\boldsymbol{\epsilon}}$ and $\boldsymbol{k}$ contains information about the direction of polarization and wavevector, respectively.

3.2.2 Diffraction by an electronic distribution

We begin by considering non-resonant, elastic scattering of incident x-rays by a charge distribution. In general, an atom can be modeled as a spatial charge distribution with some radial dependence for electron density, as $\rho(\boldsymbol{r})$. With our approximation of incident x-rays as a plane wave front as described in Eqn. (3.1) — we can think of diffraction as the phase difference, $|(\boldsymbol{k}_{\text{out}} - \boldsymbol{k}_{\text{in}}) \cdot \boldsymbol{r}|$, caused by an unequal traversal of optical path length of two (or more) scattered wavefronts. The scattered wavefronts interfere constructively (and destructively) to give us a diffraction pattern. Often we formalize it with the momentum transferred, $\boldsymbol{q} = \boldsymbol{k}_{\text{out}} - \boldsymbol{k}_{\text{in}}$, to the scattered wavefront, and then integrating it over entire above-said charge distribution as

$$f(\boldsymbol{q}) = \int \rho(\boldsymbol{r}) e^{i\boldsymbol{q}\cdot\boldsymbol{r}} d\boldsymbol{r}, \tag{3.2}$$

where $f(\boldsymbol{q})$ is the atomic form factor. It is worthwhile to mention that the full atomic form factor, in the quantum mechanical treatment which we will see in the next section, depends on the energy of the incident photons, and consequently the binding energy response to it.

Building up from our simplistic treatment of atoms as scattering entities [50], we now consider crystals — that can be classified as structures composed of periodic arrangements

of atoms that, generally, form a Bravais lattice. We can now modify our Eqn. (3.2) to include the structural information by discretely summing over the lattice sites as

$$S(\boldsymbol{q}) = \sum_{\boldsymbol{R}} f(\boldsymbol{q}) e^{i\boldsymbol{q}\cdot\boldsymbol{R}}, \tag{3.3}$$

where $\boldsymbol{R} = n_1\boldsymbol{a}_1 + n_2\boldsymbol{a}_2 + n_3\boldsymbol{a}_3$ points to the location of the atom, and $\{\boldsymbol{a}_1,\ \boldsymbol{a}_2,\ \boldsymbol{a}_3\}$ are the primitive lattice vectors. The discrete Fourier transform $S(\boldsymbol{q})$ can be thought of as a crystal structure factor for a simple periodic arrangement. The scattering intensity $|S(\boldsymbol{q})|^2$ attains a maxima when the momentum transfer for the scatterers satisfy the Laue condition, $\boldsymbol{q}\cdot\boldsymbol{R} = 2\pi m$, where m is an integer.[2]

For a more realistic treatment of (complex) periodic arrangements with multiple atoms in each unit cell, we consider $\boldsymbol{R} = \boldsymbol{R}_n + \boldsymbol{r}_j$ where $\boldsymbol{R}_n$ points to the center of unit cell n and $\boldsymbol{r}_j$ locates the different atoms within the unit cell relative to $\boldsymbol{R}_n$. The updated structure factor can be written as:

$$S(\boldsymbol{q}) = \overbrace{\sum_{A,B,C\ldots}^{\boldsymbol{r}_j} f_j(\boldsymbol{q}) e^{i\boldsymbol{q}\cdot\boldsymbol{r}_j}}^{\text{unit cell structure factor}} \underbrace{\sum_{\boldsymbol{R}_n}^{N} e^{i\boldsymbol{q}\cdot\boldsymbol{R}_n}}_{\text{lattice part}}, \tag{3.4}$$

where $A, B, C\ldots$ are distinct atoms in the unit cell, and N is the total unit cells in the crystal. The scattering intensity $|S(\boldsymbol{q})|^2$ in Eqn. (3.4) can be considered as having lattice contribution from different unit cells, and contribution from different atoms within the unit cell. For our interest, in a real (single) crystal we can assume $N \to \infty$ thus making the lattice contribution proportional to a Dirac delta function, $\sum_{\boldsymbol{G}} \delta(\boldsymbol{q} - \boldsymbol{G})$. This brings us to the Laue condition for scattering, $\boldsymbol{q} = \boldsymbol{G}$. Another important observation to make is that the scattering intensity is dictated only by the unit cell structure factor in this assumption.

3.2.3 Crystalline arrangement: Real and Reciprocal space

A perfect crystalline form is a periodic repetition of a unit cell structure which in real space is defined by primitive lattice vectors in real space, or also called unit vectors of direct lattice as $\{\boldsymbol{a}_1,\ \boldsymbol{a}_2,\ \boldsymbol{a}_3\}$. For such a crystal, the condition for maxima of scattering

[2] This allows us to define a complete set of the reciprocal lattice vectors which according to crystal and geometry of the experiment — gives us accessible Miller indices or, as we colloquially call them, Bragg peaks.

intensity is repeated for Eqn. (3.3) when $\boldsymbol{q} \cdot \boldsymbol{R} = 2\pi m$, where m is an integer, and for Eqn. (3.4) when $\boldsymbol{q} = \boldsymbol{G}$. This Laue formulation allows us to define reciprocal space using real space primitive lattice vectors as

$$\boldsymbol{b}_i = 2\pi \frac{\boldsymbol{a}_j \times \boldsymbol{a}_k}{v_0}, \tag{3.5}$$

where v_o is the volume of the unit cell, and $\{i, j, k\}$ are indices of direct lattice unit vectors, and they follow right-handed cyclic notation.

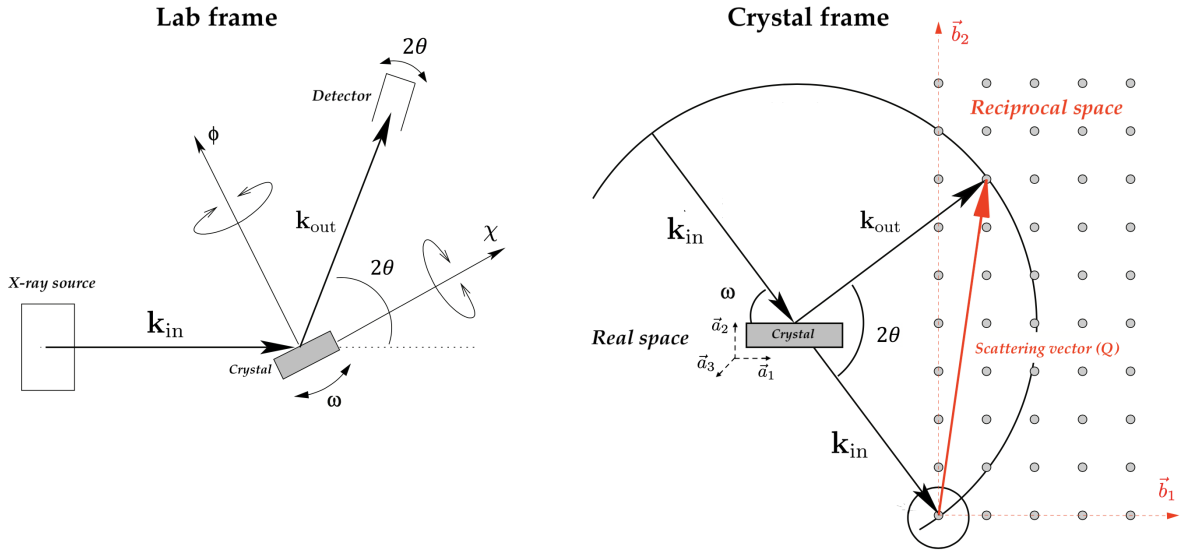

Figure 3.1: The scattering geometry in the lab and crystal frame, where $\{\boldsymbol{a}_1, \boldsymbol{a}_2, \boldsymbol{a}_3\}$ denote the direct lattice unit vectors, and $\{\mathbf{b}_1, \boldsymbol{b}_2\}$ stand for the reciprocal space unit vectors. The red solid line denotes the scattering vector, $\boldsymbol{q} = \boldsymbol{k}_{\text{out}} - \boldsymbol{k}_{\text{in}}$.

More generally from $\boldsymbol{q} = \boldsymbol{G}$, the set of reciprocal space vectors can be represented in these three equations:

$$\boldsymbol{a}_1.(\boldsymbol{k}_{\text{out}} - \boldsymbol{k}_{\text{in}}) = 2\pi h, \tag{3.6}$$
$$\boldsymbol{a}_2.(\boldsymbol{k}_{\text{out}} - \boldsymbol{k}_{\text{in}}) = 2\pi k, \tag{3.7}$$
$$\boldsymbol{a}_3.(\boldsymbol{k}_{\text{out}} - \boldsymbol{k}_{\text{in}}) = 2\pi \ell, \tag{3.8}$$

where h, k, ℓ are Miller indices and $G = h\boldsymbol{b}_1 + k\boldsymbol{b}_2 + \ell\boldsymbol{b}_3$, here $\{\boldsymbol{b}_1, \boldsymbol{b}_2, \boldsymbol{b}_3\}$ form the basis vectors of the reciprocal space.

3.3 Theory of Resonant X-ray Scattering

3.3.1 A second order process

Resonant x-ray scattering is a "photon in-photon out" technique, where light (photon) gets scattered by matter (electron cloud) — the photon energy is tuned exactly to match the energy difference between the occupied (electronic) state and the unoccupied valence state. In this two step process, a 'hole' is left behind which interacts with other (un)occupied states to gain stability. As depicted in the cartoon Fig. 3.2 when the photon energy is off-resonance the excitation process does not involve an intermediate state Ψ_m where the absorption and the scattering cross section is dramatically low, however, as we tune to the resonant energy there is a strong enhancement of the scattering cross section, which now picks up information about the correlated ordering and symmetry-breaking phenomenon (involving the d orbital states of the transition metal ion of the TMOs).

3.3.2 A quantum mechanical approach

As discussed in Ref. [47, 51, 52], for our description of resonant scattering, we can obtain a time-dependent, matter-radiation interaction Hamiltonian as

$$H_{\text{int}} = \sum_{\text{electrons}} \overbrace{\frac{e^2}{2mc^2}\boldsymbol{A}^2}^{\substack{\text{Thompson}\\ \text{scattering}}} - \overbrace{\frac{e}{mc}\boldsymbol{p}\cdot\boldsymbol{A}}^{\substack{\text{Resonant}\\ \text{scattering}}}, \tag{3.9}$$

the vector potential $\boldsymbol{A}(\boldsymbol{r}, t)$ of the incident photon interacts with the electrons in the material, $\boldsymbol{p}$ is the momentum operator, and m is the mass of the electron.

We begin by considering the interaction of an incoming photon with an electronic configuration (ground) state $|\Psi_{\text{GS}}\rangle$, or simply $|G\rangle$ (see Fig. 3.2 as well). In REXS, the incoming photon absorption with wavevector ($\boldsymbol{k}$) and polarization ($\boldsymbol{\epsilon}$) causes the electrons to transition out of state $|G\rangle$ into an intermediate state $|\Psi_m\rangle$, or $|I\rangle$ which then decays back to the initial state $|G\rangle$ by emitting a photon ($\boldsymbol{k'}, \boldsymbol{\epsilon'}$). The introduction of the intermediate state $|I\rangle$ is crucial as it makes the probe sensitive to the electronic transition and electronic/charge structure of the ground state — this is different from the Thompson (elastic) scattering in which no electronic transition would be involved. These two cases are depicted by the cartoon schematics in Fig. 3.2.

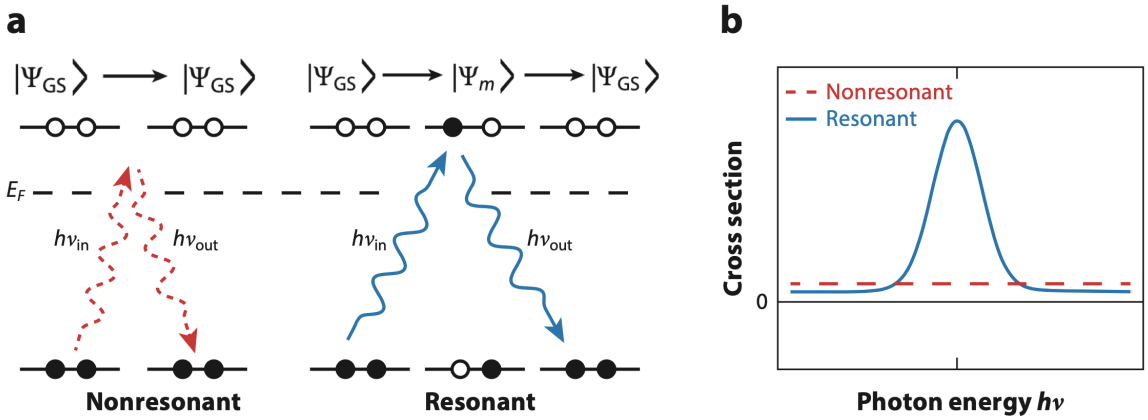

Figure 3.2: Schematic representation of resonant and nonresonant scattering: (a) In nonresonant scattering the excitation process does not involve intermediate states, whereas resonant scattering occurs when the incident photon energy ($h\nu_{\text{in}}$) is tuned to promote an electronic transition from the ground state $|\Psi_{\text{GS}}\rangle$to an intermediate state $|\Psi_m\rangle$. The subsequent, or the second order process of recombining of the excited electron with the core hole results in the creation of an outgoing (scattered) photon (with energy $h\nu_{\text{out}}$). (b) The different photon energy dependence of resonant and nonresonant processes, showing enhancement in the cross-section occurring at the resonant edge. Figure taken from [26] with permission.

To investigate the process in terms of transition matrix and scattering cross-section, we apply the Hamiltonian in Eqn. (3.9) on $|G\rangle$. In order to do so, we first choose a Coulomb gauge, $\boldsymbol{\nabla \cdot A = 0}$ to introduce a quantized photon vector field potential $\boldsymbol{A(r}, t)$ that has the form of a traveling wave as

$$\boldsymbol{A}(\boldsymbol{r}, t) = \sqrt{\frac{2\pi\hbar c}{V|\boldsymbol{k}|}} \sum_{\boldsymbol{k}} \boldsymbol{\epsilon} \left(a_k(t) e^{i\boldsymbol{k}\cdot\boldsymbol{r}} + a_k^\dagger(t) e^{-i\boldsymbol{k}\cdot\boldsymbol{r}} \right), \tag{3.10}$$

where $a_{\boldsymbol{k}}^\dagger$ and $a_{\boldsymbol{k}}$ are photon creation and annihilation operators respectively. The vector potential introduced above is linear in annihilation and creation operators which means to obtain a second order elastic process, it would have to act twice on $|G\rangle$. This implies that allowed terms quadratic in $\boldsymbol{A}$ would contribute to first order and the contribution of allowed linear order terms in $\boldsymbol{A}$ would need second order perturbation theory treatment to capture the two-step resonant elastic scattering process. We rewrite Eqn. (3.9) by separating the

Hamiltonian into a non-resonant (H_1) and a resonant (H_2) scattering contribution, summed over all electrons labeled via i:

$$H_{\text{int}} = H_1 + H_2 = \overbrace{\sum_i \frac{e^2}{2mc^2}\,[\boldsymbol{A}(\boldsymbol{r}_i,t)]^2}^{H_1:\ |G\rangle\to|G\rangle} \;-\; \overbrace{\sum_i \frac{e}{mc}\,\boldsymbol{p}_i\cdot[\boldsymbol{A}(\boldsymbol{r}_i,t)]}^{H_2:\ |G\rangle\to|I\rangle\to|G\rangle}. \tag{3.11}$$

We calculate the transition rate matrix [46, 47, 53] for H_1 and H_2, as:

$$T_1 = \langle G|H_1|G\rangle \quad \text{and} \quad T_2 = \sum_m \frac{\langle G|H_2^*|I_m\rangle\,\langle I_m|H_2|G\rangle}{\hbar\omega_{\boldsymbol{k}} - (E_m - E_g) + i\Gamma/2}. \tag{3.12}$$

plugging in H_1 and H_2 we get:

$$T_1 = \frac{hc}{V|\boldsymbol{k}|}\frac{e^2}{mc^2}\,(\boldsymbol{\epsilon}^*\cdot\boldsymbol{\epsilon})\sum_i \langle G|e^{i(\boldsymbol{k}-\boldsymbol{k}')\cdot\boldsymbol{r}_i}|G\rangle\,, \text{and} \tag{3.13}$$

$$T_2 = \frac{hc}{V|\boldsymbol{k}|}\frac{e^2}{mc^2}\sum_{m\ \text{states}} \frac{\langle G|\sum_{j=1}^N \boldsymbol{\epsilon}'^*\cdot\boldsymbol{p}_j e^{-i\boldsymbol{k}'\cdot\boldsymbol{r}_j}|I_m\rangle\,\langle I_m|\sum_{j'=1}^N \boldsymbol{\epsilon}\cdot\boldsymbol{p}_{j'} e^{i\boldsymbol{k}\cdot\boldsymbol{r}_{j'}}|G\rangle}{\hbar\omega_{\boldsymbol{k}} - (E_n - E_g) + i\Gamma/2}. \tag{3.14}$$

Note that the system transitions from the ground state $|G\rangle$ with energy E_g to an intermediate state $|I_m\rangle$ with energy E_m, and Γ represents the full-width at half-maximum of the distribution of all possible intermediate states I_m with respective energies — more commonly known as the lifetime of the intermediate states. The transition rate[3] in this quantum mechanical treatment can be described using perturbation theory by Fermi's Golden Rule, as:

$$w = \frac{2\pi}{\hbar}\,|T_1 + T_2|^2\,\delta\left(\hbar\omega_{\boldsymbol{k}} - \hbar\omega_{\boldsymbol{k}'}\right). \tag{3.15}$$

We sew up these arguments together by considering a scattering photon flux $\Phi = cn_k/V$ where n_k is the number of photons with wavevector $\boldsymbol{k}$ in a solid angle $\mathrm{d}\Omega$ which then gives us the differential scattering cross section as $d\sigma/d\Omega = w/\Phi$. Last point to note is the conversion of delta function to a differential element dE to sum over photons with all k.

[3] The probability that an electron will undergo a transition per unit time from one state to another.

Finally, we obtain:

$$\frac{\mathrm{d}\sigma}{\mathrm{d}\Omega} = \frac{e^4}{m^2c^4}\left|(\boldsymbol{\epsilon}^*\cdot\boldsymbol{\epsilon})\overbrace{\sum_i \langle G|\, e^{i(\boldsymbol{k}-\boldsymbol{k}')\cdot\boldsymbol{r}_i}\,|G\rangle}^{\mathcal{F}(\boldsymbol{Q})}\right. \\ \left. + \sum_{m\ \text{states}} \frac{\langle G|\sum_{j=1}^N \boldsymbol{\epsilon}'^*\cdot\boldsymbol{p}_j e^{-i\boldsymbol{k}'\cdot\boldsymbol{r}_j}\,|I_m\rangle\,\langle I_m|\sum_{j'=1}^N \boldsymbol{\epsilon}\cdot\boldsymbol{p}_{j'} e^{i\boldsymbol{k}\cdot\boldsymbol{r}_{j'}}\,|G\rangle}{\hbar\omega_{\boldsymbol{k}} - (E_m - E_g) + i\Gamma/2}\right|^2. \tag{3.16}$$

where $\mathcal{F}(\boldsymbol{Q})$ is the Fourier transform of the charge density, $\rho(\boldsymbol{r})$. In the above equation, the first term is the differential scattering cross section contribution from non-resonant Thompson scattering — which also follows the general relation between the scattering length and differential cross-section for non-resonant scattering processes. The second term in Eqn. (3.16) is the resonant (charge) scattering differential cross-section. At resonance the magnitude of the scattering intensity dramatically increases (see Fig. 3.2(b)), thus the measured intensity of a diffraction peak at resonance is dominated by the resonant contribution from the scattering cross-section. Naturally, there is an added background intensity that comes from the non-resonant processes. We can further simplify the second term by using the dipole approximation by Taylor expanding the exponential terms, as

$$e^{i\boldsymbol{k}\cdot\boldsymbol{r}} \simeq (1 + \boldsymbol{k}\cdot\boldsymbol{r} + (\boldsymbol{k}\cdot\boldsymbol{r})^2/2 + ...). \tag{3.17}$$

In our investigations, using REXS for orbitals and charge textures, only the first-order terms contribute significantly[4]. Furthermore, we can re-write the momentum operator using the commutator identity $\boldsymbol{p} = \frac{m}{i\hbar}\boldsymbol{r}(E_m - E_g)$ and after dropping higher order terms, the final expression for the differential cross-section of resonant scattering can be simplified as:

$$\left(\frac{\mathrm{d}\sigma}{\mathrm{d}\Omega}\right) \propto \left|(\boldsymbol{\epsilon}'\cdot\boldsymbol{\epsilon})\ \mathcal{F}(\boldsymbol{Q}) + \sum_{m\ \text{states}} \frac{\langle G|\,(\boldsymbol{\epsilon}'\cdot\boldsymbol{D})^\dagger\,|I_m\rangle\,\langle I_m|\,(\boldsymbol{\epsilon}\cdot\boldsymbol{D})\,|G\rangle}{\hbar\omega_{\boldsymbol{k}} - (E_m - E_g) + i\Gamma/2}\right|^2, \tag{3.18}$$

where $\boldsymbol{D} = \sum_j \boldsymbol{r}_j$ is the dipole operator. Note from the denominator in Eqn. (3.18) that resonant scattering will be amplified at energies where one can virtually excite an electron into some intermediate state, i.e. at an absorption edge. The differential cross section represented by Eqn. (3.18) relates to the atomic scattering form factor, $f(\omega)$, as

$$\left(\frac{\mathrm{d}\sigma}{\mathrm{d}\Omega}\right) \propto |f(\omega)|^2 \tag{3.19}$$

[4]Interested reader might find multipole expansion in Ref. [47, 54].

Thus $f(\omega)$, which is a complex quantity should vary and be enhanced in proximity to the absorption edge. This is, indeed, observed in the experiments as shown in Fig. 3.3. Re-examining the quantum mechanical treatment[5] in terms of atomic scattering form factors proves to be useful as the x-ray absorption spectroscopy (XAS) measurements not only exhibit enhancement but also become sensitive to the orbital, charge and spin degrees of freedom at the absorption edges. Furthermore, the polarization dependence of Eqn. (3.18) can be taken into account by using a tensor formulation of $f(\omega)$, as discussed in the next section.

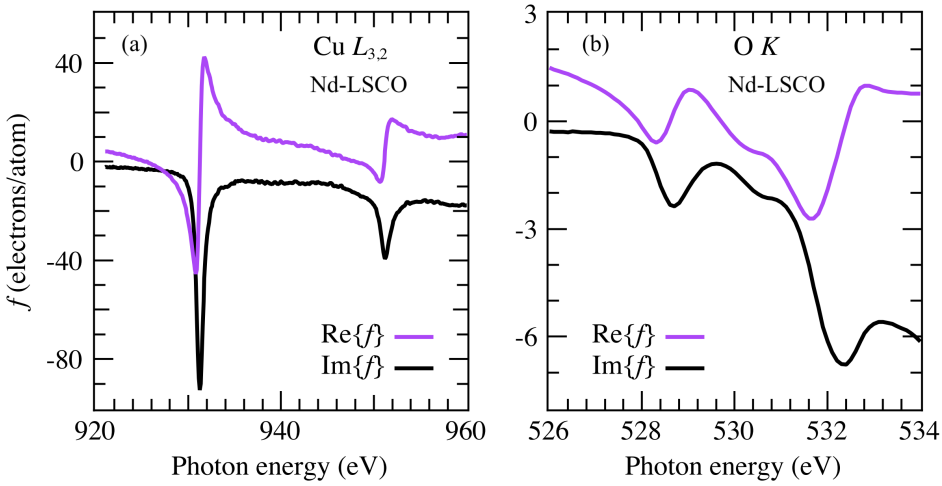

Figure 3.3: The atomic scattering form factors, $f(\omega)$, as a function of photon energy through the (a) Cu L and (b) O K absorption edges for Nd-LSCO determined from the XAS measurements. Figure reprinted from Ref. [28] with permission. Copyright (2013) by the American Physical Society.

3.3.3 Scattering tensor: Symmetry and orbital sensitivity

As described in the previous section, near an x-ray absorption edge, the resonant effect enhances the scattering amplitude which now varies strongly with photon energy and, unlike off resonance, depends on details of the electronic structure, such as the valence, spin state or orbital symmetry of the unoccupied electronic states. The absorption coefficient is peaked at this (resonance) energy because a transition is now allowed from an occupied

[5] A more rigorous connection is explored in Ref. [55].

core state to an unoccupied state. The peaks in the absorption spectra exhibit sensitivity to the unoccupied holes. For instance, the Cu L edge ($2p \rightarrow 3d$) probes unoccupied $3d$ states, the O K edge ($1s \rightarrow 2p$) probes unoccupied $2p$ states and the La, Ba, Eu or Nd M edges ($3d \rightarrow 4f$) probe unoccupied $4f$ states.

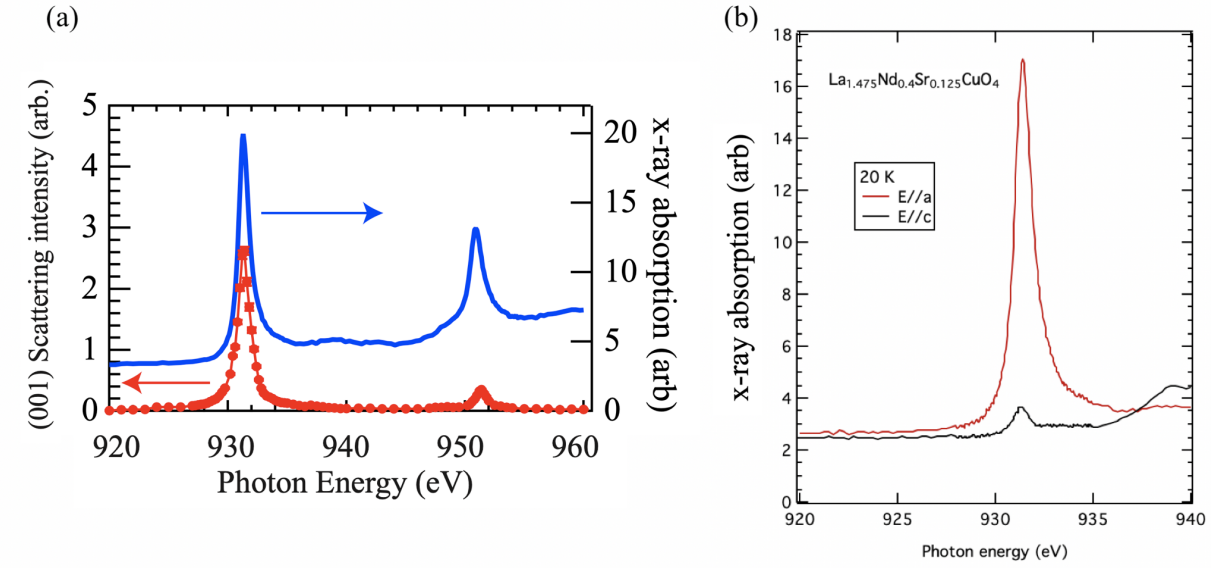

Figure 3.4: On resonance orbital sensitivity in REXS. (a) Enhancement of x-ray scattering on resonance: The resonant x-ray scattering intensity (red) and x-ray absorption (blue) as a function of incident photon energy through the Cu L absorption edge (2p to 3d transition) for the (001) Bragg peak of LBCO. (b) Polarization dependence of the x-ray absorption signal along different crystallographic directions (a and c), showing a large enhancement with polarization direction — indicating that it develops sensitivity to not only the hole occupation but also the symmetry of the holes associated with Cu $3d_{x^2-y^2}$ orbitals here. Figure (a) taken from the supplementary material of Ref. [18] with permission and figure (b) is from the data collected by previous members of our group.

In multi-ion electronic environment configurations, like tetragonal, octahedral, or orthorhombic coordinations, not only does the system break atomic/ionic spherical symmetry but also influences the way it scatters light. This anisotropy depends on the incident photon energy and polarization of the light, which can be encapsulated by a tensor representation.

The atomic scattering form factor can be treated as a tensor quantity [56] like

$$I \propto \left(\frac{\mathrm{d}\sigma}{\mathrm{d}\Omega}\right) \propto \left| \sum_j (\boldsymbol{\epsilon}_{\mathrm{in}}^{\dagger} \cdot \hat{f}_j(\omega) e^{i\boldsymbol{q}\cdot\boldsymbol{r}_j} \cdot \boldsymbol{\epsilon}_{\mathrm{out}}) \right|^2, \tag{3.20}$$

where $\boldsymbol{\epsilon}_{\mathrm{in}}$ and $\boldsymbol{\epsilon}_{\mathrm{out}}$ are incident and scattered photon polarization.

For a Cu $3d_{x^2-y^2}$ orbitals, involved at energies for Cu L edge, the scattering tensor would obey certain symmetries. The off diagonal elements would be zero, while the x and y components would be identical. In a similar way, one can qualitatively think that for a p_x (or p_y) orbital, the x component would be finite and the y component would be zero. The polarization dependence of the x-ray absorption signal, in Fig. 3.4, depicts that as we move the polarization of incident light along different crystallographic axes — we become sensitive to the symmetry of these holes. Thus, on resonance, RSXS develop sensitivity to hole occupation as well as the symmetry of the holes, to further access orbital symmetry.

For a general triclinic system we can write the scattering tensor (at atomic sites j) as:

$$\hat{S}(\boldsymbol{q},\omega) = \sum_{j \text{ sites}} \hat{f}_j(\omega) e^{i\boldsymbol{q}\cdot\boldsymbol{r}_j} \sim \begin{pmatrix} f_{xx}(\omega) & f_{yx}(\omega) & f_{zx}(\omega) \\ f_{xy}(\omega) & f_{yy}(\omega) & f_{zy}(\omega) \\ f_{xz}(\omega) & f_{yz}(\omega) & f_{zz}(\omega) \end{pmatrix},$$

where the components of $\hat{f}$ are complex. For system of our interest, like tetragonal and orthorhombic symmetries: resonant charge scattering contributions would contribute to the diagonal elements whereas magnetic scattering contributions can be present at both diagonal and off-diagonal terms of the scattering tensor. Furthermore, the polarization and the diagonal elements of the scattering tensor can give us information about the orbital asymmetry, by investigating the azimuthal dependence of the ratio of two incident photon polarization. That is to say, different types of order would have different azimuthal dependence. We will briefly discuss distinguishing between different ordering phenomena in Chapter 5 — once we have introduced which Bragg peaks correspond to what symmetry breaking. Thus, REXS is a combination of structural and electronic probes giving us a novel way to investigate complex strongly correlated systems with co-existing phases by tuning the photon energy and incident photon polarization.

Chapter 4

Synchrotron radiation and experimental setup

4.1 Introduction

The progress of resonant x-ray scattering as a technique has been greatly influenced by the development of synchrotron radiation light sources — which very generally can be classified as experimental megastructures that accelerate an electron at relativistic speeds in a circular orbit[1]. In the last half century, there have been 4 generations of synchrotrons, in this thesis we would focus on the experiments performed on 3^{rd} generation of synchrotron radiation at the Canadian Light Source (CLS), Saskatoon.

The reason resonant scattering experiments are usually performed at a synchrotron is because of their capability in generating highly resolved spatial and spectral distribution of the photon flux (x-rays beam) with tunable energy and polarization — which makes it an ideal source to detect signal intensities off and on-resonance — for both soft and hard x-rays. A schematic diagram of a synchrotron is shown in Fig. 4.1. The electrons are forced to stay in circular orbit via the use of insertion devices which are basically arrangement of magnets producing magnetic fields in alternating directions, making the electrons follow an oscillatory path. There are dimensionless parameters associated with these insertion devices that dictate which harmonics and wavelengths are enhanced. After a series of insertion devices and bending magnets, the synchrotron radiation is transmitted to the beamlines, or the respective endstations.

[1] With the exception of the 4^{th} generation sychrotrons: Free electrons lasers which are linear accelerators.

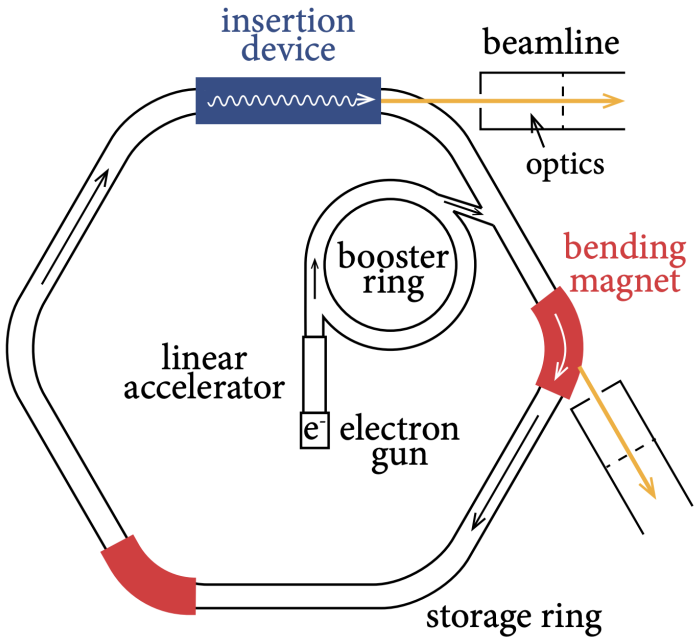

Figure 4.1: A schematic diagram of a synchrotron radiation source. Figure reused from Ref. [57] with permission.

4.1.1 REIXS beamline at the CLS

The resonant scattering experiments presented in this thesis were carried out at the REIXS (Resonant Elastic and Inelastic X-ray Scattering) beamline at the Canadian Light Source (CLS) in Saskatoon, Canada. Before reaching the ultra-high-vacuum (UHV) chamber — where the actual experiment is performed[2] — the synchrotron radiation passes through a sophisticated optical arrangement containing a monochromator and exit slits. This optical configuration at our REIXS beamline houses a variable line spacing plane grating monochromator, with different gratings and coatings on a plane mirror to optimize flux at photon energies spanning the full energy range of the beamline.

In Fig. 4.2, we see the main scattering chamber for resonant elastic scattering. After passing through the monochromator and exit slits, the (soft) x-rays from the REIXS beamline enter this chamber. The sampleholder is mounted on an in-vacuum four-circle diffractometer [58] — that not only allows us to align the beam onto the sample under investigation but also access the desired Bragg peak. To the left is the load lock and the transfer arm which can be used to store and transfer samples into the scattering chamber. To change/load samples first the samples are transfered to the load lock with the help of a transfer arm which has pincers at the end to catch the sampleholder, then the pressure of the load lock is either increased or decreased depending on whether the sample is to be taken out or loaded. There are valves present to make sure the pressure between the different sections of this assembly to avoid an abrupt breaking of the vacuum. The pressure changes are made possible through a series of pumps with specialized working pressure ranges. At the top is a cryostat which is connected to the sampleholder with copper braids too achieve cooling down to low temperatures. The base temperature for measurements in this thesis lies between 20 to 25 Kelvin.

4.1.2 Diffractometer geometry and motion stages

The sample to be studied is mounted on the sampleholder as shown in Fig. 4.3. Theoretically, there are six motors (or degrees of freedom) available within limits.[3] The x, y, and

[2]The main chamber at REIXS beamline as well as the storage ring is maintained under UHV with pressures less than 10^{-9} Torr. This is done not only to prevent the deposition of contaminants of sensitive optical instruments but also to maintain mean photon path of soft x-rays which is suscpetible to even low pressures.

[3]This is done to give more flexibility to the user during the sample alignment process, for example to center the notorious in-plane Bragg peaks at the desired detector. Apart from alignment, it also gives accessibility to more $\boldsymbol{q}$ addresses in the reciprocal space.

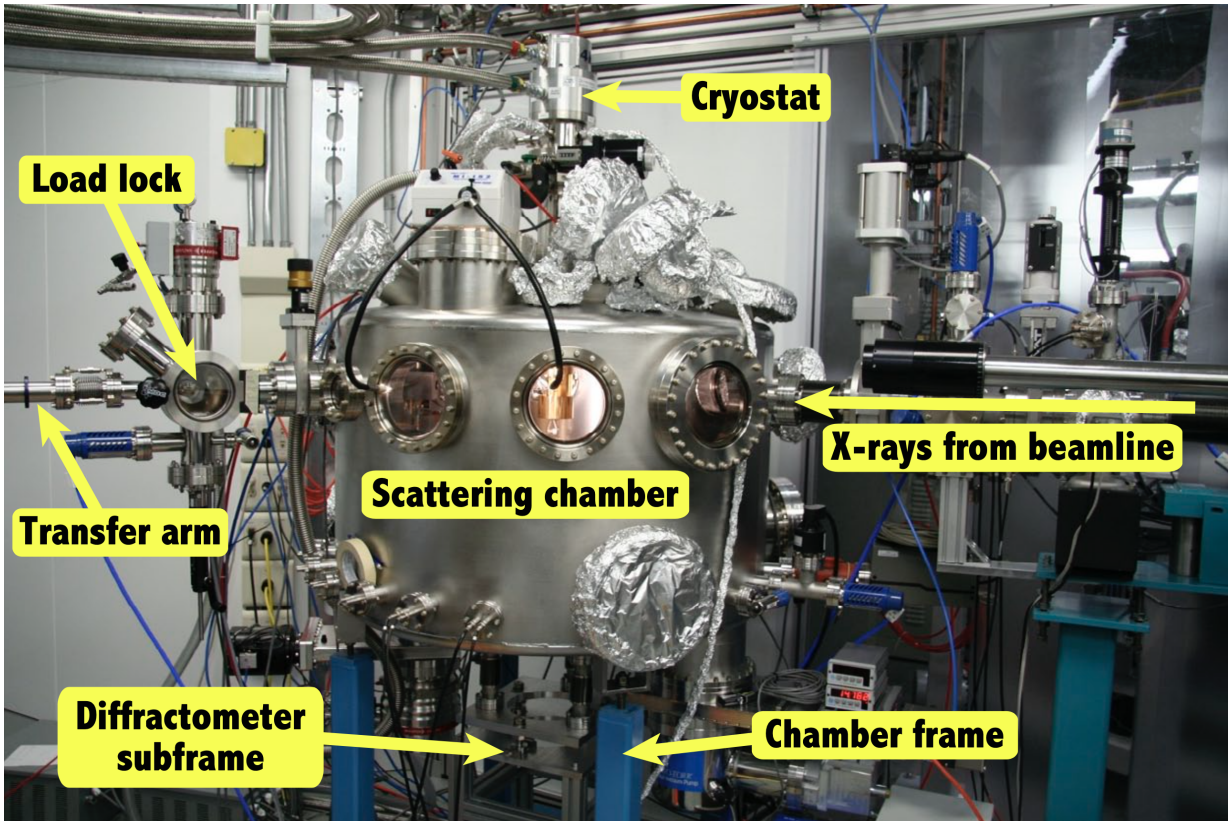

Figure 4.2: The RSXS scattering chamber at the CLS's REIXS beamline. Image reused from Ref. [25] with permission.

z stages/motors can achieve translations of ± 7.5 mm, however χ and ϕ motors can access motions of $\pm 7°$. The main action happens through $\theta - 2\theta$ scans — which are essentially synchronous and restricted motion of the θ[4] and 2θ motors in such a way that it corresponds to the desired reciprocal space scans. Figure 4.3 shows how a different combinations of real space motor movement help us navigate different directions in the reciprocal space depending on the incident photon energy, distance to the detector other than the θ and 2θ motor positions.

Our RSXS measurements, or any diffraction measurement for that matter, would involve scanning q-values in reciprocal space. Over time, some of these scans, as shown in Fig 4.3(b), have picked up colloquial names. A scan with a θ motor is called a rocking scan

[4]Sometimes called the ω motor. This is done to avoid the confusion that 2θ is twice the θ — which only holds for the (00ℓ) scans.

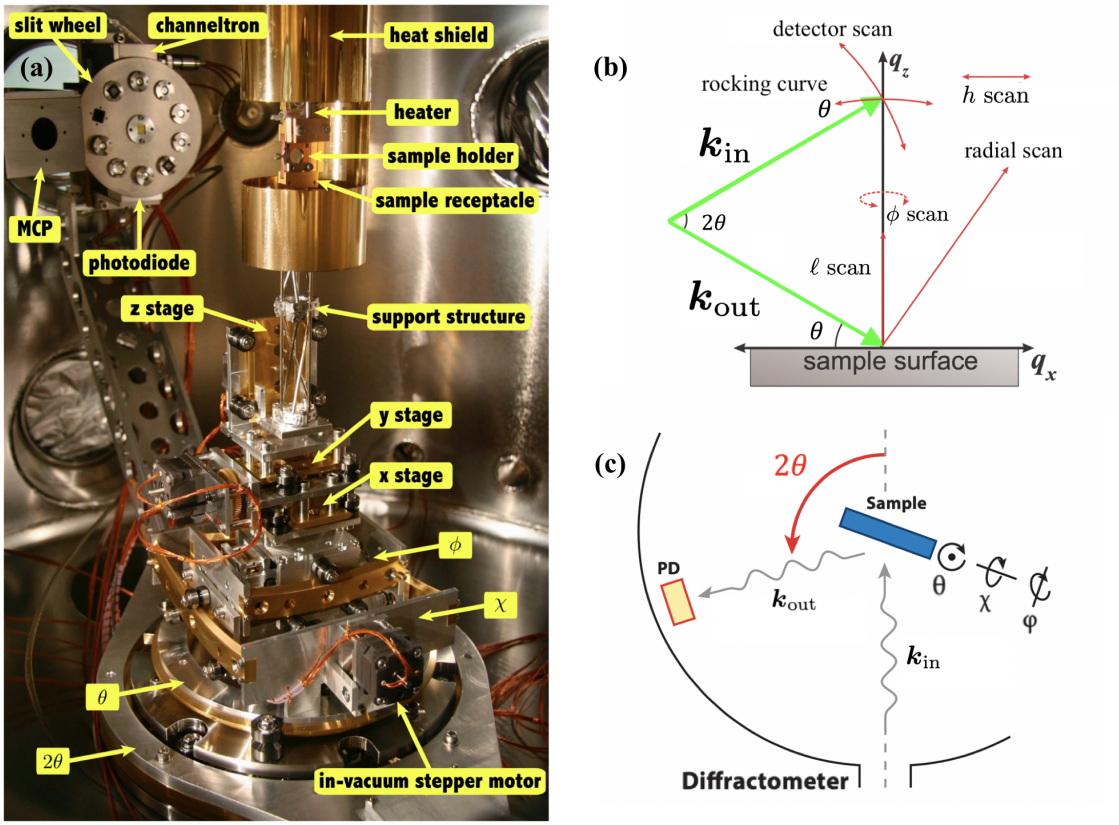

Figure 4.3: Motion stages and scattering geometry: (a) The four-circle diffractometer assembly in the RSXS scattering chamber, (b) Schematic diagram of the translations of real space motions to their corresponding reciprocal space scans, (c) Schematic diagram of the top view of the four-circle diffractometer assembly. Figure (a) reused from Ref. [25] with permission. Figure (c) adapted from Ref. [26] with permission.

— which is important in checking if the crystal has multiple domains. Similarly, centering the detector with the aid of a 2θ motor is often referred to as detector scan.

Another important technical aspect of this sample receptacle/holder assembly is the change in sample position, or equivalently the location of the beam on the sample surface with change in temperature. This thermal expansion (contraction) effect is not only minimized but also channeled along the θ and z motion stages — where it can be balanced by re-centering the corresponding Bragg peak — with the help of the support structure consisting of oblique thin-walled stainless steel tubing.

4.1.3 Detectors and signal scans

In the scattering chamber, there are detectors attached to the 2θ arm. The data collection in the upcoming chapters include the usage of a micro-channel plate (MCP), a silicon drift detector (SDD), a photodiode (PD), and a channeltron (ChT). The approximate distance of these detectors is 30 cm from the sample position. The MCP detector provides single-event counting, 2D position sensitive detection of soft x-ray photons, it has a diameter of about 25 mm. This becomes very useful in aligning the Bragg peak, and detecting weaker signals over the entire active area, for instance, a charge ordering signal (as described in section 2.3.1) has a wider and weaker spread in q-space, and is still easily recorded via a h-scan. The PD is sensitive to a large range of photon energies with a linear response for higher photon energies, this makes it suitable for the high flux of the direct beam or an x-ray fluorescence measurement. A slit wheel containing different filters and slits gives the control over the energy resolution and intensity saturation of the signal based on the incoming flux. The SDD measures the energy range of an incoming photons, and is suitable for low-energy x-rays providing a decent energy resolution for high count rates, the peaking time can be changed to avoid saturation of the signal.

4.2 Sample Preparation

Before performing the experiment at the synchrotron, there are certain things to be taken care of, like: a clean surface, properly mounted samples on a sampleholder (that will eventually fit the sample receptacle at the CLS), and most importantly well-aligned reciprocal axes for the Bragg peak to be studied. The last part is crucial because as we mentioned in section 3.1, RSXS has limited access to the q-space unlike the hard x-rays. Other factors that needs proper characterization include, possible twinning or mosaic spread, polishing

defects, χ and ϕ offset angles — not only does it constitute good practice but also saves valuable time during the limited shifts available at the CLS.

4.2.1 Determining crystallographic axes: Laue Diffraction

Before performing any mechanical operations like cutting, cleaving, or polishing on the single crystal sample to suit the purpose of the experiment, it is important to know the orientation of the sample (which is grown as a boule). Laue diffraction is an useful technique to determine the orientation of the crystal using hard x-rays by having a large number of diffraction peaks impinged on a photographic film in order to gain information about the crystal symmetry and orientation. For a simple crystal, and a monochromatic x-ray source, only a few diffraction peaks will be visible, since only a single scattering angle will satisfy Bragg's law for each crystal plane. The Laue method uses an Tungsten x-ray source with a wide spread in energy, so as to get more diffraction peaks, that can be analyzed to determine crystal symmetry and orientation. These diffraction Bragg peak positions are recorded using Fujifilm imaging plates, which uses a high-emission, photo-stimulated phosphor, which accurately detects and stores x-ray energy in its phosphor particles. These plates are then scanned without exposing to light and the resulting pattern is analyzed, as shown in Fig. 4.5.

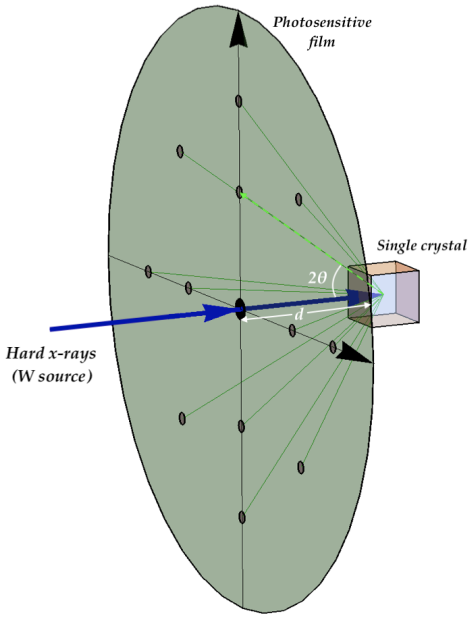

Figure 4.4: Setup for backscattering Laue diffraction geometry for single crystal orientation.

Laue scattering can be operated in transmission or back-scattering geometry. For thick single crystals, Laue back scattering geometry is more suitable as shown in Fig. 4.4, the x-rays produced by the Tungsten target are incident (shown in blue) on a stationary crystal behind the photosensitive plate which then scatters them (shown in green) back towards the x-ray tube. For each crystal plane, in a particular sample orientation, d and θ are fixed, so x-rays with wavelength $n\lambda$ will satisfy Bragg's law and diffract in the direction making an angle 2θ with the incident x-ray beam. The diffracted beams will cross through

the plane perpendicular to the x-ray beam creating a series of Laue spots corresponding to different crystal planes ($d_{hk\ell}$) and the Bragg peaks ($hk\ell$).

Our main subject of investigation in this thesis are La-based cuprates, in Fig. 4.5(a) we see the Laue diffraction pattern by the crystal boule of Nd-LSCO with unknown orientation. We know the space group for our single crystal is $I4/mmm$ and lattice constants are, $a = b = 3.787$ Å, $c = 13.24$ Å. Our aim is to align the single crystal along the [001] crystallographic direction: we begin by a random crystal orientation Fig. 4.5(a), which resembles being close to [100] direction[5] As perform the Laue diffraction again, this time

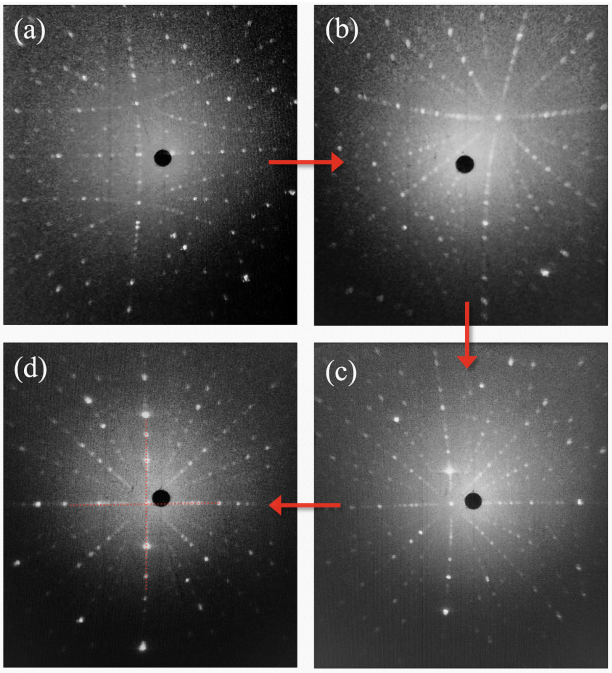

Figure 4.5: Laue scattering images in back-scattering geometry: Aligning a single crystal in a desired crystallographic direction. Images (a) to (d) are Laue scattering photographs from a single crystal alignment procedure. Starting from a random crystal orientation in (a), to polishing and cutting to achieve the crystal oriented along the desired [001]. Details are described in the text.

with one of the adjacent faces of the sample facing the beam (first red arrow operation), and we get (b) which looks close to being oriented [001]. Fig. 4.5(b), however, has offset

[5]We know this by running a Laue simulation of the crystal parameters on OrientExpress software. Since we are not interested in the individual Bragg peaks, I have skipped superimposing the simulated pattern.

in χ, ϕ and θ which can be calculated and corrected to achieve our desired orientation of c perpendicular to the sample surface. We account for these angular (χ, ϕ and θ) corrections (second red arrow) on the goniometer to get to Fig. 4.5(c), then we cut our samples. When the angular offset is less than 5°, I have found it useful to polish on an incline rather than cutting the samples (third red arrow) — after polishing and correcting for a small χ offset we get almost perfect [001] alignment in Fig. 4.5(d). The more accurately this alignment is done, the lesser time we have to invest at the synchrotron[6]. Once we have the correct angles, the next step involves cutting, cleaving, and polishing depending on the nature of the measurement. One thing which is worth mentioning is, even after getting the exact angles it requires extreme caution to precisely cut and polish the crystals along those directions — often in the process of aligning one angle, the other develops an offset. The order in which these corrections are approached make the job slightly easier.

4.2.2 Aligning real and reciprocal axes

Cutting: Wire Saw

After performing the Laue diffraction, the crystal boule on the goniometer is transferred to a wire saw to perform cuts along the desired crystallographic axes. A wire saw is essentially a tungsten[7] (or steel) wire which spools on two discs, running from one to another in such a way that the wire achieves a cutting action by going back and forth over the sample — by dragging a grit of boron carbide across the sample surface — it begins by a shallow scratch but because of the weight on the wire it seeps in until the entire thickness of the samples is cut. Fig. 4.6 shows the wire saw's cutting action, and how the weight can be modulated to achieve accuracy while making the first scratch. The general approach is to achieve one good flat surface and then re-check it with Laue diffraction again until the desired orientation is decent enough, this step can require several iterations. After a flat, well-oriented surface is achieved, we proceed to the next step of cleaving (or polishing-etching) the sample to expose a clean surface which would receive the synchrotron radiation in the scattering chamber at the CLS.

[6]These operation can take days sometimes to get perfect alignment, but I often justify their worth by the ease of aligning the desired peaks at the CLS.

[7]Preferred because of its stiffness but difficult to re-spool.

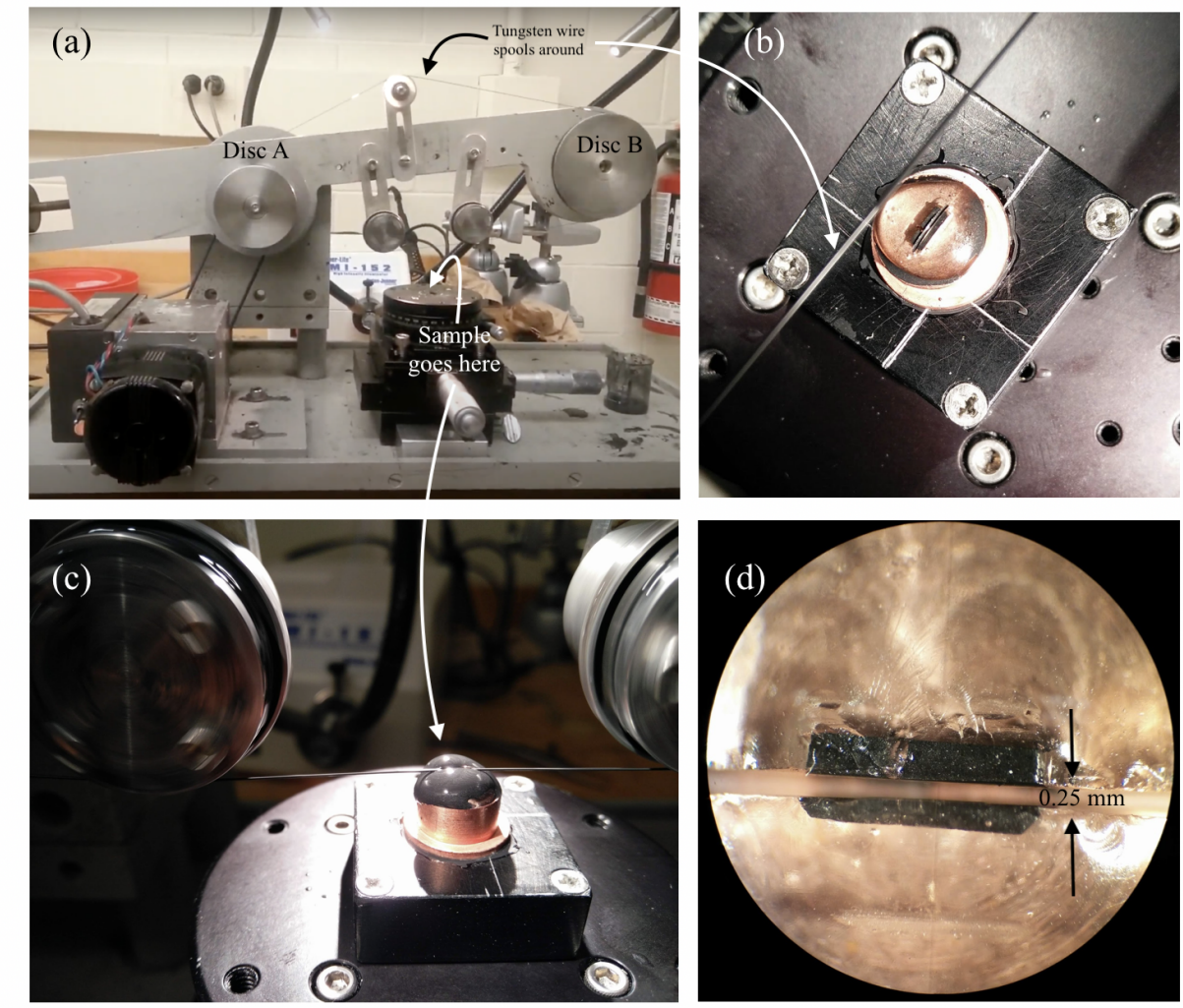

Figure 4.6: Wire saw machine for cutting samples: (a) shows the wire saw assembly, (b) and (c) show the cutting motion by the Tungsten wire in action, and (d) shows the completed task of cutting a single crystal sample along a particular direction. Working and details discussed in the text.

Polishing: to orient and achieve a flat surface

Polishing has to done in multiple stages, with careful transition from a coarser microgrit polishing paper to a fine one. If the aim of polishing is just to correct a small χ offset, or get a flat surface to provide a base of cleaving — one can be slightly careless about it and just use a single 20 micrometer grit paper, since the polished surface would be stuck to the base and not exposed to the synchroton beam. More details discussed in the next polishing section.

Cleaving: Top post and anvil-blade

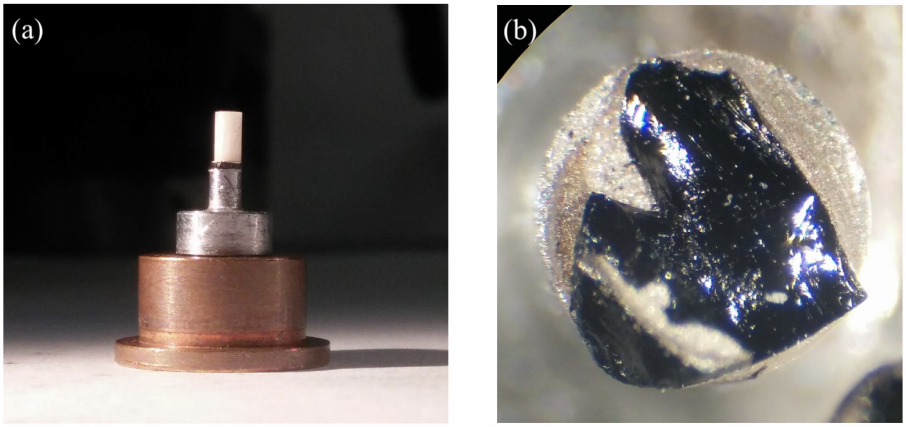

Figure 4.7: Top post cleaving: (a) shows the sample sandwiched between the copper plug and the cleaving post with silver epoxy bonding the sample surfaces, (b) Thee sample is cleaved after a quick, horizontal impulse is imparted on the top post.

A clean surface is crucial for a good (or any[8]) signal intensity. After getting a flat surface, we use a copper plug and a top post attached to the top and bottom ends of the sample as shown in Fig. 4.7(a) — it is generally easier to get a good cleave along the weaker crytallographic axes, in Nd-LSCO it is the c-axis. We use silver epoxy (EPO-TEK H20E) as it has a stronger bond than the interlayer bonding in Nd-LSCO (if applied and cured correctly); thus on giving the top-post a strong flick — the sample is fractured/cleaved

[8]If the surface is not properly cleaved, it is common to not find any peak, or a very feeble peak intensity: both cases are undesirable.

Figure 4.8: Surfaces after sample polishing techniques with a micro grit paper and a granite slab assembly in our lab. Details discussed in the text.

exposing a clean surface. Speculatively, I have found cleaving to become more difficult with increasing hole-doping[9]. There is an additional capability at the load lock at the CLS and the UHV chamber in our lab of using blade and anvil sample cleaver, which applies pressure to the side of the sample causing it to fracture in vacuum, exposing a fresh surface.

Polishing: to prepare a clean surface to be beam-exposed

If the polished surface is to be exposed to the synchroton beam in the RSXS chamber, one needs to exercise caution as the penetration depth of soft x-rays is small (around 100 nm) which means a first few rough layers and contaminants can be a problem. Polishing to prepare a surface is useful in cases when the physical dimension of the crystal has to follow certain restrictions, like before mounting on a uniaxial stress device, the sample has to be of $2 \times 1 \times 0.5$ mm to make sure the applied mechanical stress is not asymmetric. Due to the delicate nature of the sample, all polishing action is done by hand on a custom built assembly which includes a 4 cm diameter Aluminum rod, a granite slab, and a slot to keep the rod's face perpendicular to the slab where we lay the polishing micro-grit paper. The process needs a special water-based solution, which acts as a lubricant as well as a coolant to avoid unnecessary chipping off and fracturing of the sample-face. We begin by positioning the sample with the copper plug at the flat face of an aluminum rod 4.8(a) with the sample surrounded by a Stycast (a glassy substance that ensures the sample does not cracks or chips off once polishing begins). We start off with a coarse 20 μm Aluminum

[9]In one of our tries with Nd-LSCO, the x=0.24 sample took about 10 cleaving attempts to get a good surface, and still the signal intensity was almost non-existent at the CLS.

carbide micro-grit paper, the surface of the sample looks like 4.8(b) once polished with it. We then follow up with finer micro grit papers from 0.3 to 0.05 μm to obtain a surface that looks like 4.8(c). The order in which the grit size is varied is important for imperfections to be minimal, although, the surface looks very smooth and featureless after completing the process and washing with acetone — we still do not get a (001) peak on this surface[10]. There is a very thin layer of contaminants, imperfections and mechanical stresses that dramatically affects the absorption of soft x-rays. The last step is chemical etching to get rid of surface contamination and defects.

Chemical etching

The idea of chemical etching is often used[11] for surface sensitive probes which are highly dependent on penetration depth and first few clean layers. We use Br-etching, where the sample surface is exposed to an alcoholic solution of concentrated Bromine. The rate of etching is important to be controlled, this can be calculated based on the crystal composition, and a solution with a suitable concentration or Br ions and exposure time is obtained — this solution will eat away the first few layers giving us a clean surface, almost comparable[12] to its cleaved counterpart. The eating away is more or less uniform, although, one important factor is the quality of polishing, sharp edges etch faster and might end up producing an overall rough surface. Liquid Bromine is notorious for being corrosive and requires a fuming hood to operate, some friends from the Chemistry Department have been kind enough to help me out with this step. Without them Chapter 6 would not be present in this thesis.

If we do not need the samples to be mounted on a uniaxial stress device, we generally cleave and perform the measurement instead of going through the pain of cutting in special dimensions, polishing upto a certain surface perfection, and using Br-etching to eat away a few bad atomic layers.

[10] This was especially non-trivial, because the Laue diffraction would use hard x-rays and would show a perfect pattern, ignoring surface sensitive details.

[11] Attempts of Br-etching on cuprates go back to late 1980s [59].

[12] We were lucky in many ways than I care to admit: as mentioned in the previous footnote there was no proper soft x-ray experiment that was possible before the main CLS shift. The concentration of Bromine turned out to be perfect for our case and we ended by getting a decent (001) and CDW signal in the polished sample.

4.2.3 Mounting samples: Uniaxial stress device

In general, when mounting samples that would go in the UHV chamber, silver epoxy serves as an excellent candidate as the contact between the sample and the sampleholder. The silver epoxy not only retains good thermal and electrical conductivity at such low temperatures and pressures, but also retains the strength with almost no diffusion of lighter gases (or contaminants) which can be bad for the measurement. For non-strain experiments, the application and removal of silver epoxy is generally straightforward, the removal can be tricky sometimes either via scraping gently with a scalpel or ultrasonic vibrations in an acetone solution. However, the design of the uniaxial stress device sampleholder plate requires the samples to be 2 mm long, 1 mm wide and 0.2 mm thick (see Fig. 4.9) (with c-axis facing out of the plane in our study) — there is a shallow (0.15 mm) valley where the bottom of the sample fits to ensure uniform strain. This makes things slightly tricky as we need to set a very thin flat layer of epoxy, then the sample rests on top of that, and finally the two ends of the sample are covered in epoxy, this makes the stress align along one direction, and cancel stray off-uniaxial stresses. I have found it almost impossible to reuse a sample after the experiment is performed, either the sample is cracked or the epoxy removal leads to breaking of the sample. Mounting samples and the role of epoxy will be discussed in detail in Chapter 6.

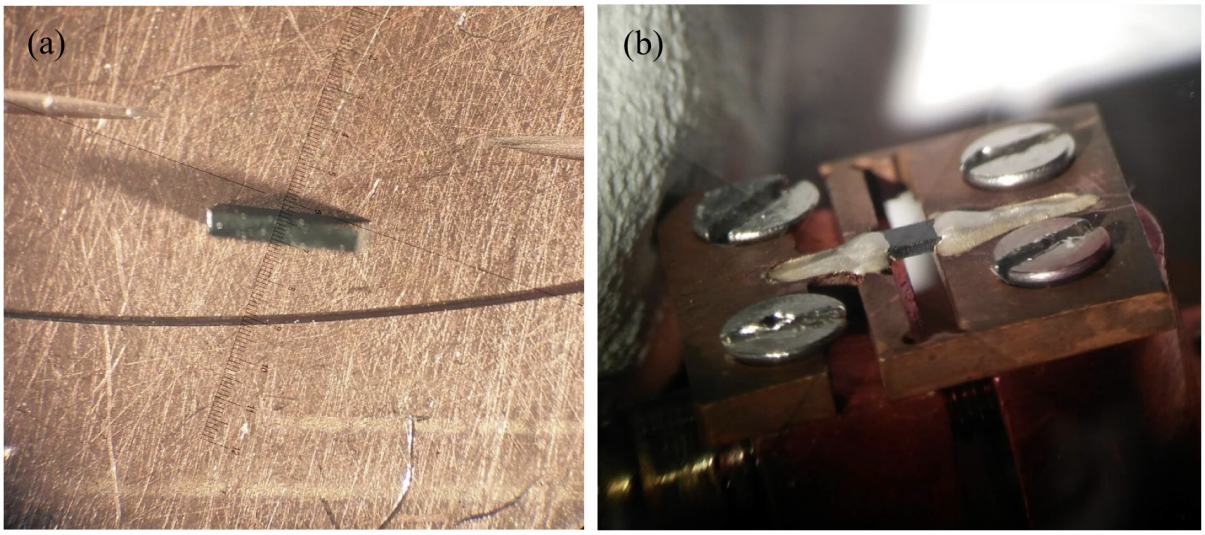

Figure 4.9: Finished product: Nd-LSCO samples 2 mm long, 1 mm wide and 0.2 mm thick. (a) Polished and etched, (b) mounted on the uniaxial stress device sampleholder plate. (a) shows a strand of author's hair to give a sense of scale.

Chapter 5

Evolution of electronic nematic order with hole doping in Lanthanum based cuprate superconductors

5.1 Introduction

There is a growing realization that the essential physics of many quantum materials, such as high-temperature superconductors, involves a complex interplay between many different electronic phases like charge density wave order, pair density wave order, magnetism, orbital order, electronic nematicity that have very similar energy and temperature scales [9, 8]. In the last two decades, theoretical proposals for electronic liquid-crystal phases [60, 7, 61, 62], specifically, existence of a nematic phase have been experimentally realized in cuprates [12, 13, 14, 15, 17, 16] and iron-based superconductors [63, 64]. An electronic nematic phase occurs when the electronic structure breaks the rotational (point group) symmetry but leaves the translational (lattice group) symmetry intact. A key example of the importance of intertwined order is the cuprate high temperature superconductors. Previous work by our research group has identified the existence of electronic nematicity and its relationship to charge density wave order in the cuprate $(\mathrm{La,M})_2\mathrm{CuO}_4$ (M is Sr, Ba, Eu, or Nd) by measuring the (001) Bragg peak using resonant x-ray scattering [18]. We investigated the $\mathrm{C}_4 \rightarrow \mathrm{C}_2$ rotational symmetry-breaking (electronic nematicity) of the average, intra–unit cell, electronic structure within an individual CuO_2 plane. The role of electronic nematicity, such as whether it is a feature of the pseudogap region and how it relates to CDW order or hole doping or the crystal structure of different cuprate families

has not yet been fully established.

In this chapter, we begin by reviewing existing consensus on electronic nematic phases in strongly correlated electronic systems, particularly, highlighting the case of Lanthanum based cuprates that allow us to investigate the orbital asymmetry owing to a fortuitous access to the forbidden (001) peak on-resonance [65, 66] using resonant x-ray scattering. We, then, establish a temperature based anisotropy by noting the difference between copper-oxide and non-copper-oxide planes (also called spacer layer) through investigating the in-plane copper atoms and apical oxygen atoms. After establishing the probe and what we define as 'electronic nematic', we perform measurements at different hole dopings in $La_{1.6-x}Nd_{0.4}Sr_xCuO_4$ (Nd-LSCO) to understand the doping evolution of this novel phase.

5.2 Electronic nematic phase

5.2.1 Electronic liquid crystal phases and possible origins

As described in section 2.3.3, electronic nematicity refers to a breaking of rotational symmetry of the electronic structure in a manner that is not a straightforward result of crystalline symmetry, such that an additional electronic nematic order parameter, distinct from the structure would be required to describe the resulting phase. Such a state can be difficult to identify in materials that have orthorhombic structures, which would naturally couple to any electronic nematic order and vice versa. Moreover, the manifestation of nematic order may depend on the details of the crystal structures of the materials, such as whether the structure is tetragonal or orthorhombic.

There have been a few suggestions to realize the mechanism for the formation of a nematic phase. One way would be through thermal or doping-induced (partial) melting of a stripe (smectic) phase such that it regains translation symmetry[1] but still has orientational ordering — a proposed vestigial nematic state [67, 68]. For instance, in cuprate superconductors existence of CDW order is well-established at 1/8th doping where periodic superstructure of charge modulation break both translation and rotational symmetry. Increasing temperature or hole-doping in such a system might allow breaking long-range order and fashion itself into local stripe order that gathers a statistically preferred direction — an average rotational symmtery breaking of sorts — while keeping the translational invariance intact.

[1] Or maybe it does so before orientational disordering eventually becoming a Fermi liquid?

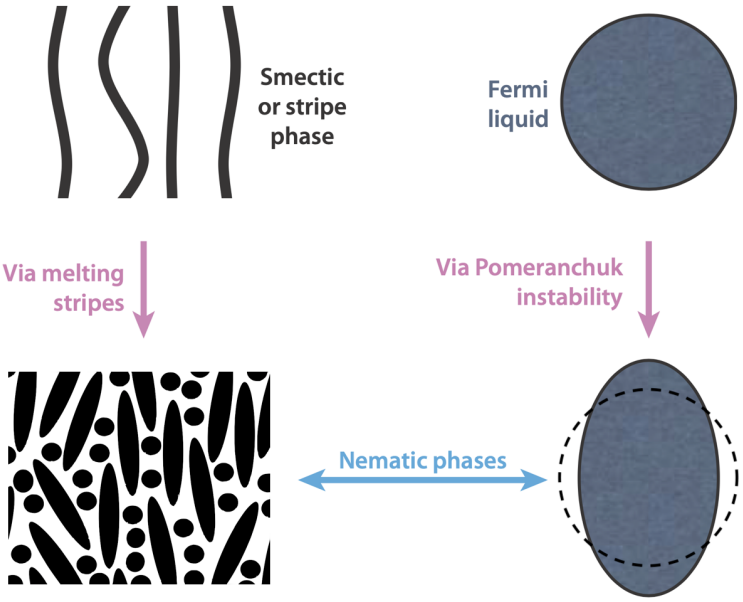

Figure 5.1: Two possible mechanisms for the existence of a nematic phase: via thermal (or quantum) melting of a stripe phase such that it regains translational invariance with an average rotational symmetry breaking; and through the elliptical distortion of the Fermi surface — caused by hole doping or temperature or possibly quantum effects — of a metallic circular Fermi surface via a Pomeranchuk instability. Figure from [61] with permission.

Alternatively, the second approach starts from the momentum space structure of a metallic system, a Fermi liquid type approach. This phenomenological approach proceeds by considering fermions having a well-defined Fermi surface and quasiparticles. The idea comes from Pomeranchuck [69] who showed that the if some of the Landau parameters for a Fermi liquid are negative and large enough to overcome the stabilizing effects of Fermi pressure, then a thermodynamic (Pomeranchuk) instability occurs, causing the system to spontaneously lower their symmetry. For instance, as shown in Fig 5.1 for a simple 2D circular Fermi surface, a Pomeranchuk instability will cause an elliptical distortion causing the momentum structure to transition down into a residual C_2 rotational symmetry and show anisotropic electronic/orbital signatures with a concomitant local average orientation.

5.2.2 Electronic nematic phase in cuprate superconductors

For cuprates superconductors, first reports of an electronic nematic phase include measurements of anomalous anisotropy in the in-plane resistivity in YBCO[2] and LSCO[3] by Ando *et al*. [12] in 2002. Despite the already known weak orthorhombic nature of the unit cells in YBCO the thermal dependency of the in-plane anisotropy could not be entirely described by the structural transitions, leading to the proposition of an electronic nematic phase in YBCO, which was subsequently confirmed by neutron scattering experiments and later by Nernst effect. Experimental evidences of electronic nematicity that is distinct from structural distortions now include reports from bulk transport [12, 14, 13], scanning tunneling microscopy (STM) measurements [16, 15], and inelastic neutron experiments [17]. Achkar *et al*. demonstrated that the resonant x-ray scattering measurements of the (001) Bragg peak provide sensitivity to electronic nematicity [18].

Recently, reports have emerged of nematic fluctuations in the vicinity of the quantum critical point (QCP) in another cuprate material Bi2212[4] using elasto-resistance measurements [44] and enhanced electronic nematic fluctuations using Raman scattering [45], suggesting a link between electronic nematicity and the QCP. To examine the possibility that electronic nematic order is associated with the QCP and electronic structure changes in the cuprate family $La_{1.6-x}Nd_{0.4}Sr_xCuO_4$ (Nd-LSCO), we probe electronic nematic order — by measuring the orbital asymmetry via the (001) Bragg peak — using resonant x-ray scattering as a function of hole doping, x. Investigation of Nd-LSCO provides an opportunity to study the evolution of nematicity over a wide range of doping — furthermore in the same material system, some of the most compelling signatures of quantum criticality and electronic structure evolution have been recently observed, such as the divergence in the heat capacity [36] and a change in the electronic structure from angle-dependent magnetoresistance (ADMR) measurements [39] at hole doping in the vicinity of x = 0.23 — enabling a direct comparison of these previous results to our measurements in electronic nematicity.

[2] $YBa_2Cu_3O_y$
[3] $La_{2-x}Sr_xCuO_4$
[4] $Bi_2Sr_2CaCu_2O_{8+x}$

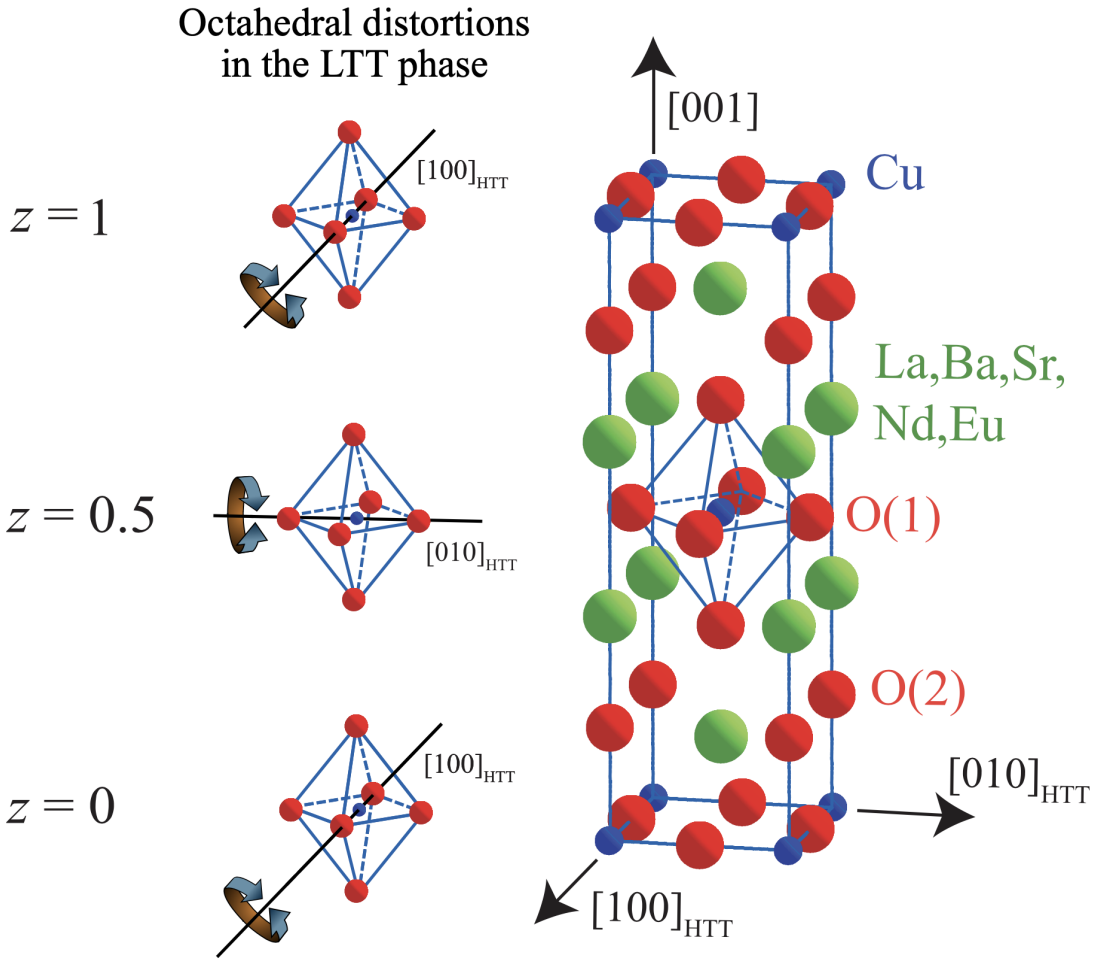

Figure 5.2: Crystal structure of Nd-LSCO: Unit cell of Nd-LSCO (or the La214 unit cell) in the high-temperature tetragonal phase (HTT). O(1) and O(2) are in-plane and apical oxygen sites, respectively. The low-temperature tetragonal (LTT) phase is understood in terms of rotations of the CuO_6 octahedra about axes parallel to the Cu-O bonds, with the rotation axis of the octahedra alternating between the a and b axes of neighboring planes ($z = 0$ and $z = 0.5$). This induces C_4 symmetry-breaking of the average (or intra- unit cell) electronic structure within an individual CuO_2 plane, referred to here as electronic nematicity.

5.3 Probing electronic nematic order using resonant x-ray scattering

5.3.1 On-resonance (001) Bragg peak

Understanding how the measurement of the (001) Bragg peak reveals electronic nematicity requires examination of the crystal structure of La214s. As described in section 2.3.2, Nd-LSCO exhibits a structural phase transition from the low temperature orthorhombic (LTO) to low temperature tetragonal phase (LTT) at temperatures between 50 – 90 K depending on doping. The LTT phase is characterized by tilting of the CuO_6 octahedra along the a or b axes such that each individual CuO_2 layer structurally breaks C_4 rotational symmetry as shown in Fig. 5.2. The axis of rotation of the octahedra, however, rotates by 90 degrees between neighbouring layers producing a crystal structure that is globally tetragonal, despite having orthorhombic layers. Consequently, any probe that bulk averages the layers would yield the same result along the a and b axes and not reveal nematic order.

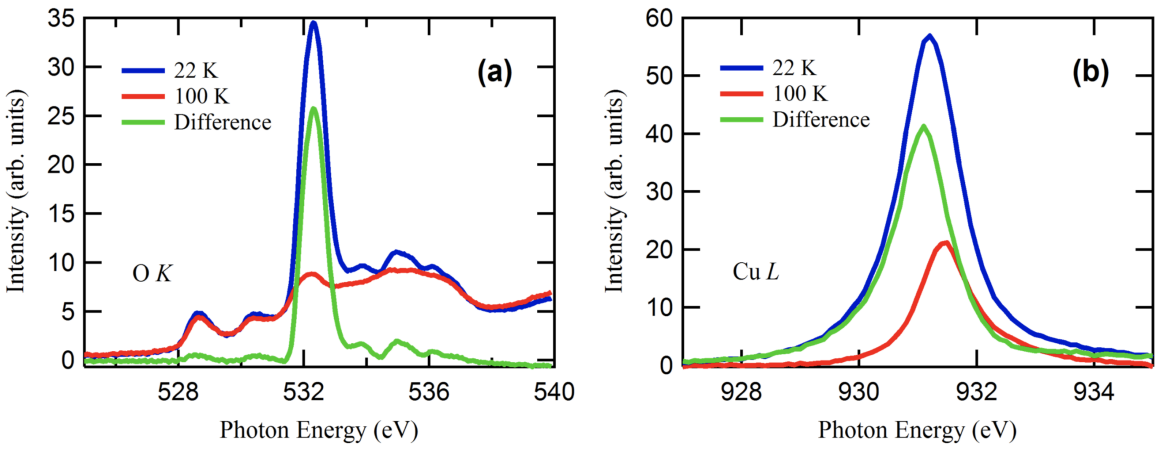

Figure 5.3: Energy dependence of the (001) peak at the O K (a) and Cu L (b) edges in x = 0.125 LBCO. Background intensity has been removed from all spectra with a constant offset for clarity. Figure adapted from [70] with permission.

Resonant x-ray scattering of the (001) Bragg peak, however, provides a direct measure of the difference in the symmetry of the electronic structure between neighbouring layers [18].

Off resonance or with conventional x-ray diffraction, the (001) Bragg peak is forbidden, based on the ionic positions of atoms in the LTT or LTO phases. However, resonant x-ray scattering is sensitive to orbital symmetry as established in section 3.3.3, which differs for atoms in neighbouring layers in the LTT phase. Moreover, by tuning the photon energy to correspond to different atoms within the unit cell, the electronic symmetry breaking of the CuO_2 planes – which contain the Cu d and O p states that cross Fermi energy E_F and are most relevant to the low energy physics of the cuprates – can be differentiated from the La_2O_2 spacer layer, which do not have states that cross E_F but would be sensitive to changes to their orbital symmetry induced purely by structural distortions. In Fig. 5.3 we show how the (001) peak responds to change in temperature and resonance energy for LBCO.

Achkar *et al.* showed that the temperature dependence of the (001) peak intensity exhibited a dichotomy when the photon energy is tuned to different atoms in the neighboring layers of the Nd-LSCO unit cell [18]. As we see in Fig. 5.4, an abrupt 1st order increase at the LTO $\rightarrow$ LTT transition consistent with previous measurements of the structural transition was observed when the photon energy is at the La M edge ($\sim$826 eV) or an energy associated with apical oxygen ($\sim$533.5 eV) – atoms in the La_2O_2 spacer layer. However, a more gradual temperature dependence is observed when the photon energy is tuned to the Cu L edge ($\sim$931.5 eV) or an energy associated with in-plane O ($\sim$528.5 eV) – atoms in the CuO_2 planes. The different temperature dependences can be understood in terms of an electronic nematic order in the CuO_2 planes that has a temperature dependent susceptibility and provides a contribution to the (001) peak intensity in addition to any contributions induced by the lattice potential. Effectively this is akin to an internal strain applied to individual spacer layer by the lattice distortion, with the electronic structure of the CuO_2 planes (probed by the (001) peak intensity at the Cu L edge exhibiting a response that depends on the electronic nematic susceptibility. Importantly, Achkar *et al.* also showed that this electronic nematic order is coupled to but distinct from charge density wave order.

To characterize the measure of in-plane anisotropy, we begin by writing out the structure factor using Cu atoms — it is convenient as their ionic position do not change during the LTT $\rightarrow$ LTO structural phase transition — in the La214 unit cell for the (001) peak, as:

$$S(001)_{\mathrm{Cu}} = \boldsymbol{\varepsilon}_{\boldsymbol{f}}^{*} \left(F_{\mathrm{av}}(z=0) + e^{i\pi} F_{\mathrm{av}}(z=0.5) \right) \boldsymbol{\varepsilon}_{\boldsymbol{i}}, \tag{5.1}$$

where $\boldsymbol{\varepsilon_i}$ (and $\boldsymbol{\varepsilon_f}$) denote incident (and scattered) photon polarization, and F_{av} is a tensor representation of the average atomic scattering form factor for Cu in neighbouring planes

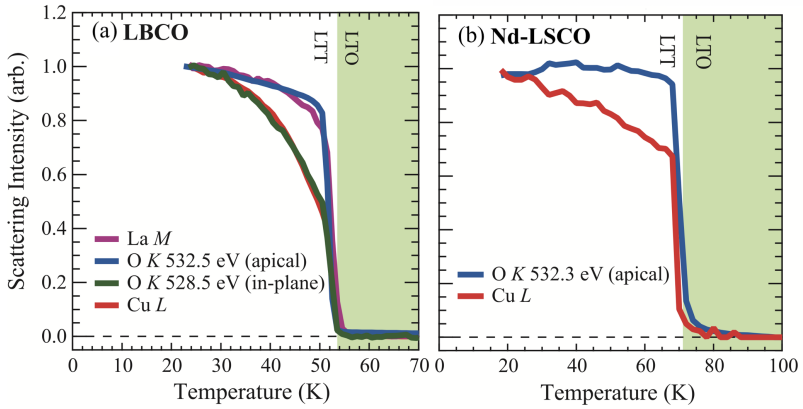

Figure 5.4: Temperature dependence of the (001) Bragg peak intensity: The intensities are normalized by the corresponding low-temperature values, $I_{(001)}(T)/I_{(001)}(20\text{ K})$ with photon energy tuned to the spacer layer atoms, or La M, apical O K, and copper-oxide layer atoms in-plane O K, Cu L edges for LBCO and Nd-LSCO. Figure reproduced from [18] with permission.

$z = 0$ and $z = 0.5$, as

$$F_{\text{av}}(z) = \begin{bmatrix} f_{aa,\text{av}}(z) & 0 & 0 \\ 0 & f_{bb,\text{av}}(z) & 0 \\ 0 & 0 & f_{cc,\text{av}} \end{bmatrix}. \tag{5.2}$$

It is worthwhile to note that for conventional (non-resonant) scattering, both $F_{\text{av}}(z = 0)$ and $F_{\text{av}}(z = 0.5)$ have identical terms, which makes the (001) intensity go to zero. Furthermore, on-resonance the diagonal components of the average atomic scattering form factor — determined by local intra-unit cell anisotropic interaction — follow symmetry of the rotation between layers as

$$f_{cc,\text{av}}(z = 0) = f_{cc,\text{av}}(z = 0.5), \tag{5.3}$$
$$f_{bb,\text{av}}(z = 0) = f_{aa,\text{av}}(z = 0.5), \text{and} \tag{5.4}$$
$$f_{aa,\text{av}}(z = 0) = f_{bb,\text{av}}(z = 0.5). \tag{5.5}$$

We define the measure of in-plane anisotropy for the Cu $3d$ orbital in $z = 0$ and $z = 0.5$ layers as

$$\eta = f_{aa,\text{av}}(z) - f_{bb,\text{av}}(z), \tag{5.6}$$

which from symmetry conditions is identical to

$$\eta = f_{aa,\mathrm{av}}(z=0) - f_{aa,\mathrm{av}}(z=0.5). \tag{5.7}$$

The scattering intensity for the (001) at Cu L edge from Eqn. (5.1) can be written as:

$$I(001) \propto |S(001)|^2 = \left| \boldsymbol{\varepsilon}_{\boldsymbol{f}}^{*} \begin{bmatrix} \eta & 0 & 0 \\ 0 & -\eta & 0 \\ 0 & 0 & 0 \end{bmatrix} \boldsymbol{\varepsilon}_{\boldsymbol{i}} \right|^2 . \tag{5.8}$$

5.3.2 Azimuthal dependency

As shown in the supplementary material of Ref. [18], the expression for (001) peak scattering intensity in Eqn. (5.8) can be experimentally validated to hold for an electronic rotational symmetry breaking signature by measuring its azimuthal dependence relative to the incident polarization — scattering geometry shown in Fig. 5.5 (b). The azimuthal dependence of I_π/I_σ providing strong confirmation that the (001) peak at Cu L edge is measuring electronic nematicity of the Cu $3d$ states and has a form given by Eqn. (5.8).

Other ordering and charge modulations signatures would have a different azimuthal dependency. Fig. 5.5 shows how modulations between planes of the average charge or lattice position or antiferromagnetic ordering of the average c-axis component of the Cu magnetic moment would behave differently from electronic nematicity.

5.4 Experimental procedure

5.4.1 Experimental setup

The results discussed further are performed over Nd-LSCO samples at hole doping levels of x = 0.125, 0.17, 0.18, 0.19, and 0.24 at the in-vacuum four-circle diffractometer at CLS's REIXS endstation. These samples were provided by collaborators and grown using travelling solvent floating zone (TSFZ) method. We[5] measured the (001) peak and charge density wave (CDW) order at different temperatures — varying in the steps of 2 to 3 K — for these doping levels.

[5]These measurements are performed over a course of last 2-3 years by previous and current members of our research group, including myself. I measured the x = 0.24 sample.

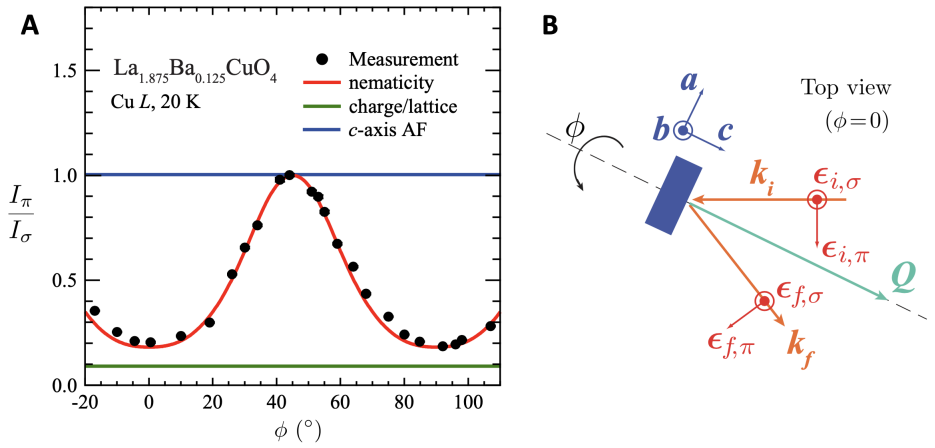

Figure 5.5: (a) Azimuthal dependence of the (001) Bragg peak intensity: The azimuthal dependence of I_π/I_σ provides strong confirmation that the (001) peak at Cu is measuring electronic nematicity and not charge ordering or antiferromagnetic order, which would behave differently following from the symmetry of the scattering tensor. (b) Scattering geometry for the azimuthal dependent measurement described in the text. Figure taken from the Supplementary material of [18] with permission.

For this scheme of doping series measurement, we need a cleaved surface to get a decent surface and good signal intensity, this is achieved by preparing the sample before the beamtime at the synchrotron. The samples are characterized via Laue diffraction which helps in marking a/b axes for easier alignment as well as looking for twinning and other imperfections. In order to expose a fresh surface, samples are cleaved beforehand in our lab and then kept in an clean and dry environment until the experiment. The cleaved samples are mounted on a copper plug with silver epoxy — which is a good conductor and retains strength at low temperatures and ultrahigh vacuums — such that the cleaved ab-face is parallel to the sampleholder surface and at $\theta = 0$ geometry c-axis and the incident photon beam are collinear. Once mounted on the sampleholder, the assembly goes in the load lock chamber until it is brought down to near-UHV pressures, only them the valve to the main scattering chamber is opened and the sample is inserted in the sample receptacle slot into the four-circle diffractometer-gonimoter's center of rotation. The position is screwed in place using an externally controlled in-situ screwdriver arm to avoid any undesired displacements.

The first step is the coarse alignment by eye using the cross hairs on the telescope

which are very carefully aligned to the beamspot line-of-sight. Once we locate the a good spot on the sample under investigation, we start with fine tuned calibration using x-ray absorption spectroscopy (XAS) measurements at Cu L edge for instance[6]. After locating a decent spot of the sample, we proceed to align the crystallographic axes using the structural Bragg peaks — at low temperatures for Nd-LSCO, which is a tetragonal structure, we can access (004), (103), and (-103) Bragg peaks — at an incident photon energy of 2200 eV. We use the MCP detector to visually center the Bragg peaks and record the respective motor values which are then used to set the orientation matrices in the SPEC macros, allowing up to access the reciprocal space by desired Miller indices.The lattice parameters for Nd-LSCO samples were taken to be $a = b = 3.787$ Å and $c = 13.24$ Å for finding and recording Bragg peak positions.

Once the sample is aligned, we move to the Cu L and apical O K edge to locate and confirm the (001) Bragg peak. Validation generally includes measuring the peak at low temperature and then warming up the sample and comparing the (001) peak intensity which should dramatically drop down after 60-90 K for different doping levels as it is only permitted in the LTT phase. We, then, perform a series of ℓ-scan[7] measurements around (001) peak at different temperature values. The measured peaks shapes are then fitted to a Lorentzian function to get information about peak intensity, peak area, full-width half-maxima (FWHM), and the peak position in ℓ.

5.4.2 Data collection and analysis

The data collection process involves not only careful calibration of the motor positions, incident photon energy, and count time but also validating any drifts caused by variety of beamline's operation parameters. There are changes which can be mitigated like described in Section 4.1.2, the assembly is designed in a way to reduce the change with temperature mostly to z and θ degree of freedom, which makes it slightly easier for us to confirm if the incident beam is hitting the same 'good' spot on the sample.

Although, it depends on the detector how the exact steps for data analysis are proceeded, however, a general scheme is as follows:

[6]Technically, this can work with tuning the energy to any of the transition edges of any of the atoms in the unit cell, often the O K edge signal has a higher flux and disturbance from the oxygen content in the epoxy. Hence, copper edge is preferred.

[7]This is achieved by performing a $\theta - 2\theta$ scan in which both the sample and detector rotate at the same rate, such that the ratio of the two remains constant.

- **Pre-fitting procedures:** Normalizing the scattered signal with the intensity of the incident beam — to make sure fluctuations in any physical parameters at the beamline or the storage ring is accounted for — thus providing a common ground to compare signal intensity with changes in temperature, reciprocal axes, and other degrees of freedom.

- **Higher harmonic correction:** Before moving to background subtraction, it is important to check any potential signal contribution from second-order light, unfortunately, the latter often causes a difficulty in recording the (001) peak intensity at the apical O K edge. Higher harmonics are produced in the undulator and is difficult to be contained or filtered by the monochromator which only allow light of only certain wavelength to pass through. Thus, an on-resonance geometry that allows the forbidden (001) peak also permits the structural (002) Bragg peak at *almost* the same (2θ) detector position. Ways to correct this include, switching to an energy resolved detector, or moving slightly towards the shoulder of the (001) peak — which is broader in reciprocal space than the (002) peak — thus away from the (002) Bragg peak geometry, the intensity at the shoulder/falling edge responds approximately proportional to the actual peak intensity and can be carefully validated by fitting Lorentizans and comparing full-width half-maxima (FWHM). Other ways can include subtracting the signal at higher temperature devoid of (001) peak. Note that the energy resolved detector (SDD) was used for the x = 0.24 measurements, as shown in Fig. 5.6.

- **Background subtraction:** We generally fit a third order polynomial (or fifth in some cases) with the signal intensity/detector count at detector positions sufficiently away from the peak shape under investigation. it is hard to predict exactly how many points would be used to fit the background polynomial — which is done visually — but ideally the background polynomial fit should not change by varying the degree of polynomial[8] or a few points up and down. Especially for the (001) peak, sometimes it is also good to validate the background subtracted signal with the high temperature signal subtraction — as in the LTO phase there is (002) peak but no (001) signal — to make sure any saturation effects in the detector used. Irregularities can also be detected once we start fitting a Lorentzian line shape — by looking at residual (= fitted data - actual data) shapes — in terms of large error in FWHM or offsets at few temperatures.

[8] We generally use cubic fits, I have tried changing the degree of polynomial between 3 to 6 for the (001) peak and a good background fit does not respond much to it.

- **Lineshape fitting:** Post-background subtraction, the Bragg peaks we measure are mostly Lorentzian line shapes[9], however, sometimes there is some Gaussian contribution — say from the instrument/detectors count efficiency — those can be corrected by validating the fitting Pseudo-Voigt (PV) functions.[10] After subtracting the polynomial background, we fit to:

$$L(x) = c_0 + \frac{A}{1 + 4\left(\frac{x-x_0}{w}\right)^2} \tag{5.9}$$

where, A is the amplitude, w is the FWHM, c_0 is a constant offset[11]. A PV function would look like:

$$P(x) = c_0 + c_1 \cdot x + \alpha \cdot \overbrace{\left(\frac{A}{1 + 4\left(\frac{x-x_0}{w}\right)^2}\right)}^{\text{Lorentzian}} + (1-\alpha) \cdot \overbrace{\left(\frac{Ae^{-4\log[2]\cdot\left(\frac{x-x_0}{w}\right)^2}}{w \cdot \sqrt{\frac{\pi}{4\log[2]}}}\right)}^{\text{Gaussian}} \tag{5.10}$$

α lies between 0 and 1, former extreme means Gaussian and latter being the Lorentzian. c_1 is the possible linear contibution, other variables are same as that of Eqn. 5.9[12].

Once the fitting schedule is satisfactorily completed, we can extract the fitting parameters — and after checking different fitting schemes and plotting error bars with the best fit parameters – we proceed to plot them trying to understand the underlying physics.

5.4.3 Results for x = 0.24 Nd-LSCO

We show the above-mentioned data collection and analysis scheme for Sr hole doping of x = 0.24 in Nd-LSCO or $La_{1.6-x}Nd_{0.4}Sr_xCuO_4$ in Fig. 5.6

[9] This has also been rigorously investigated previously by our group as a function of energy and detector positions and temperature.

[10] PV are a linear combination of a Gaussian (G) and a Lorentizan (L) line shape, one can record the individual G and L contribution by fitting to a α·G + (1-α)·L type function, where α is a number between 0 and 1.

[11] Which can be modified to make the Lorentzian signal go to zero if the actual signal is zero at extreme ends from the peak.

[12] I find CDW peaks (like the one shown in section 2.3.1 and section 5.5.2) to fit in well with pseudo-voigts which I think is due to its ability to provide a Gaussian and a polynomial background subtraction at the same time.

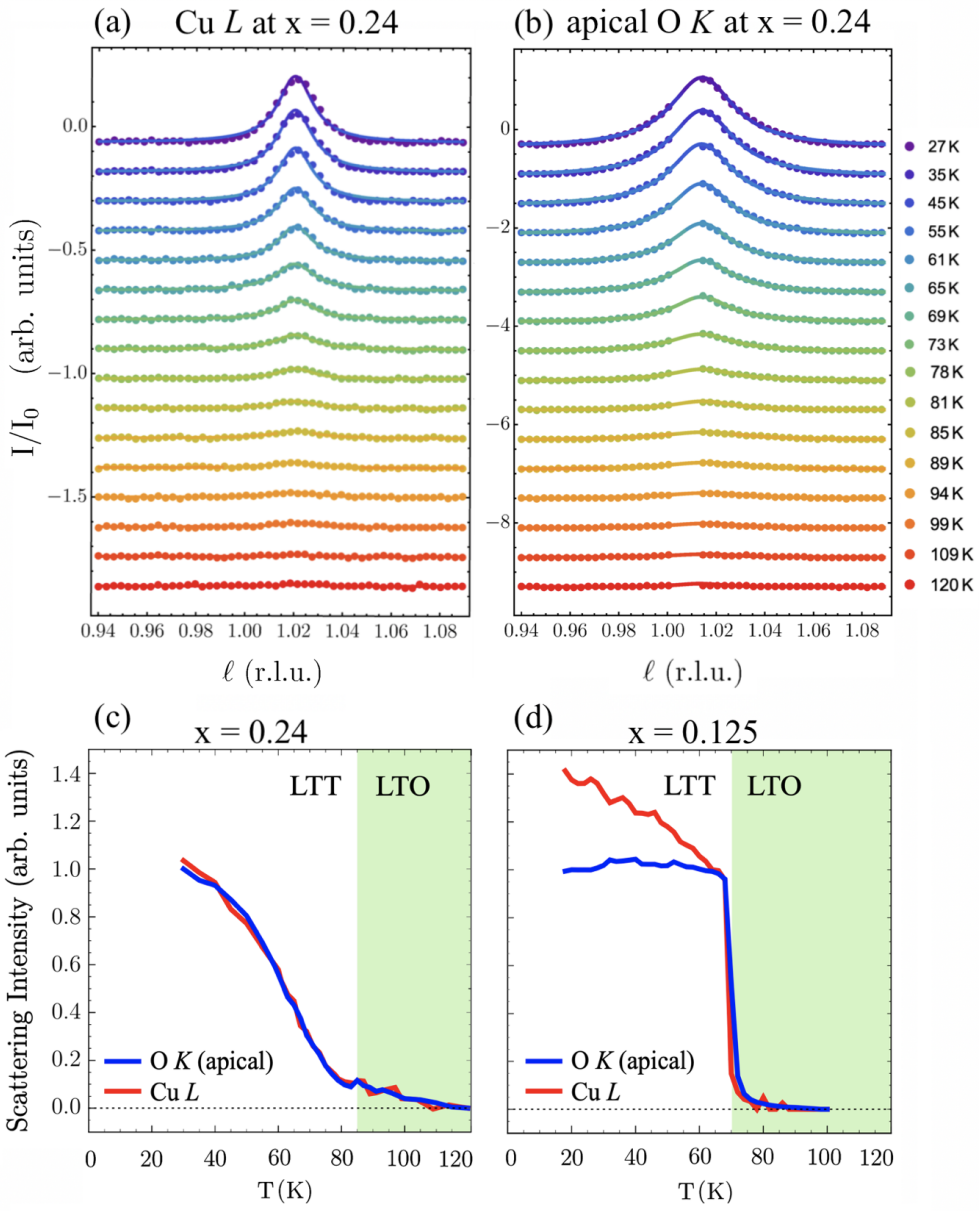

Figure 5.6: Temperature dependence of the (001) Bragg peak intensity in Nd-LSCO x = 0.24: Recorded and background subtracted (001) peak. Colored dots denote recorded data at different temperatures and lines imply the Lorentzian fits for (a) apical O K edge and (b) in-plane Cu L edge, (c) shows the peak intensity obtained by fit's amplitude, and (d) is data adapted from Ref. [18] to highlight the loss of orbital asymmetry from hole doping, x = 0.125 to 0.24, as one crosses the putative QCP. The green region shows the onset of the LTO phase in the samples.

5.5 Results and discussion

5.5.1 Evolution of electronic nematic order with hole doping

We investigate electronic nematic order in Nd-LSCO as a function of doping from x = 0.125 to x = 0.24, crossing the putative QCP (at x ∼ 0.23) in the measurement set.

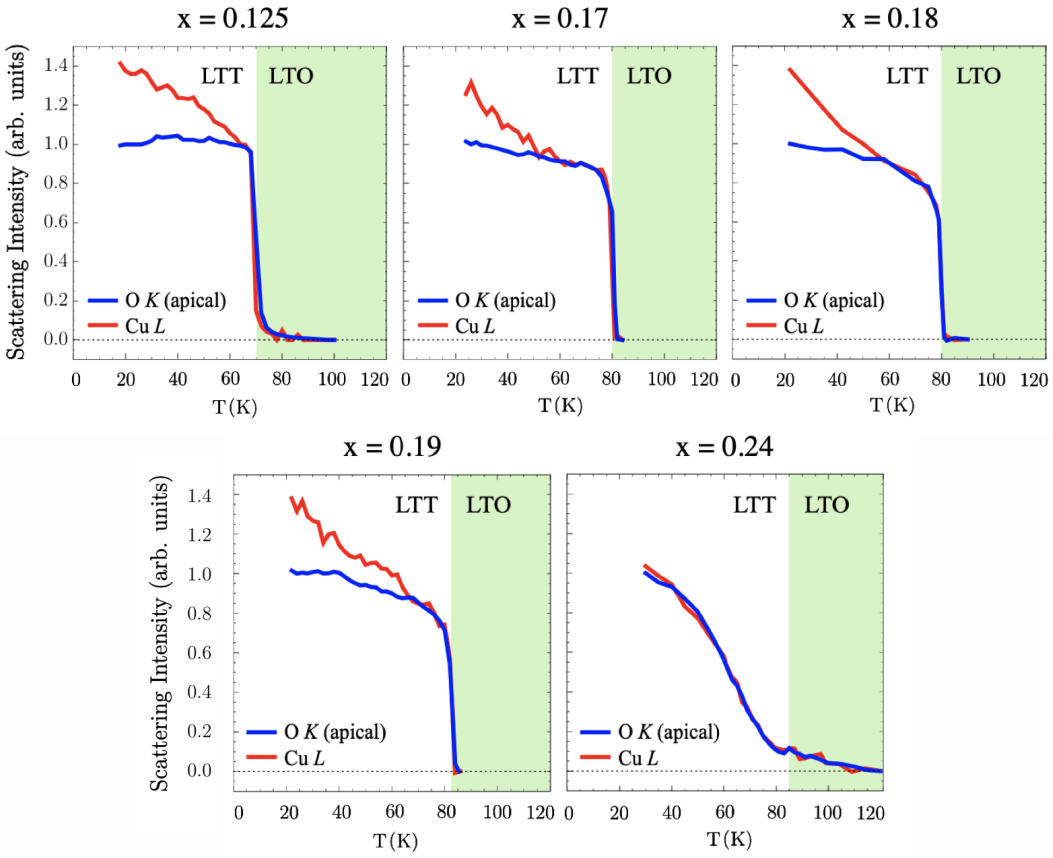

Figure 5.7: Doping and temperature evolution of the (001) Bragg peak intensity in Nd-LSCO. The intensities for the apical O K are normalized by the corresponding low-temperature values, $I_{O(001)} \sim 24$ K, with photon energy tuned to the apical O K and Cu L edges for $La_{1.6-x}Nd_{0.4}Sr_xCuO_4$ with Sr content: x = 0.125, 0.17, 0.18, 0.19 and 0.24. The white and green region indicate the LTT phase and the LTO phase respectively. The data for x = 0.125 is adapted from Ref. [18] and for x = 0.18 from Ref. [70] with permission.

In Fig. 5.7 we show the intensity of the (001) peak as a function of temperature at

an energy sensitive to Cu L edge (probing the CuO_2 planes) and the apical O K edge (probing the La_2O_2 layer). Note, here the data at the different edges is arbitrarily scaled to match in intensity below the LTO $\rightarrow$ LTT phase transition to highlight the difference in temperature dependence for different doping levels. In Fig. 5.7(a), data from our group's previous work [18] is reproduced, which showed that at x = 0.125, a distinct difference exists in the temperature dependence of the (001) peak for measurements at the Cu L and O K edges. As the doping is increased in Nd-LSCO, a similar difference in the peak intensity between Cu L and O K edges is observed for x = 0.125, 0.17, 0.18 and 0.19. However, for x = 0.24 within the measurement accuracy we detect no difference in the T dependence of the (001) peak when measured at the apical O K and Cu L edges.

Our principle conclusion from this result is that static, long range ordered electronic nematicity vanishes upon crossing the putative QCP at x = 0.23[13] in Nd-LSCO, indicating that electronic nematicity may be tied to the quantum criticality and electronic structure changes in overdoped cuprates. Similar evidence for vanishing electronic nematic order in the vicinity of the putative QCP — at the end of the pseudogap phase — at x = 0.23 that has been identified in Nd-LSCO and other cuprates. This suggests that nematicity may be the fluctuating order responsible for the quantum critical phenomena at this point. The possible connection of electronic nematicity with the putative QCP at x $\sim$ 0.23 is reinforced by recent measurements in other cuprates families that do not exhibit the LTT structural phase, indicating that an electronic nematic phase terminating at the QCP in overdoped cuprates may be a generic property of the cuprate phase diagram. Recent elasto-resistance [44] and Raman scattering [45] measurements in Bi2212 have both shown dynamical electronic nematic fluctuations that are enhanced – in the overdoped region between $p = 0.20$ and 0.23 – and nematic quantum criticality which is consistent with the putative quantum critical point for Bi2212 at $p^* \sim 0.22$ [45].

It has also been established that the electronic structure of the cuprates undergoes a transformation[14] from a small Fermi surface or Fermi arcs in the pseudogap phase to a large hole like Fermi surface at higher doping above what has been identified as the QCP, in the La214 cuprates [39, 71, 72], and other cuprate families [38]. The vanishing of electronic nematicity may be associated with this change in the nature of the Fermi surface. However, with evidence of electronic nematicity existing across the entire psuedogap phase, it would seem likely that the pseudogap might have a nematic character.

[13] As reported in Ref. [38, 36].

[14] Other techniques like angle-resolved photoemission spectroscopy (ARPES) [71, 72] and more recently angle-dependent magnetoresistance (ADMR) [39] have observed transformation of the Fermi surface structure at the pseudogap critical point (x $\sim$ 0.23) in La-based cuprates; which might have implications for the rotational symmetry-breaking of the electronic structure through a nematic QCP in the La214 family.

5.5.2 Evolution of CDW order with hole doping

Trying to understand the relation between the three symmetry-breaking phases — namely, CDW, nematicity, and structural distortions — is one of the key challenges in this family. In order to gain more insight about these intertwined symmetry-breaking phases, we also recorded the CDW signal at different doping levels in Nd-LSCO. Speculations arise on whether CDW, nematicity, and structural distortions compete, cooperate, or leads to onset of each other? There have been attempts to tackle each phase separately by suppressing the others using uniaxial strain, magnetic fields, doping and hydrostatic pressure [31].

As introduced in section 2.3.1 the existence of stripe-like CDW order, that breaks both translational and rotational symmetry, does not appear to be the solely responsible for the electronic nematicity, which is rather a distinct phase that persists to higher doping than the CDW order. A schematic updated phase diagram that summarizes the doping evolution of LTO $\rightarrow$ LTT phase transition, the onset of CDW order and our evidence for electronic nematicity is depicted in Fig. 5.9. While the onset of CDW order coincides with the LTO $\rightarrow$ LTT transition in Nd-LSCO at x = 0.125 no signature of CDW is observed in Nd-LSCO x = 0.18 or 0.19, despite clear observations of electronic nematicity. This indicates that electronic nematicity is either a distinct order or a melted stripe phase that retains rotational symmetry breaking but not translational symmetry breaking of the CDW order.

As summarized in Fig. 5.9 at doping levels of x = 0.125 and 0.17 in Nd-LSCO, we record a signal for charge ordering and electronic nematicity. However, at x = 0.18 and 0.19, we see signatures of electronic nematicity but do not observe CDW ordering peak. Finally, in the overdoped case at x = 0.24 both CDW and nematicity signal is absent. The interplay, stability and onset of electronic nematicity, CDW order and the LTO $\rightarrow$ LTT structural transition suggest that these three symmetry-breaking phases are related in a nontrivial way.

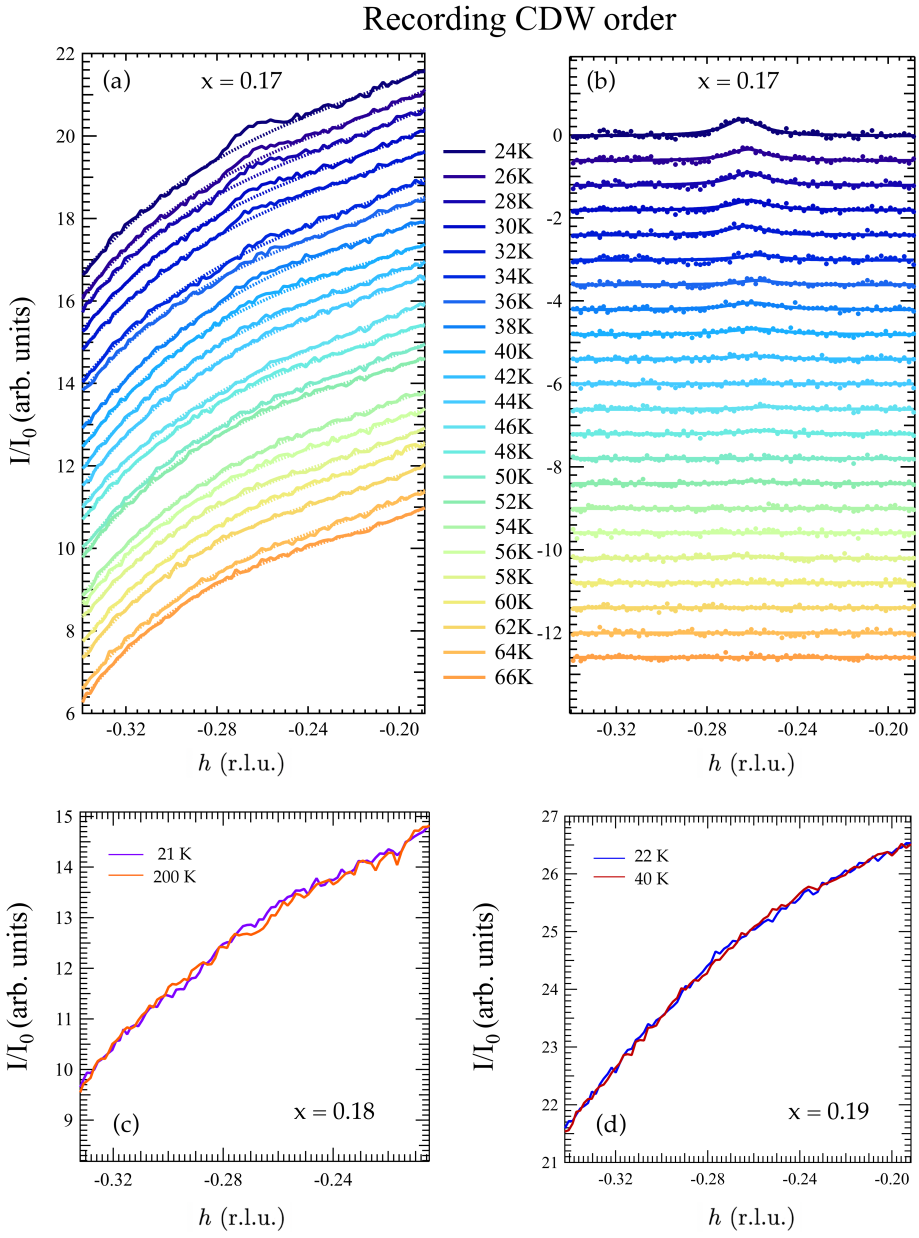

Figure 5.8: Charge density wave (CDW) order at different hole doping levels in Nd-LSCO: (a) shows the recorded CDW order data with a dotted line to show background subtraction, in (b) we show the background subtracted data fitted with the Lorentzian line shape. Data indicate data and lines indicate the fitting curve. In (c) and (d), at x = 0.18 and x = 0.19, we did not detect a CDW order. Shown is the data at high and low temperatures. We did not detect a CDW signal at x = 0.24.

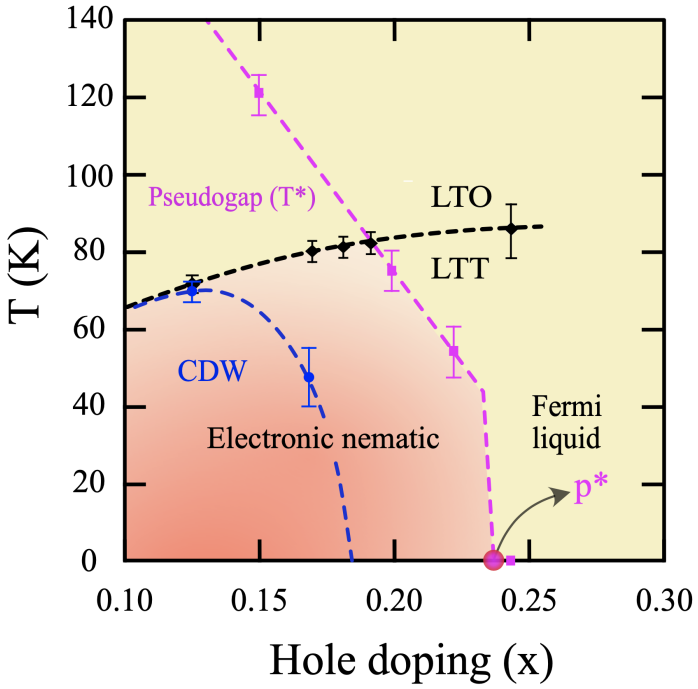

Figure 5.9: Updating the phase diagram for Nd-LSCO: The doping-temperature phase diagram of Nd-LSCO. The black diamonds show the structural phase transition from the LTO to LTT phase, the blue circles record the onset temperature of the CDW order. The black, purple, and blue dotted lines are a guide to the eye. The existence of a quantum critical point at $p^* \sim 0.23$ has been identified in [6, 38]. The pseudogap temperature as a function of hole-doping is shown by the purple squares, which marks the onset of the upturn in the resistivity $\rho(T)$, as reported in [6]. We report the absence of orbital asymmetry at the doping of x = 0.24 above our base temperature.

5.5.3 Change in the nature of LTO → LTT phase transition

Apart from the evidence for vanishing electronic nematic order, one also observes the change in the nature of the LTT → LTO phase transition from first-order like to second-order like in Fig. 5.7. Such a change can happen due to multitude of reasons, which is not very clear to us at the moment. One can speculate that a second-order nature of this phase transition might indicate the presence of strong fluctuations [40] corroborating a possibility of a (nematic) QCP, other possibilities include the role of disorder in smoothening the sharp

transition, or the reconstruction of the Fermi surface around the pseudogap critical point, which causes the free energy to favor a second-order transition route for the structural order parameters.

5.6 Summary and conclusions

We report the evidence for vanishing electronic nematic order in the vicinity of the QCP at x = 0.23 that has been identified in Nd-LSCO and other cuprates. This suggests that nematicity may be the fluctuating order responsible for the quantum critical phenomena at this point. Consequently, nematicity may play a larger role in understanding the cuprate phase diagram that has been previously recognized, possibly having a key role in the nature of the pseudogap phase or impacting the superconducting transition temperature. In this chapter, we investigated five Nd-LSCO samples at different Sr hole doping levels. Along with investigating the electronic nematic order near the end of the pseudogap phase in Nd-LSCO. We also documented the CDW signal, and report that it vanishes beyond x = 0.18 which is in agreement with previous similar studies using other experimental probes. Possible scenarios for these obervations include the existence of a zero-temperature nematic QCP and/or a nematic character to the pseudogap regime in this family (as suggested in Ref. [40]). We also report a non-trivial relationship between three distinct structural and electronic symmetry breaking phases with varying carrier concentration in the La-based cuprates.

Chapter 6

Behavior of charge order and electronic nematicity under in-plane uniaxial stress

6.1 Introduction

The co-existing electronic phases in cuprates — charge density wave order, superconductivity, magnetism, orbital order, nematicity — having almost identical energy and temperature scales provides a barrier in developing a microscopic or a robust phenomenological description for these phases. One way to sort these phases can be via disentangling the roles of nematicity, CDW order and superconductivity in the cuprates — which requires a means to vary one (nematicity or CDW order) while minimizing changes to other properties — through a tunable knob, such as carrier concentration, magnetic field or uniaxial pressure. A powerful means to achieve this goal is to apply uniaxial strain in order to tunably change the degree of orthorhombicity, and measure the impact of the resulting changes of the crystal structure on electronic nematic order, unidirectional CDW order and superconductivity.

In the cuprates, strain can have a dramatic effect on CDW order. Recent experiments by Le Tacon and collaborators in the cuprate $YBa_2Cu_3O_{6+x}$ (YBCO) showed strain results in the formation of intense long range ordered CDW order [73]. However, the impact of strain may vary significantly between different cuprates materials (like Nd-LSCO versus YBCO) owing to their different crystalline structures and the internal strain this applies

on the CuO_2 planes. Few reports of competition between static stripe and superconducting phase in Nd-LSCO has been made under hydrostatic pressure [74] as well.

This chapter is a work-in-progress, we present preliminary unpublished results from our most recent beamtime.[1] The first half of the chapter discusses the theory of uniaxial strain, laying the framework for discussing the design and working of the uniaxial device. The latter half establishes the robustness of the device by shows results for the response of CDW order with uniaxial stress in 1/8th doped Nd-LSCO. We also present incomplete results for the response of the low-temperature (001) Bragg peaks — associated with the orbital asymmetry of the neighbouring layers in Nd-LSCO — with applied uniaxial stress.

6.2 Uniaxial strain

Uniaxial strain proves to be a useful way in understanding the role of directional crystal deformations — which influences the way how orbitals overlap in the neighboring sites and layers — in the correlated electronic states of matter. This selection not only allows us to decouple co-existing symmetry breaking phases providing a way to understand the behavior of the electronic structure under changing point group symmetries.

6.2.1 Theory of stress and strain

When a rigid object is subjected to external force, the deformation is described via *strain* and *stress* tensor fields — the former being the measure of relative displacements relative to the original state and the latter is the description of how the (restoring) forces are distributed internally throughout the strained object. This section is based on derivations and discussions covered in Ref. [75].

For a one-dimensional rod, the unstrained length is L and under an external (elongation) force the new length becomes $L + \Delta L$. For such a case, if the transformation of every point along the length is $x \to x + u$, the strain on an infinitesimal element dx would be:

[1] The data presented in this chapter was the first decent dataset, after several trials, on our uniaxial stress device collected in February 2020. Our main objective was to establish the working and application of the uniaxial stress device on our polished-cut samples. The device appeared to be working and we were lucky enough to collect some data for the CDW order with strain. This, however, still remains to be reproduced and possibly scrutinized under higher strains — these plans had to be postponed due to canceling of our CLS shifts in June-July owing to spread of covid19 in Canada.

$$\varepsilon = \frac{\Delta L}{L} = \frac{\partial u}{\partial x}. \tag{6.1}$$

A more general description of the strain tensor can be obtained by considering a coordinate $\boldsymbol{x}$ and a displacement vector $\boldsymbol{u}$ ($= u\hat{\boldsymbol{x}} + v\hat{\boldsymbol{y}} + w\hat{\boldsymbol{z}}$), such that $\boldsymbol{x} \to \boldsymbol{x} + \boldsymbol{u}$, where the components of the strain tensor would be given by

$$\varepsilon_{ij} = \frac{1}{2}\left(\frac{\partial u_i}{\partial x_j} + \frac{\partial u_j}{\partial x_i}\right), \tag{6.2}$$

where the i, j refer to principal axes x, y, z. The strain tensor in the expanded form would look like:

$$\varepsilon_{ij} = \begin{pmatrix} \varepsilon_{xx} & \varepsilon_{yx} & \varepsilon_{zx} \\ \varepsilon_{xy} & \varepsilon_{yy} & \varepsilon_{zy} \\ \varepsilon_{xz} & \varepsilon_{yz} & \varepsilon_{zz} \end{pmatrix} = \begin{pmatrix} \frac{\partial u}{\partial x} & \frac{1}{2}\left(\frac{\partial u}{\partial y} + \frac{\partial v}{\partial x}\right) & \frac{1}{2}\left(\frac{\partial u}{\partial z} + \frac{\partial w}{\partial x}\right) \\ \frac{1}{2}\left(\frac{\partial v}{\partial x} + \frac{\partial u}{\partial y}\right) & \frac{\partial v}{\partial y} & \frac{1}{2}\left(\frac{\partial v}{\partial z} + \frac{\partial w}{\partial y}\right) \\ \frac{1}{2}\left(\frac{\partial w}{\partial x} + \frac{\partial u}{\partial z}\right) & \frac{1}{2}\left(\frac{\partial w}{\partial y} + \frac{\partial v}{\partial z}\right) & \frac{\partial w}{\partial z}. \end{pmatrix}, \tag{6.3}$$

As one would expect from Eq. (6.2), $\varepsilon_{ij} = \varepsilon_{ji}$, the strain tensor is symmetrical, exploiting this symmetry helps in reducing the number of material constants required to describe the relation between the stress and strain.

For a linear elastic material, the most general linear relation (by Hooke's Law) among all the components of the stress and strain tensor for uniaxial stress (load) conditions is given by

$$\sigma_{ij} = C_{ijkl}\varepsilon_{ij}, \tag{6.4}$$

where C_{ij} is known as the stiffness tensor. Assuming equivalence of mixed partials and symmetry in the off-diagonal elements of the strain tensor, we reduce the material constants from 81 to 21. The most general anisotropic linear elastic material therefore has 21 material constants. This can further be simplified for different space groups, the one which we are interested in being the tetragonal crystals of Nd-LSCO with the $I4/mmm$ space group symmetry. The stiffness matrix for such a stress-strain would look like:

$$\overbrace{\begin{pmatrix}\sigma_{xx}\\ \sigma_{yy}\\ \sigma_{zz}\\ \sigma_{yz}\\ \sigma_{zx}\\ \sigma_{xy}\end{pmatrix}}^{\text{Uniaxial stress}} = \overbrace{\begin{pmatrix} C_{11} & C_{12} & C_{13} & 0 & 0 & 0\\ C_{12} & C_{11} & C_{13} & 0 & 0 & 0\\ C_{13} & C_{13} & C_{33} & 0 & 0 & 0\\ 0 & 0 & 0 & C_{44} & 0 & 0\\ 0 & 0 & 0 & 0 & C_{44} & 0\\ 0 & 0 & 0 & 0 & 0 & \frac{1}{2}(C_{11}-C_{12}) \end{pmatrix}}^{\text{Stiffness tensor for a tetragonal lattice}} \overbrace{\begin{pmatrix}\varepsilon_{xx}\\ \varepsilon_{yy}\\ \varepsilon_{zz}\\ 2\varepsilon_{yz}\\ 2\varepsilon_{zx}\\ 2\varepsilon_{xy}\end{pmatrix}}^{\text{Uniaxial strain}} \tag{6.5}$$

The C_{ij}'s are obtained using resonant ultrasound spectroscopy, and other sound velocity measurement probes. Here is what the stiffness tensor coefficients for $La_{1.86}Sr_{0.14}CuO_4$ (LSCO) in a tetragonal phase [76] would look like,

$La_{1.86}Sr_{0.14}CuO_4$	C_{11}	C_{33}	C_{23}	C_{12}	C_{44}	C_{66}
$T = 300$ K	2.67	2.57	0.99	0.65	0.68	0.59

where the C_{ij}'s are in the units of 0.01 GPa. The values for the stiffness coefficients of Nd-LSCO would be similar. A quick demonstration of how to think of these numbers: if there is a 0.01% change in the lattice constants, say along c-axis, determined by shifting of the Bragg peaks — that would imply a stress of 2.57 kPa is applied[2] by the uniaxial stress device.

[2]The convention followed here is: change caused by compressive strains being positive and tensile strains being negative.

6.2.2 Uniaxial stress mechanism and other techniques

The promise of uniaxial strain as a tuning parameter for understanding competing phases in strongly correlated systems, especially unconventional superconductors, has been around for a long time. Over this period, uniaxial stress has proved its niche over hydrostatic pressure (on powdered samples, generally) by selectively tuning and comparing the physics involved along different crystallographic directions, for instance a 0.1 GPa stress along [100] would not make a big difference in T_c, however, a similar stress along [110] would increase the T_c two-folds in Eu doped LSCO [77].

Broadly speaking, we classify uniaxial stress configuration under two main categories depending on the purpose of the measurement:

1. **Diffraction experiments** which need access to the surface of the crystal — for a beam of energetic particles impinging on the face — which is under uniaxial strain. The Laue geometry plays an important role, a though experiment would be an investigation of a certain $(hk\ell)$ peak under synchrotron radiation, which would significantly restrict the possible placement of the sample and quantity of the strains applied.

2. **Non-diffraction probes** which need thermal/electrical contact via conducting wires/epoxy, and does not necessarily depend on either the medium or the geometry of the sample placement as long as the strain is homogeneous and uniaxial. This allows the application of huge strains, upto 20 GPa [78], and arguably more uniform strains.

Another classification can be done on the basis of the mechanism of the apparatus, and the application media of strain, namely

1. a **mechanical setup**, generally involving a combination of screw-bolt-spring allowing turning the screw to apply a uniaxial force on the sample using the clamps,

2. a **piezoelectric setup**, through a certain number of piezoelectric stacks in parallel [79] that control stress by applying an external voltage.

Our attempt would lie at the intersection of the former of both, that is a stress device which allows (resonant[3]) x-ray scattering experiments using a mechanical setup. Recent efforts in the field of synchrotron radiation compatible devices — based on the piezoelectric stacks mechanism — involve work done by Le Tacon on YBCO [73] which reports

[3]The restricted access to the reciprocal space makes the job slightly trickier.

a dramatic increase in the 3-dimensional stabilization of charge order on applying $\sim 1\%$ strain on single crystals of de-twinned YBCO.

We discuss our design in the section ahead, our main motivation was to develop a device capable of applying homogeneous uniaxial strain along a preferred direction[4], which is compatible with the RSXS scattering chamber at the REIXS beamline at the CLS. The scattering chamber has the ability to turn the screw — via a hex-head screwdriver attached to the end of a long arm controlled from outside, without breaking the ultra-high vacuum — and apply/modify strain in the sample by clockwise and anti-clockwise turns.

Furthermore, it is worthwhile to mention the constraints we are working under owing to the experimental setup and the geometry of scattering in the chamber — some of the challenges include:

- Restricted scattering geometry for the $\boldsymbol{Q}$ values we are interested in,
- Bulging epoxy contact at the edges forbidding low-angle scattering,
- Avoiding hysteresis due to applying-removing strain, or compressive-tensile strain,
- Avoiding buckling, cracking, and strain inhomogenities while applying strain by turning the screw using an in-situ screwdriver arm,
- Size of the sample versus beam spot size to ensure homogeneous strain signal,
- Avoiding hysteresis due to heating-cooling cycles.

6.2.3 Design of uniaxial strain device

Our uniaxial stress device — a mechanical attempt to apply uniaxial strain under the contraints mentioned in the previous section — works on a basic differential screw mechanism. The entire assembly is divided into three stages:

- The **bottom-third** fits in the our pre-designed sample holder compatible with the sample receptacle in the scattering chamber at the CLS's REIXS beamline. This part remains stationary while we turn the differential screw above to apply uniaxial strain.

[4]Depending on the how we place the sample, and which faces are under stress.

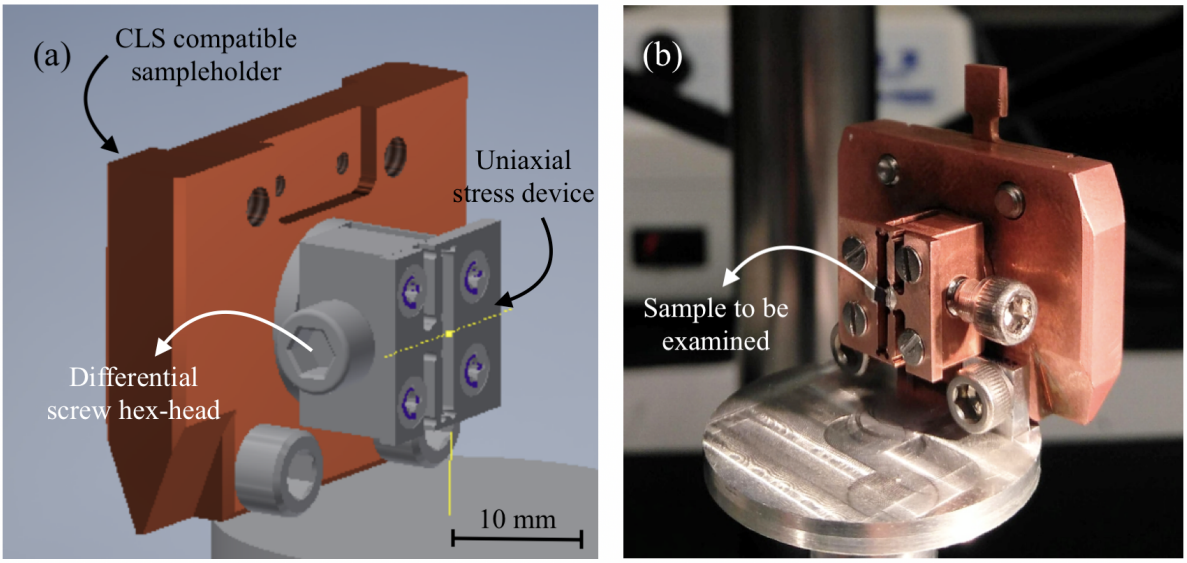

Figure 6.1: Uniaxial stress device: Design and reality, (a) AutoCAD design of the uniaxial stress device, (b) Machined product with a test sample on with mounting-epoxy scheme (a) (discussed ahead).

- The **middle-third** consists of two threaded copper blocks — one movable and the other as an extension of the bottom-third — naturally, one moves relative to other. This middle assembly has a differential screw mechanism in which one copper block moves differentially as function of the screw rotations (say θ_s) which initiates the strain in the system. A differential screw has two types of screw threadings (say t_1 and t_2), such that, if free both blocks would move $t_1\theta_s$ and $t_2\theta_s$ in the same direction. The relative motion, however, in such a mechanism would be $|t_1 - t_2|\theta_s$ — implemented in our setup by fixing one of the blocks — this allows us to apply fine tuned strain by choosing the threading difference cautiously. Most anvil-based setups do not go further, however, one might argue that the strain applied can have non-uniaxial components in a rigid block setup: to account for such an effect we transmit this stress to the top-third, or the sampleholder plate. This feature serves two purpose: i) cancels out non-uniaxial components of the stress, and ii) reduces the strain applied, giving us an even more fine-tuned setup[5].

[5]This is very useful as it gives us some flexibility to rotate in a safe-range during the experiment, for example a 90 degree turn would roughly correspond to 0.1% strain, depending on the sample's stiffness coefficients.

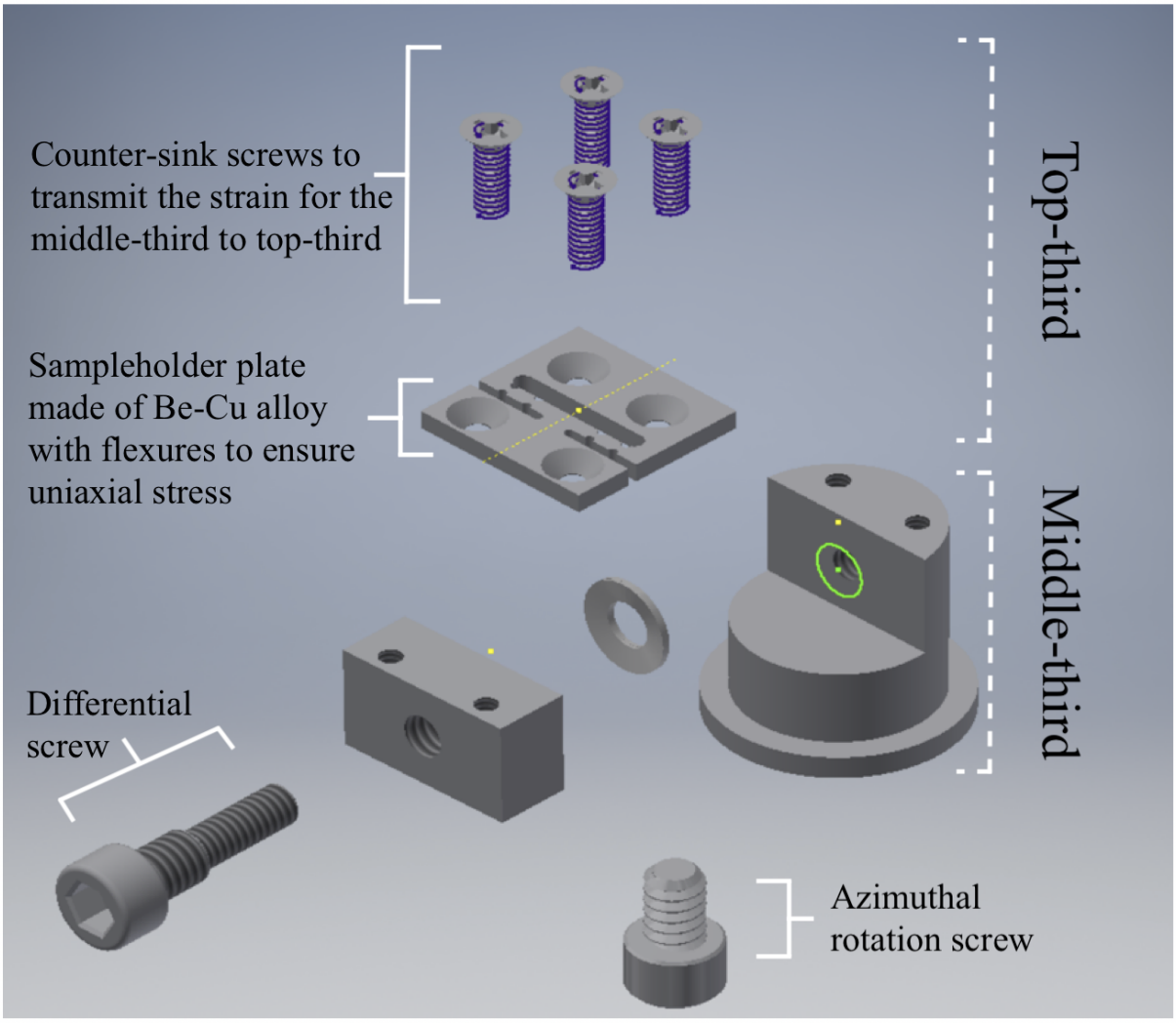

Figure 6.2: Uniaxial device: Exploded view with functioning of various parts. The entire assembly shown in this figure fits into a CLS-REIXS beamline's compatible copper sampleholder, which is shown in the previous figure with the condensed view of the entire assembly. Top-third and Middle-third labels are described in the text.

- The **top-third** is a 1 mm thick Be-Cu alloy sampleholder plate. Beryllium-Cooper (Be-Cu) is commonly used in low temperature cryogenic apparatus because of its mechanical strength, non-magnetic nature, and good thermal conductivity in this temperature range. As it retains its elastic properties at low temperature, it becomes a good choice for the part — applying uniaxial stress — in direct contact with the sample through epoxy, as shown in Fig 1(b). To cancel of stray stresses, we use a combination of flexures which are design features engineered to provide a specific degree of freedom. The one we use is called a Notch flexure — a thin curved cutout on both sides of a Be-Cu piece — which constrains 5 degrees of freedom, essentially solving the problem of non-uniaxial strains.

The sample is mounted on the Be-Cu sampleholder plate using epoxy around the edges which transmits the strain and ensures good thermal conduction to the sample. The sample is mounted such that the center of the sample passes through the central axis of the goniometer at the scattering chamber at the REIXS beamline. The strain, as described before, is applied by turning the differential screw — Fig. 6.3 shows how the two ends (or clamps) move without a sample. We have observed that compressive strains are more robust and reproducible than tensile ones. In the initial runs the uniaxial device was found capable for applying strains upto 0.4% based on the shifts in the Bragg peaks. The strain homogeneity and critical limit also depends on the sample material and dimensions to be discussed later. There is a possibility of adding a strain gauge which can validate the strain values obtained by shift in Bragg peaks.

6.2.4 Sample mounting and the role of epoxy

Before mounting the sample on the uniaxial stress device, the surfaces are polished to obtain parallel planes to avoid inhomogeneous and asymmetric stresses. In our trials, we have found chemical etching to be essential to get rid of the first few bad atomic layers due to polishing imperfections[6]. The rate of etching depends on the surface imperfection, the larger the imperfection the more susceptible to etching, this is crucial for the surface of the sample which faces the x-ray beam — as we cannot afford to have a non-uniform surface — whereas the bottom portion of the sample would not make a big difference.

After making sure the sample is polished well, it is set into position on the sampleholder plate using silver epoxy (EPO-TEK H20E). The epoxy comprises of two components, say part A and part B, which are to be mixed in equal amounts and then applied on the ends

[6]The techniques how the samples are cut, polished and etched are discussed in more detail in chapter 4.

of the sample in a certain fashion (like shown in Fig. 6.3). We generally use a 0.25 mm clean copper wire as a paint-brush to settle the epoxy and make both th ends symmetric, special care is taken to get rid of any bubbles or mixing irregularities. The entire assembly, which is mostly made of copper and is thermally conducting, is then kept covered on a hot platform to cure the epoxy, we generally follow 150 degree Celsius for 1 hour (this depends greatly on the kind of the epoxy used) and then it is gradually cooled down to room temperature to find the hardened-cured epoxy bonds.

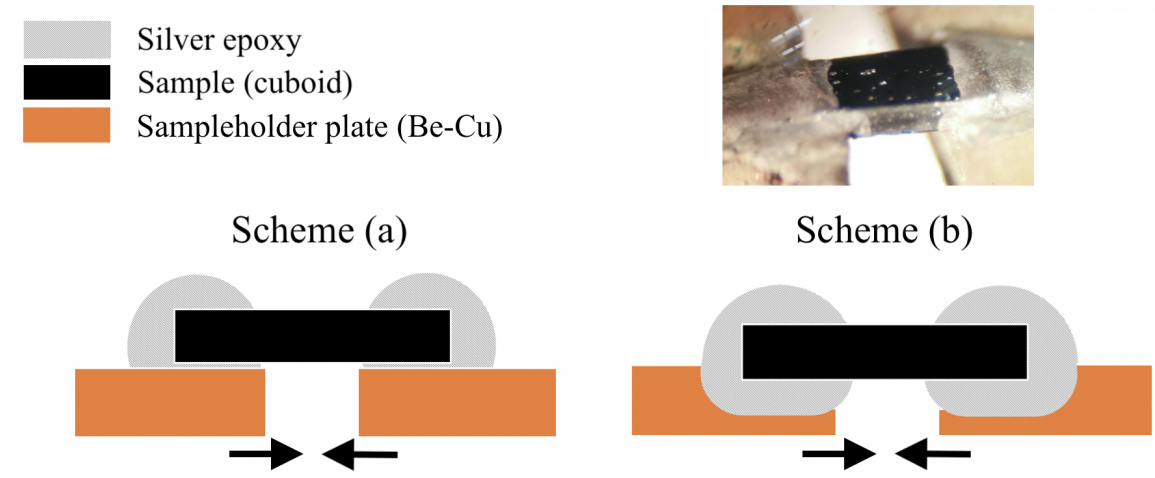

Figure 6.3: Different epoxy application schemes: Samples under compressive uniaxial strain using Scheme (a) and (b). In scheme(b), the strain applied was more homogeneous with lower tendency to buckle than scheme (a). The thickness of the sample in the picture is almost equal to that of a human hair.

This is a crucial step, as silver epoxy is the point-of-contact between the mechanical stress generating assembly and the two ends of the rigid cuboidal sample. The epoxy encapsulates the edges and vertices at the two ends — keeping a constant cross-section area — we try to ensure that the strain transmission is uniaxial and homogeneous in the elastic limit. For this purpose, we tried different schemes of applying epoxy around the sample. In our first trial, as shown in Fig. 6.3(a), we laid a very thin layer of silver epoxy and then placed the sample over it, and finally creating an encapsulating symmetric bulge around the ends of the sample. This worked decently for low stress levels, but we experienced bulging of the sample as we applied more stress. To counter this, our next epoxy-application scheme, as shown in Fig. 6.3(b) involved introducing a 0.2 mm valley cut in the Be-Cu sampleholder plate — which is almost the same thickness of the sample (under strain) – this ensures the deformation/drag of epoxy is uniform on top and bottom

surfaces. This helps with the problem of buckling at low strain values. There is, however, a theoretical buckling limit that is greater than the fracture point of the sample. In our trials, we noted that the fracture point of sample is reached before that of the epoxy contacts, maximum strain can be achieved by choosing the dimensions, particularly thickness of the sample under strain. We have tried samples of thickness: 200, 300, and 500 μm, we find the strain homogeneity is best achieved in the 200 μm. Assuming, the amount of strain is not limited by the epoxy — we can calculate the buckling load limit, as F_{critical} for given dimensions using the Euler's formula [80]:

$$F_{\text{cr}} = \frac{4\pi^2 Y I_m}{\ell^2}, \tag{6.6}$$

where Y is the modulus of elasticity of the material, ℓ is the unsupported length of the sample, d is the thickness, and I_m is the minimum area moment of inertia of the cross section of the (cuboid) sample bar. This allows us to find the critical strain for buckling, we replace the area moment of inertia as $\frac{\ell d^3}{12}$, and use Hooke's law to get critical strain $(= \frac{F_{\text{cr}}}{Y \ell d})$ as:

$$\varepsilon_{\text{cr}} = \frac{\pi^2}{3} \left(\frac{d}{\ell}\right)^2. \tag{6.7}$$

Optimizing with our dimensions, the theoretical critical buckling limit comes out to be around 2%. In our preliminary trials we reached values less than 0.5% before fracturing the sample, it requires more investigation both experimental and numerical modeling (simulating using finite element analysis) to properly characterize the strain transmission and distribution through the sample dimensions.

One more important factor, as mentioned before, is the access to a clean surface for scattering geometry. This brings a challenge of not using wire contacts, and strain gauges as metal and epoxy contacts would add noise to the signal owing to their presence in the beamspot on the sample during reciprocal scans. We will show how this forbids us to access the CDW order at low angles as the bulge of the epoxy hinders the incident beam.

6.2.5 Placement in the RSXS chamber

The design of the uniaxial stress device is done in such a manner to ensure beamspot stability with change in temperature — that is, from the sample frame of reference — we have designed it minimize the change in the beamspot position with temperature and added uniaxial strain. The beam spot size at the sample is $\approx 250 \times 150$ μm. The polished-etched surface of the sample (a-b face) receiving the incident beam is aligned with the axis of the goniometer at the CLS.

We have the capability of making a 90 degree azimuthal turn, see Fig. 6.4(b), such that it allows us to look for collective excitations along and perpendicular to the direction of the uniaxial strain. The La214s have a tetragonal to orthorhombic structural transition, this freedom to detect ordering along and perpendicular to the uniaxial strain can be potentially used to induce rotational symmetry breaking via uniaxial strain in the otherwise tetragonal phase to record the response of electronic nematic fluctuations. The screw for applying strain as well as making an azimuthal turn is achieved by an in situ screwdriver arm that allows to make turn without breaking the ultra high vacuum.

As shown in the figure, we need to rotate the θ_s motor to align different screws with the in-built hex-screwdriver arm in the RSXS scattering chamber. In my experience, I have found that one can achieve (and reproduce) $\pi/8$ turns pretty robustly. In our preliminary trials, we have applied and released strain in two stages from an unstrained case — let's say a moderately strained case (strain set 1)and a maximally strained case (strain set 2) — we will discuss this in the sections ahead. The temperature sensors lower down from the crysostat allowing us to record the sample's temperature, we have waited a couple of extra minutes after temperature change schemes to give enough time to the sampleholder assembly reach equilibrium.

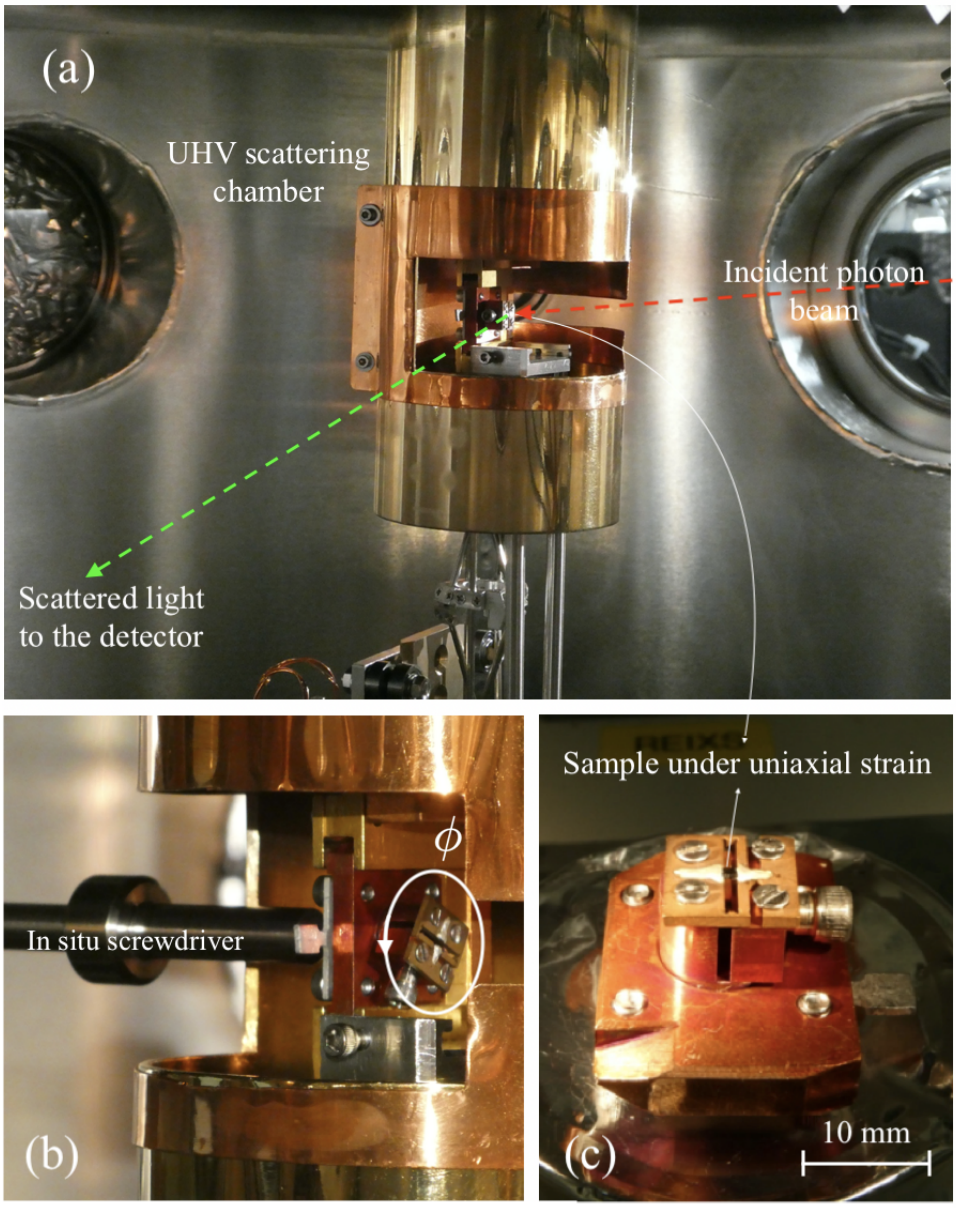

Figure 6.4: (a) View from the RSXS chamber's window showing the uniaxial stress device with the sample mounted. (b) The screw at the base of the device — can be rotated with an in situ screwdrives — provides the azimuthal degree of freedom, allowing access to $(h0\ell)$ and $(0k\ell)$ peaks. (c) Uniaxial stress device with the Nd-LSCO sample mounted, also shows in the scale valid for the (c) image.

Preliminary results

The results presented in the sections ahead are based on the February 2020 run at the REIXS endstation at the CLS in Saskatoon. Here, we discuss the measurement of structural and electronic features in the same direction as the applied strain. We calculate the amount of uniaxial strain — applied in the [100] direction — by calculating the shift in (004) and (-103) Bragg peaks . Due to technical difficulties in azimuthal rotations, unfortunately, we could not collect data for changes in the direction perpendicular to the applied (uniaxial) strain. We plan to do that in the subsequent beamtimes.

6.3 Structural Bragg peaks under uniaxial strain

6.3.1 Introduction

At low temperatures for Nd-LSCO, which is a tetragonal structure, we can access (004), (103), and (-103) Bragg peaks at an incident photon energy of 2200 eV. This gives us an opportunity to calculate the strain percentage — as probed at the beamspot patch by the incident x-rays — by comparing the shift in the Bragg peak's position (referred ahead as 2θ value) to find the change in the crystallographic axes. We begin as,

$$q = \frac{4\pi}{\lambda_{\text{in}}} \sin\left(\frac{2\theta}{2}\right) \tag{6.8}$$

where λ_{in} is the wavelength in the incident soft x-rays. Then we use the q-value to find $d = 2\pi/q$ which is connected to the Miller indices as:

$$\frac{1}{d^2} = \frac{h^2}{a^2} + \frac{k^2}{b^2} + \frac{l^2}{c^2} \tag{6.9}$$

After applying compressive uniaxial strain (say along a-axis), we measure the change in the 2θ position for the (004) Bragg peak to find the resulting change along c-axis. Next we note the change in 2θ position for the ($\pm$103) Bragg peak — already knowing the change along c-axis — we can calculate the change along a-axis using Eqn. (6.9).

6.3.2 Experimental procedure

The sampleholder is first positioned in the loadlock (at room temperature), then we bring the cryostat and sample receptacle assembly to room temperature to avoid any sudden contraction/expansions — during transferring the copper sampleholder — which can cause undesired strains to set in. Once the equilibrium is reached, we slowly lower the sample temperature to 30 K in order to perform further measurements.

We use a spatial and an energy resolved detector to record the (004), (103), and (-103) Bragg peaks because in our previous trials we have observed that after the application of uniaxial strain some specular reflections, often, due to domains misalignment can introduce noise in the peak signal if we just stick to the spatial detector (MCP). However, using an energy resolved detector (SDD) we can extract a clean signal — separating the specular reflection from the Bragg peak — and get a more accurate account of the shift in 2θ values, eventually allowing us to calculate the amount of strain (stress) the sample is under using the equations described above.

We begin with the unstrained case moving to non-resonant edge energies, 2000 eV here, to record changes in the structural Bragg peaks in Nd-LSCO. In the series of results ahead, we have followed the scheme of applying compressive strain at 30 K which lies in the low temperature tetragonal (LTT) phase. We looked at one unstrained case, and two values of strain by turning the differential screw. We were also able to come back to the unstrained case by turning the screw in the opposite direction.

6.3.3 Results and discussion

We note the shift in the 2θ position consistent with the compression along the direction in which we applied strain, the change in the c-direction indicated increase in the lattice parameter with strain applied along the a-axis. Fig. 6.5(b) shows the change in the (004) Bragg peak under uniaxial strain. Fig. 6.5(a) shows how the in-plane (103) behaves under uniaxial strain. Note that we have used the reciprocal lattice units/vectors instead of 2θ as we need to align and apply the strain, which causes change in the machine $\theta/2\theta$ value settings. The reciprocal directions, however, are accounted for those changes as it takes into consideration all the motor degrees of freedom.

We then use the Eqn. (6.8) and Eqn. (6.9) to characterize the applied strain based on the shifting of the Bragg peaks. We also compared the change in the h values for the peak for (103) and (-103), they appear to move in opposite direction as one might expect for uniaxial strain.

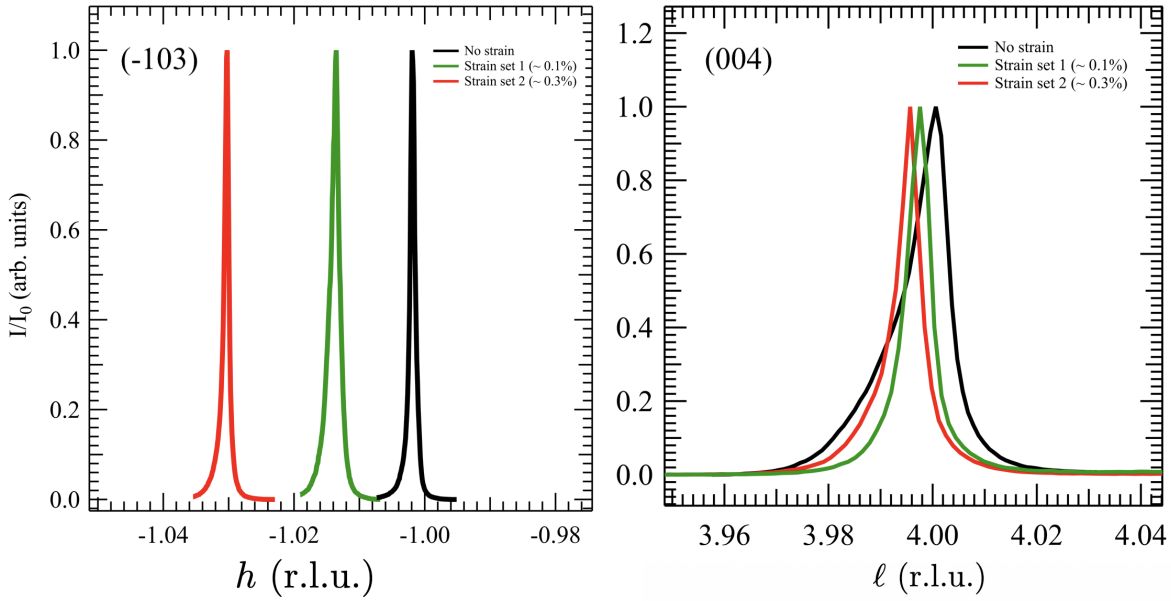

Figure 6.5: Structural Bragg peaks under uniaxial strain

Careful characterization of the structural Bragg peak help us understand if there are strain inhomogeneities and stray stresses present, from this minimal data set showing the shift in peak position we conclude that the applied strain is uniaxial to a great degree. Note that the change in the a-axis and c-axis parameters have comparable h and ℓ indices which gives us a chance to calculate the shift in the lattice parameters with applied uniaxial strain with fair certainty. We tried using hard x-rays (E $\sim$ 8.04 keV) at Stefan's Lab at University of Waterloo to characterize the applied strain using (107) and (006) Bragg peaks — the uncertainty involved in calculating the a-axis (or b-axis) lattice parameter change was about 5 times more than the results described above — which essentially made the results inconclusive. At CLS, we did not see stray or split peaks on the MCP detector, which generally imply mosaic character, or sometimes twinning in the crystal.

6.4 CDW order under uniaxial strain

6.4.1 Introduction

The discovery of an abnormally stable charge density wave order at x $\sim$ 1/8 doping in Nd-LSCO was made more than two decades ago [5]. Since then, it has been detected by numerous techniques, particularly to our interest, it can be probed with resonant x-ray scattering. As discussed in previous chapters, Nd-LSCO also exhibits electronic nematic order thus it provides a unique opportunity to understand the relation between CDW, electronic nematicity and structural distortions. Exploring the impact of uniaxial strain on these orders within the same measurement can help us answer whether the three symmetry-breaking phases compete? cooperate? Or leads to onset of each other?

The application of uniaxial strain can be used to identify if variation in CDW order and nematicity is associated with variation in the crystal structure or variation in the carrier concentration. We present results for the unstrained case along with two set of strain measurements from our previous beamtime.

6.4.2 Experimental procedure

As described in section 2.3.1, CDW order peak has a feeble intensity and a wide spread in reciprocal space compared to the traditional Bragg peaks which have sharp (intense) spectral signatures. This poses a challenge in the choice of the detectors, instead of point detectors we use a 2D MCP spatial detector — to cover a wider q-space region — giving us integrated intensity over the region to detect charge order superstructures with a period of several unit cells.

We start by tuning to Cu L resonance edge and perform a h-scan (or a θ scan) to detect and characterize CDW signal. For unstrained Nd-LSCO, from our previous measurements, we know the CDW order peak is peaked around (h, k, ℓ) value of (0.235, 0, 1.5)[7], we perform a h scan around that value at different temperatures to investigate the CDW order. For the unstrained case, as seen before, the CDW order starts fading at a temperature of 60 K. In this series of uniaxial strain experiments, we collect data for four values of temperature (in K): 30, 60, 90, 120, beginning with no strain, and collecting two set of measurements

[7]Once we have set the orientation matrices (UB) in SPEC macros using information about the motor positions from the (004), (103), and (-103) Bragg peak, we can run a macro to allow motor movement with some contraints to reach the desired $\boldsymbol{Q}$ value.

for different applied strains. The strain is applied at 30 K, that is, in the tetragonal phase of the material.

6.4.3 Results and discussion

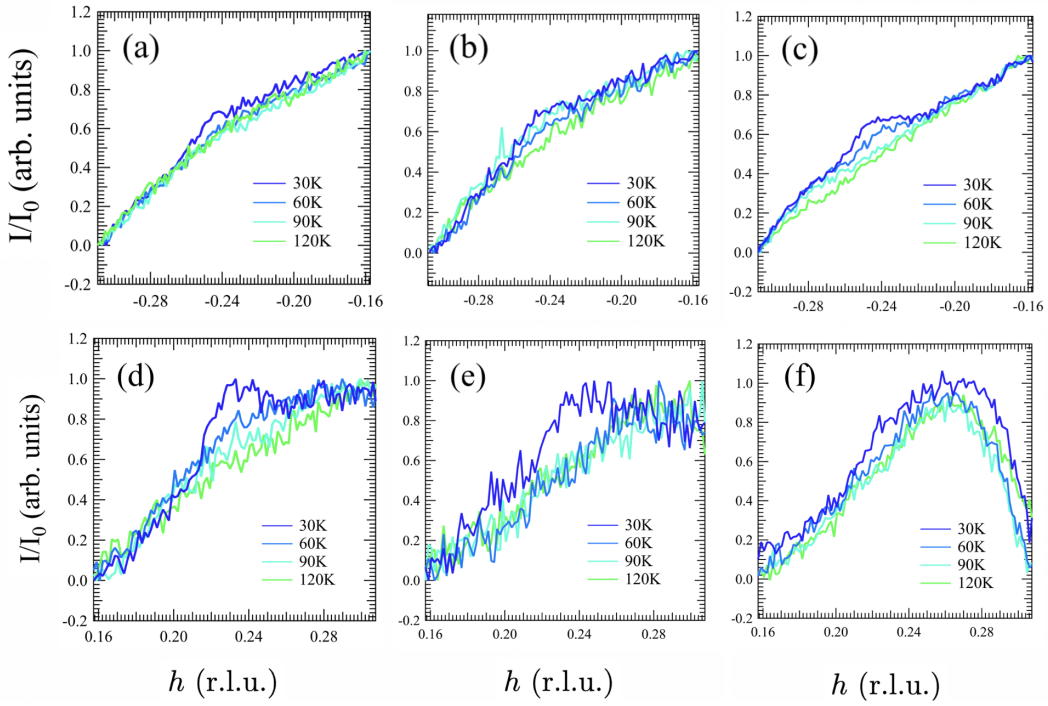

Figure 6.6: CDW ordering peaks at $(\pm 0.24, 0, 1.5)$ under uniaxial strain: We show results for the response of the CDW ordering peaks to in-plane uniaxial stress. (a, d) shows the case with no strain, in (b, e) we applied a moderate strain of $\sim 0.1\%$, and we increased the strain to a maximum of $\sim 0.3\%$ in (c, f). The data is plotted on a same scale, that is rescaled to show any broadening or enhancement features in the CDW ordering peaks. The data for maximum strain (f) has possible interference in the signal from the epoxy as the scattering angles is less than 30 degrees which becomes even more challenging with sample under strain as the epoxy can bulge and partially obstruct the line-of-sight of the incident photon beam.

We measured the CDW order associated with half-integer, that is $\boldsymbol{Q}_{\rm 2D} = (h, k, \ell) = (\pm 0.24, 0, 1.5)$ and integer, that is $\boldsymbol{Q}_{\rm 3D} = (h, k, \ell) = (-0.24, 0, 1)$, ℓ-values to investigate the

response of charge ordering with uniaxial strain along [100] direction. The measurements at $(+0.24, 0, 1.5)$ involved possible obstruction by the epoxy bulge for the line-of-beam of x-rays owing to the small angle of incidence, furthermore, the angles for $(+0.24, 0, 1)$ involved a direct beam into the detector; thus both of the $+h$ value ordering peak data is omitted here.

For the values of applied strain, in these preliminary trials, we do not observe a drastic change in the CDW ordering at half-integer and integer ℓ-values. Few notable observations from Fig. 6.6 involve widening of the CDW peak with slight enhancement in the peak intensity under applied strain. This, however, requires more careful characterization, possibly, with higher strain measurement sets. As discussed earlier, we could not successfully make the 90 degree azimuthal turn because of the the technical difficulties – that should make the understanding more complete in terms on strain and stabilization of biaxial charge order in direction perpendicular to applied uniaxial strain — this remains as an immediate future work.

6.5 LTO → LTT transition under uniaxial strain

6.5.1 Introduction

As described in the section 2.3.2, a key signature of Nd-LSCO is a — sharp, first order like — low-temperature structural transition from the orthorhombic to the tetragonal structure. Uniaxial strain, produces an anisotropic distortion, giving us control over the symmetry of the lattice which can enhance or suppress CDW order. Speculations based on Landau free energy combined with response to external applied conjugate field have shed some light on its coupling with the other symmetry breaking phases. Here we present coarse temperature evolution of the (001) Bragg peak which allows us to study the response LTO → LTT structural transition under uniaxial strain.

6.5.2 Experimental procedure

We have already discussed the experimental procedure for probing the (001) peak, please refer to section 5.4.1. Summarizing the key steps again: after setting the orientation matrices using the in-plane Bragg peaks at 2200 eV. We change the energy and instrument setting — mirror, grating, and slit gaps — to obtain decent signal intensity at the Cu L ($\sim$ 931 eV)and apical O K ($\sim$ 531 eV) edges. Once we located the peak on the SDD detector

for a cleaner signal, we increase the temperature to investigate how the (001) peak responds to in plane Cu and apical O edges. It is worthwhile to mention that the results here are coarse scans, that is the detector recorded the peak intensity as the sample temperature was increased, this is not ideal as sometimes the recorded 'sample temperature' has a time delay between recorded and real temperature. However, due to time constraints, we performed quicker scans to look for general features in the LTO $\rightarrow$ LTT structural transition under uniaxial strain. The recorded temperature and measured temperature has a drift/delay offset of $\sim$ 5-10 K, this has been attempted to be accounted for in the data presented ahead.

6.5.3 Results and discussion

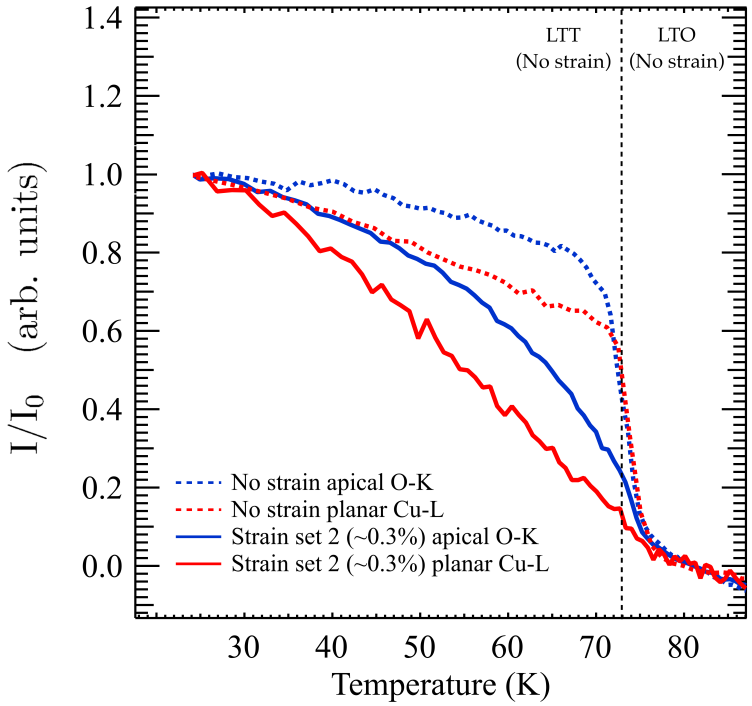

Figure 6.7: LTO $\rightarrow$ LTT structural transition under in-plane uniaxial strain for in-plane Cu L and apical O K edges: Dotted lines record the thermal evolution of (001) peak for x = 0.125 Nd-LSCO across the LTT to LTO structural transition which matches our previous studies. Solid line is the response of the (001) peak under in-plane uniaxial strain. Notice the broadening in the nature of transition.

Our results for the unstrained case matches with our previous carefully calibrated studies of LTO → LTT structural transition — as we observe a sharp transition marked by absence of the (001) peak — the dotted red and blue line show that in Fig. 6.7. The case under uniaxial strain, however, behaves differently. The nature of LTO → LTT structural transition appears to be softened substantially from the unstrained case, this can be due to broadening on the structural transition or creation of mixed domains or even an LTLO phase. Again, FWHM and comparison of peak intensity as a function of temperature would shed some light of such possibilities, for instance mixed domains would show up as split Bragg peaks, if any. Although — just as a thought experiment — an interesting situation can be imagined where the uniaxial strain helps the octahedral distortions in the LTT phase, possibly, favoring the formation of a nematic phase and maybe even emerging on a larger length scale as enhancement of a charge ordering superstructure. The former would appear as an enhancement in the difference[8] in (001) peak at in plane Cu L and apical O K edges, and the latter would show up as an increase in CDW peak intensity, or possible stabilization of charge order in the copper-oxide planes. One vague evidence to support such a claim would be the change of the (001) peak behavior at low temperatures — between 30-50 K — which are sufficiently far from the LTT → LTO transition ($\sim$ 70 K). This, however, remains a matter of future investigation along with possibly looking at other elemental edges in the copper-oxide and spacer layers.

6.6 Summary and conclusions

In this chapter, we established the working of the uniaxial stress device. We presented preliminary results on the application of in-plane stress in the cuprate high temperature superconductors. We record a few interesting features under strain, there needs to be more careful attempts to explore the ideas presented in the chapter. We have applied and been granted beamtime regarding this project and we hope to run these experiments as soon as the opportunity presents.

[8] Increase in the orbital asymmetry.

Chapter 7

Conclusions

We have measured the on-resonance allowed (001) Bragg peak for different atomic edges — in the CuO_2 and spacer layer of the layered pervoskite unit cell — and CDW order for five hole doping levels in single crystals of the cuprate high-temperature superconductor, Nd-LSCO.

We report the evidence for vanishing electronic nematic order in the vicinity of the putative QCP — at the end of the pseudogap phase — at x = 0.23 that has been identified in Nd-LSCO and other cuprates. This suggests that nematicity may be the fluctuating order responsible for the quantum critical phenomena at this point. Consequently, nematicity may play a larger role in understanding the cuprate phase diagram that has been previously recognized, possibly having a key role in the nature of the pseudogap phase or impacting the superconducting transition temperature. In this thesis, we measured five Nd-LSCO samples at different Sr hole doping levels. Along with investigating the electronic nematic order near the end of the pseudogap phase in Nd-LSCO, we also documented the CDW signal, and found that it vanishes beyond x = 0.18 which is in agreement with previous similar studies using other experimental probes. Possible scenarios for these observations include the existence of a zero-temperature nematic QCP and/or a nematic character to the pseudogap regime in this family. We also report a non-trivial relationship between three distinct structural and electronic symmetry breaking phases with varying carrier concentration in the La-based cuprate.

In the last chapter, we discuss the design and working of the in-plane uniaxial stress device. We present preliminary results providing a proof of principle by examining the shift in the structural Bragg peaks in response to applied strain. We report slight broadening of the CDW order along h-direction on applying uniaxial strain, immediate future

plans include reproducing the results and investigating the change along k-direction for the identical setup. We also recorded the 1st order like LTT $\rightarrow$ LTO transition which on applying strain loses the sharp features, this needs further investigation. The primary future goal would be understanding the interplay between electronic nematic order and the CDW order present at a hole doping of x = 1/8 in Nd-LSCO. The response of the (001) Bragg peak for atoms in the CuO_2 layer versus the spacer layer might provide us a way to characterize orbital asymmetry by a phenomenological description for examining nematic susceptibility with the applied strain. If successful, this can possibly help us characterize the nematic fluctuations in the vicinity of the putative QCP in Nd-LSCO, the results of which would direct evidence of the role of nematicity as a fluctuating order associated with the quantum criticality.

References

[1] J George Bednorz and K Alex Müller. Possible high $-$ T_c superconductivity in the Ba $-$ La $-$ Cu $-$ O system. *Zeitschrift für Physik B Condensed Matter*, 64(2):189–193, 1986.

[2] John Bardeen, Leon N Cooper, and John Robert Schrieffer. Theory of superconductivity. *Physical review*, 108(5):1175, 1957.

[3] John Bardeen, Leon N Cooper, and J Robert Schrieffer. Microscopic theory of superconductivity. *Physical Review*, 106(1):162, 1957.

[4] Maw-Kuen Wu, Jo R Ashburn, ClJ Torng, Ph H Hor, Rl L Meng, Lo Gao, Z Jo Huang, YQ Wang, and aCW Chu. Superconductivity at 93 K in a new mixed-phase Y $-$ Ba $-$ Cu $-$ O compound system at ambient pressure. *Physical review letters*, 58(9):908, 1987.

[5] JM Tranquada, BJ Sternlieb, JD Axe, Y Nakamura, and S Uchida. Evidence for stripe correlations of spins and holes in copper oxide superconductors. *Nature*, 375(6532):561–563, 1995.

[6] Louis Taillefer. Scattering and pairing in cuprate superconductors. *Annu. Rev. Condens. Matter Phys.*, 1(1):51–70, 2010.

[7] Steven A Kivelson, Ian P Bindloss, Eduardo Fradkin, Vadim Oganesyan, JM Tranquada, Aharon Kapitulnik, and Craig Howald. How to detect fluctuating stripes in the high-temperature superconductors. *Reviews of Modern Physics*, 75(4):1201, 2003.

[8] Eduardo Fradkin, Steven A Kivelson, and John M Tranquada. Colloquium: Theory of intertwined orders in high temperature superconductors. *Reviews of Modern Physics*, 87(2):457, 2015.

[9] Bernhard Keimer, Steven A Kivelson, Michael R Norman, Shinichi Uchida, and J Zaanen. From quantum matter to high-temperature superconductivity in copper oxides. *Nature*, 518(7538):179–186, 2015.

[10] Shin-ichi Uchida. *High temperature superconductivity: The road to higher critical temperature*, volume 213. Springer, 2014.

[11] A Schilling, M Cantoni, JD Guo, and HR Ott. Superconductivity above 130 K in the $Hg-Ba-Ca-Cu-O$system. *Nature*, 363(6424):56–58, 1993.

[12] Yoichi Ando, Kouji Segawa, Seiki Komiya, and AN Lavrov. Electrical resistivity anisotropy from self-organized one dimensionality in high-temperature superconductors. *Physical review letters*, 88(13):137005, 2002.

[13] R Daou, J Chang, David LeBoeuf, Olivier Cyr-Choiniere, Francis Laliberté, Nicolas Doiron-Leyraud, BJ Ramshaw, Ruixing Liang, DA Bonn, WN Hardy, *et al*. Broken rotational symmetry in the pseudogap phase of a $high-T_c$ superconductor. *Nature*, 463(7280):519–522, 2010.

[14] O Cyr-Choinière, G Grissonnanche, S Badoux, J Day, DA Bonn, WN Hardy, R Liang, N Doiron-Leyraud, and Louis Taillefer. Two types of nematicity in the phase diagram of the cuprate superconductor $YBa_2Cu_3O_y$. *Physical Review B*, 92(22):224502, 2015.

[15] MJ Lawler, K Fujita, Jhinhwan Lee, AR Schmidt, Y Kohsaka, Chung Koo Kim, H Eisaki, S Uchida, JC Davis, JP Sethna, *et al*. Intra-unit-cell electronic nematicity of the $high-T_c$ copper-oxide pseudogap states. *Nature*, 466(7304):347–351, 2010.

[16] Kazuhiro Fujita, Andrew R. Schmidt, Eun-Ah Kim, Michael J. Lawler, Dung Hai Lee, JC Davis, Hiroshi Eisaki, and Shin-ichi Uchida. Spectroscopic imaging scanning tunneling microscopy studies of electronic structure in the superconducting and pseudogap phases of cuprate $high-T_c$ superconductors. *Journal of the Physical Society of Japan*, 81(1):011005, 2011.

[17] V Hinkov, D Haug, B Fauqué, P Bourges, Y Sidis, A Ivanov, Christian Bernhard, CT Lin, and B Keimer. Electronic liquid crystal state in the high-temperature superconductor $YBa_2Cu_3O_{6.45}$. *Science*, 319(5863):597–600, 2008.

[18] AJ Achkar, M Zwiebler, Christopher McMahon, F He, R Sutarto, Isaiah Djianto, Zhihao Hao, Michel JP Gingras, M Hücker, GD Gu, *et al*. Nematicity in stripe-ordered cuprates probed via resonant x-ray scattering. *Science*, 351(6273):576–578, 2016.

[19] J Chang, E Blackburn, AT Holmes, Niels B Christensen, Jacob Larsen, J Mesot, Ruixing Liang, DA Bonn, WN Hardy, A Watenphul, *et al*. Direct observation of competition between superconductivity and charge density wave order in $YBa_2Cu_3O_{6.67}$. *Nature Physics*, 8(12):871–876, 2012.

[20] H Kamerlingh Onnes. research notebooks 56, 57. *Kamerlingh Onnes Archive, Boerhaave Museum, Leiden, the Netherlands*, 1911.

[21] MR Norman and C Pépin. The electronic nature of high temperature cuprate superconductors. *Reports on Progress in Physics*, 66(10):1547, 2003.

[22] G Ghiringhelli, M Le Tacon, Matteo Minola, S Blanco-Canosa, Claudio Mazzoli, NB Brookes, GM De Luca, A Frano, DG Hawthorn, F He, *et al*. Long-range incommensurate charge fluctuations in $(Y,Nd)Ba_2Cu_3O_{6+x}$. *Science*, 337(6096):821–825, 2012.

[23] Eduardo H da Silva Neto, Pegor Aynajian, Alex Frano, Riccardo Comin, Enrico Schierle, Eugen Weschke, András Gyenis, Jinsheng Wen, John Schneeloch, Zhijun Xu, *et al*. Ubiquitous interplay between charge ordering and high-temperature superconductivity in cuprates. *Science*, 343(6169):393–396, 2014.

[24] Stephen D Edkins, Andrey Kostin, Kazuhiro Fujita, Andrew P Mackenzie, Hiroshi Eisaki, S Uchida, Subir Sachdev, Michael J Lawler, E-A Kim, JC Séamus Davis, *et al*. Magnetic field–induced pair density wave state in the cuprate vortex halo. *Science*, 364(6444):976–980, 2019.

[25] Andrew Achkar. Charge density wave order in cuprate superconductors studied by resonant soft x-ray scattering. PhD Thesis, University of Waterloo. 2015.

[26] Riccardo Comin and Andrea Damascelli. Resonant x-ray scattering studies of charge order in cuprates. *Annual Review of Condensed Matter Physics*, 7:369–405, 2016.

[27] P Abbamonte, A Rusydi, S Smadici, GD Gu, GA Sawatzky, and DL Feng. Spatially modulated 'mottness' in $La_{2-x}Ba_xCuO_4$. *Nature Physics*, 1(3):155–158, 2005.

[28] AJ Achkar, F He, R Sutarto, J Geck, H Zhang, Y-J Kim, and DG Hawthorn. Resonant x-ray scattering measurements of a spatial modulation of the Cu 3 d and O 2 p energies in stripe-ordered cuprate superconductors. *Physical Review Letters*, 110(1):017001, 2013.

[29] JD Axe, AH Moudden, D Hohlwein, DE Cox, KM Mohanty, AR Moodenbaugh, and Youwen Xu. Structural phase transformations and superconductivity in $La_{2-x}Ba_xCuO_4$. *Physical Review Letters*, 62(23):2751, 1989.

[30] JD Axe and MK Crawford. Structural instabilities in lanthanum cuprate superconductors. *Journal of Low Temperature Physics*, 95(1-2):271–284, 1994.

[31] M Hücker. Structural aspects of materials with static stripe order. *Physica C: Superconductivity*, 481:3–14, 2012.

[32] Mirela Dragomir, Qianli Ma, J Patrick Clancy, Amirreza Ataei, Paul A Dube, Sudarshan Sharma, Ashfia Huq, Hanna A Dabkowska, Louis Taillefer, and Bruce D Gaulin. Materials preparation, single crystal growth, and the phase diagram of the cuprate high temperature superconductor $La_{1.6-x}Nd_{0.4}Sr_xCuO_4$. *arXiv preprint arXiv:2008.07573*, 2020.

[33] M Hücker, M v Zimmermann, M Debessai, JS Schilling, JM Tranquada, and GD Gu. Spontaneous symmetry breaking by charge stripes in the high pressure phase of superconducting $La_{1.875}Ba_{0.125}CuO_4$. *Physical Review Letters*, 104(5):057004, 2010.

[34] T Shibauchi, A Carrington, and Y Matsuda. A quantum critical point lying beneath the superconducting dome in iron pnictides. *Annu. Rev. Condens. Matter Phys.*, 5(1):113–135, 2014.

[35] Thanapat Worasaran, Matthias S Ikeda, Johanna C Palmstrom, Joshua AW Straquadine, Steven A Kivelson, and Ian R Fisher. Nematic quantum criticality in an fe-based superconductor revealed by strain-tuning. *arXiv preprint arXiv:2003.12202*, 2020.

[36] B Michon, C Girod, S Badoux, J Kačmarčík, Q Ma, M Dragomir, HA Dabkowska, BD Gaulin, J-S Zhou, S Pyon, *et al*. Thermodynamic signatures of quantum criticality in cuprate superconductors. *Nature*, 567(7747):218–222, 2019.

[37] S Badoux, W Tabis, F Laliberté, G Grissonnanche, B Vignolle, D Vignolles, Jerome Béard, DA Bonn, WN Hardy, R Liang, *et al*. Change of carrier density at the pseudogap critical point of a cuprate superconductor. *Nature*, 531(7593):210–214, 2016.

[38] C Collignon, S Badoux, SAA Afshar, B Michon, F Laliberté, O Cyr-Choinière, J-S Zhou, S Licciardello, S Wiedmann, N Doiron-Leyraud, *et al*. Fermi-surface transformation across the pseudogap critical point of the cuprate superconductor $La_{1.6-x}Nd_{0.4}Sr_xCuO_4$. *Physical Review B*, 95(22):224517, 2017.

[39] Yawen Fang, Gael Grissonnanche, Anaelle Legros, Simon Verret, Francis Laliberte, Clement Collignon, Amirreza Ataei, Maxime Dion, Jianshi Zhou, David Graf, *et al*. Fermi surface transformation at the pseudogap critical point of a cuprate superconductor. *arXiv preprint arXiv:2004.01725*, 2020.

[40] Y Sato, S Kasahara, H Murayama, Y Kasahara, E-G Moon, T Nishizaki, T Loew, J Porras, B Keimer, T Shibauchi, *et al*. Thermodynamic evidence for a nematic phase transition at the onset of the pseudogap in $YBa_2Cu_3O_y$. *Nature Physics*, 13(11):1074–1078, 2017.

[41] BJ Ramshaw, SE Sebastian, RD McDonald, James Day, BS Tan, Z Zhu, JB Betts, Ruixing Liang, DA Bonn, WN Hardy, *et al*. Quasiparticle mass enhancement approaching optimal doping in a high $-$ T_c superconductor. *Science*, 348(6232):317–320, 2015.

[42] Chandra M Varma. Quantum-critical fluctuations in 2d metals: strange metals and superconductivity in antiferromagnets and in cuprates. *Reports on Progress in Physics*, 79(8):082501, 2016.

[43] I Paul and M Garst. Lattice effects on nematic quantum criticality in metals. *Physical Review Letters*, 118(22):227601, 2017.

[44] Kousuke Ishida, Suguru Hosoi, Yuki Teramoto, Tomohiro Usui, Yuta Mizukami, Kenji Itaka, Yuji Matsuda, Takao Watanabe, and Takasada Shibauchi. Divergent nematic susceptibility near the pseudogap critical point in a cuprate superconductor. *Journal of the Physical Society of Japan*, 89(6):064707, 2020.

[45] N Auvray, B Loret, S Benhabib, M Cazayous, RD Zhong, J Schneeloch, GD Gu, A Forget, Dorothée Colson, I Paul, *et al*. Nematic fluctuations in the cuprate superconductor $Bi_2Sr_2CaCu_2O_{8+\delta}$. *Nature communications*, 10(1):1–7, 2019.

[46] Jörg Fink, E Schierle, E Weschke, and J Geck. Resonant elastic soft x-ray scattering. *Reports on Progress in Physics*, 76(5):056502, 2013.

[47] Yves Joly, SD Matteo, and Oana Bunău. Resonant x-ray diffraction: Basic theoretical principles. *The European Physical Journal Special Topics*, 208(1):21–38, 2012.

[48] Sergio Di Matteo. Resonant x-ray diffraction: multipole interpretation. *Journal of Physics D: Applied Physics*, 45(16):163001, 2012.

[49] C Vettier. Resonant elastic x-ray scattering: Where from? where to? *The European Physical Journal Special Topics*, 208(1):3–14, 2012.

[50] Jens Als-Nielsen and Des McMorrow. *Elements of modern X-ray physics*. John Wiley & Sons, 2011.

[51] Leslie L Foldy and Siegfried A Wouthuysen. On the dirac theory of spin-1/2 particles and its non-relativistic limit. *Physical Review*, 78(1):29, 1950.

[52] Eric Beaurepaire, Hervé Bulou, Fabrice Scheurer, and Jean Paul Kappler. *Magnetism: A synchrotron radiation approach*, volume 697. Springer, 2006.

[53] Jun John Sakurai. *Advanced quantum mechanics*. Pearson Education India, 1967.

[54] M Blume. Magnetic scattering of x rays. *Journal of Applied Physics*, 57(8):3615–3618, 1985.

[55] MW Haverkort, N Hollmann, IP Krug, and A Tanaka. Symmetry analysis of magneto-optical effects: The case of x-ray diffraction and x-ray absorption at the transition metal $L_{2,3}$ edge. *Physical Review B*, 82(9):094403, 2010.

[56] Adam S Foster, VB Sulimov, F Lopez Gejo, AL Shluger, and Risto M Nieminen. Structure and electrical levels of point defects in monoclinic zirconia. *Physical Review B*, 64(22):224108, 2001.

[57] Yi Lu. From itinerant to localized: an x-ray spectroscopic study of transition metal oxides. PhD Thesis, University of Stuttgart, 2017.

[58] DG Hawthorn, F He, L Venema, H Davis, AJ Achkar, J Zhang, R Sutarto, H Wadati, A Radi, T Wilson, *et al*. An in-vacuum diffractometer for resonant elastic soft x-ray scattering. *Review of Scientific Instruments*, 82(7):073104, 2011.

[59] RP Vasquez, BD Hunt, and MC Foote. Nonaqueous chemical etch for $YBa_2Cu_3O_{7-x}$. *Applied physics letters*, 53(26):2692–2694, 1988.

[60] Steven A Kivelson, Eduardo Fradkin, and Victor J Emery. Electronic liquid-crystal phases of a doped mott insulator. *Nature*, 393(6685):550–553, 1998.

[61] Eduardo Fradkin, Steven A Kivelson, Michael J Lawler, James P Eisenstein, and Andrew P Mackenzie. Nematic fermi fluids in condensed matter physics. *Annu. Rev. Condens. Matter Phys.*, 1(1):153–178, 2010.

[62] Matthias Vojta. Lattice symmetry breaking in cuprate superconductors: stripes, nematics, and superconductivity. *Advances in Physics*, 58(6):699–820, 2009.

[63] T-M Chuang, MP Allan, Jinho Lee, Yang Xie, Ni Ni, SL Bud'ko, GS Boebinger, PC Canfield, and JC Davis. Nematic electronic structure in the "parent" state of the iron-based superconductor $Ca(Fe_{1-x}Co_x)_2As_2$. *Science*, 327(5962):181–184, 2010.

[64] Jiun-Haw Chu, James G Analytis, Kristiaan De Greve, Peter L McMahon, Zahirul Islam, Yoshihisa Yamamoto, and Ian R Fisher. In-plane resistivity anisotropy in an underdoped iron arsenide superconductor. *Science*, 329(5993):824–826, 2010.

[65] VE Dmitrienko. Forbidden reflections due to anisotropic x-ray susceptibility of crystals. *Acta Crystallographica Section A: Foundations of Crystallography*, 39(1):29–35, 1983.

[66] David H Templeton and Lieselotte K Templeton. Polarized x-ray absorption and double refraction in vanadyl bisacetylacetonate. *Acta Crystallographica Section A: Crystal Physics, Diffraction, Theoretical and General Crystallography*, 36(2):237–241, 1980.

[67] Sourin Mukhopadhyay, Rahul Sharma, Chung Koo Kim, Stephen D Edkins, Mohammad H Hamidian, Hiroshi Eisaki, Shin-ichi Uchida, Eun-Ah Kim, Michael J Lawler, Andrew P Mackenzie, *et al*. Evidence for a vestigial nematic state in the cuprate pseudogap phase. *Proceedings of the National Academy of Sciences*, 116(27):13249–13254, 2019.

[68] Laimei Nie, Gilles Tarjus, and Steven Allan Kivelson. Quenched disorder and vestigial nematicity in the pseudogap regime of the cuprates. *Proceedings of the National Academy of Sciences*, 111(22):7980–7985, 2014.

[69] I Ia Pomeranchuk *et al*. On the stability of a fermi liquid. *Sov. Phys. JETP*, 8:361, 1958.

[70] Christopher McMahon. Symmetry of the charge ordering phases in hole-doped cuprates studied by resonant x-ray absorption and scattering. PhD Thesis, University of Waterloo 2019.

[71] Christian E Matt, Claudia G Fatuzzo, Yasmine Sassa, Martin Månsson, S Fatale, V Bitetta, X Shi, Stéphane Pailhes, MH Berntsen, Tohru Kurosawa, *et al*. Electron scattering, charge order, and pseudogap physics in $La_{1.6-x}Nd_{0.4}Sr_xCuO_4$: an angle-resolved photoemission spectroscopy study. *Physical Review B*, 92(13):134524, 2015.

[72] M Platé, JDF Mottershead, IS Elfimov, DC Peets, Ruixing Liang, DA Bonn, WN Hardy, S Chiuzbaian, M Falub, M Shi, *et al*. Fermi surface and quasiparticle excitations of overdoped $Tl_2Ba_2CuO_{6+\delta}$. *Physical Review Letters*, 95(7):077001, 2005.

[73] H-H Kim, SM Souliou, ME Barber, E Lefrançois, M Minola, M Tortora, R Heid, N Nandi, Rodolfo Alberto Borzi, G Garbarino, *et al*. Uniaxial pressure control of competing orders in a high-temperature superconductor. *Science*, 362(6418):1040–1044, 2018.

[74] S Arumugam, N Mori, N Takeshita, H Takashima, T Noda, H Eisaki, and S Uchida. Competition of static stripe and superconducting phases in $La_{1.48}Nd_{0.4}Sr_{0.12}CuO_4$ controlled by pressure. *Physical Review Letters*, 88(24):247001, 2002.

[75] LD Landau and EM Lifshitz. Theory of elasticity (volume 7 of a course of theoretical physics) pergamon press, 1970.

[76] JL Sarrao, D Mandrus, A Migliori, Z Fisk, I Tanaka, H Kojima, PC Canfield, and PD Kodali. Complete elastic moduli of $La_{2-x}Sr_xCuO_4$ (x= 0.00 and 0.14) near the tetragonal-orthorhombic structural phase transition. *Physical Review B*, 50(18):13125, 1994.

[77] Nao Takeshita, Takao Sasagawa, Takenari Sugioka, Yoshinori Tokura, and Hidenori Takagi. Gigantic anisotropic uniaxial pressure effect on superconductivity within the CuO_2 plane of $La_{1.64}Eu_{0.2}Sr_{0.16}CuO_4$: Strain control of stripe criticality. *Journal of the Physical Society of Japan*, 73(5):1123–1126, 2004.

[78] MK Crawford, RL Harlow, S Deemyad, V Tissen, JS Schilling, EM McCarron, SW Tozer, DE Cox, N Ichikawa, S Uchida, *et al*. High-pressure study of structural phase transitions and superconductivity in $La_{1.48}Nd_{0.4}Sr_{0.12}CuO_4$. *Physical Review B*, 71(10):104513, 2005.

[79] Clifford W Hicks, Mark E Barber, Stephen D Edkins, Daniel O Brodsky, and Andrew P Mackenzie. Piezoelectric-based apparatus for strain tuning. *Review of Scientific Instruments*, 85(6):065003, 2014.

[80] C Truesdell. Euler's calculation of buckling loads for columns of non-uniform section (1757). In *The Rational Mechanics of Flexible or Elastic Bodies 1638–1788*, pages 345–347. Springer, 1960.

[81] Neil W Ashcroft, N David Mermin. *Solid state physics.* New York: Holt, Rinehart and Winston,, 1976.

[82] SP Collins. *X-ray Scattering and Absorption by Magnetic Materials. Oxford Series on Synchrotron Radiation*. Oxford University Press, 1996.

[83] Pierre-Gilles De Gennes and Jacques Prost. *The physics of liquid crystals*, volume 83. Oxford university press, 1993.

[84] Takashi Suzuki and Toshizo Fujita. Anomalous change in crystalline structure of $(La_{1-x}Ba_x)_2CuO_{4-\delta}$. *Journal of the Physical Society of Japan*, 58(6):1883–1886, 1989.

[85] N Ichikawa, S Uchida, JM Tranquada, T Niemöller, PM Gehring, S-H Lee, and JR Schneider. Local magnetic order vs superconductivity in a layered cuprate. *Physical Review Letters*, 85(8):1738, 2000.

[86] Anirban Pal, Manuel Chinotti, Jiun-Haw Chu, Hseuh-Hui Kuo, Ian Randal Fisher, and Leonardo Degiorgi. Optical anisotropy in optimally doped iron-based superconductor. *npj Quantum Materials*, 4(1):1–5, 2019.